# Long-distance Quantum Communication with Neutral Atoms

by

Mohsen Razavi

B.S. (1998), M.S. (2000)
Electrical Engineering, Sharif University of Technology, Tehran, Iran

Submitted to the Department of Electrical Engineering and Computer Science
in partial fulfillment of the requirements for the degree of

Doctor of Philosophy

at the

MASSACHUSETTS INSTITUTE OF TECHNOLOGY

September 2006

Author . . . . . . . . . . . . . . . . . . . . . . . . . . . . . . . . . . . . . . . . . . . . . . . . . . . . . . . . . . . . . . .
Department of Electrical Engineering and Computer Science
August 24, 2006

Certified by . . . . . . . . . . . . . . . . . . . . . . . . . . . . . . . . . . . . . . . . . . . . . . . . . . . . . . . . . . . .
Jeffrey H. Shapiro
Julius A. Stratton Professor of Electrical Engineering
Thesis Supervisor

Accepted by . . . . . . . . . . . . . . . . . . . . . . . . . . . . . . . . . . . . . . . . . . . . . . . . . . . . . . . . . . .
Arthur C. Smith
Chairman, Department Committee on Graduate Students

# Long-distance Quantum Communication with Neutral Atoms

by

Mohsen Razavi

Submitted to the Department of Electrical Engineering and Computer Science
on August 24, 2006, in partial fulfillment of the
requirements for the degree of
Doctor of Philosophy

## Abstract

In this thesis, we develop quantitative performance analyses for a variety of quantum communication/computation systems that have the common feature of employing neutral atoms for storage/processing and photons for qubit transmission. For most of these systems, there is a lack of a precise performance analysis to enable a comparison between different scenarios from a top-level system standpoint. One main goal of this thesis is to fill that gap, thus providing quantum system designers with realistic estimates of system performance that can guide and inform the design process.

For many applications in quantum communication and distributed quantum processing, we need to share, in advance, an *entangled* state between two parties. Thus, *entanglement distribution* is at the core of long-distance quantum communication systems. It not only includes generation and transmission of entangled states, but it also requires storing them for further processing purposes. Whereas the photons are the prime candidate for the former task, they are not appropriate for long-time storage and processing. Metastable levels in some alkali atoms, e.g., rubidium, are attractive venues for quantum storage. In this thesis, we study several basic quantum memory modules—all based on single trapped atoms in high-finesse optical cavities—and analytically evaluate how efficiently they can be loaded with (entangled) quantum states. We propose a non-adiabatic mechanism for driving off-resonant Raman transitions that can be used in loading trapped-atom quantum memories. Our method is more flexible than its adiabatic counterpart in that it allows use of larger cavities and a larger class of driving sources.

We also describe two proposed implementations for long-distance quantum communication—one that uses trapped atoms as quantum memories and another that employs atomic ensembles for quantum storage. We provide, for the first time, a detailed quantitative performance analysis of the latter system, which enables us to compare these two systems in terms of the fidelity and the throughput that they achieve for entanglement distribution, repeater operation, and quantum teleportation.

Finally, we study quantum computing systems that use the cross-Kerr nonlinearity between single-photon qubits and a coherent mode of light. The coherent beam serves a mediating role in coupling two weak single-photon beams. We analytically study this structure using a continuous-time formalism for the cross-Kerr effect in optical fibers. Our results establish stringent conditions that must be fulfilled for the system's proper operation.

Thesis Supervisor: Jeffrey H. Shapiro
Title: Julius A. Stratton Professor of Electrical Engineering

## Acknowledgments

First and foremost, I would like to express my sincere gratitude towards my supervisor, Professor Jeffrey H. Shapiro, for his support, encouragement, and patience during my Ph.D. career. I enjoyed working with him, with all his considerate, thoughtful principles, and learning from him, with his vast knowledge about all aspects of my work. His brilliant supervision, as he knew every single step that I had to take, is behind all my achievements in these five years. I feel so blessed to be in touch with so many exceptional geniuses throughout my life, and particularly here at MIT. I have been very fortunate to have two of these outstanding scientists on my Ph.D. committee, Professor Isaac Chuang and Professor Seth Lloyd, whose support and comments helped me improve this thesis. I am also indebted to Professor Selim Shahriar from Northwestern University, for introducing me to the cavity-quantum-electrodynamics analysis, and to Professor Mikhail Lukin, and two of his students Mohammad Hafezi and Liang Jiang, from Harvard University, for helping me learn atomic physics. Dr. Franco Wong was always present to answer my silly questions, those that I was embarrassed to ask my supervisor, and I learned a lot from his experimental perspective, of which I am appreciative. I enjoyed discussions with my group-mates at MIT, Baris Erkmen, Brent Yen, Chris Kuklewicz, Danial Lashkari, Elliott Mason, Etty Lee, Gaétan Messin, Joe Aung, Lorenzo Maccone, Marco Fiorentino, Marius Albota, Onur Kuzucu, Saikat Guha, Shane Haas, Taehyun Kim, and Vittorio Giovannetti, on all academic and non-academic topics. I would especially like to thank my office-mate, Baris, for his being so considerate and kind during these five years, as well as Brent, Vittorio, and Lorenzo for their technical support. Jane Dunphy has had a major role in improving my technical writing skills, and she has been always supportive and helpful throughout my career. I would also like to thank Professor Jawad Salehi, my Master's supervisor, for his moral support during my first year at MIT, and most importantly, for his guiding me toward a professional research career. I also feel deeply indebted to my father for his encouraging me, from early years of high school, to prepare myself for the International Mathematics Olympiad. I did not succeed in gaining a berth on the IMO team, however, what I learned during that period was the key to my success in my undergraduate and graduate studies.

Many thanks go to Josephina Lee and Cathy Bourgeois for their kindness and helpfulness as well as for many interesting conversations that I had with them. I would also like to thank Ms. Ameneh Abdi, whom I forgot to acknowledge in my Master's thesis, and I can still remember her sad smile after opening my thesis.

I have shared numerous happy and sad moments with my friends at MIT and elsewhere, which can hardly be expressed and acknowledged in words. I would like to especially thank Mahnaz Maddah and Ali Khakifirooz for their extreme support and kindness during the past three years. Their little star, Setareh, enlightened my life as I was writing this thesis, and I hope some day, when she finds her name in her Uncle Mohsen's strange book, that makes her happy too. Many thanks go to the community in the Math common room/reading room and my Mobydick companions, Mohsen Bahramgiri, Taghi Hajiaghayi, Vahab Mirrokni, with whom I have spent days and nights, as well as Adel Ahanin, Ali Farahanchi, Ali Melli, Eaman Eftekhari, Fardad Hashemi, Hoda Bidkhori, Khanom Rahmani, Maryam Mirzakhani, Mohammad Mahdian, Mohsen Ghasemi, Navid Sabbaghi, Nicole Immorlica, Reza Alam, Reza Seyyedali, Roya Beheshti, Sabri Kilic, Salman Abolfathbeiki, and Sepehr Sarmadi with whom I had many interesting discussions and unforgettable memories. I am particularly grateful to Anya Obizhaeva and Hazhir Rahmandad, with whom I shared a house full of love and joy, Ali Tabaei for his witty repartee, Arash Fazl for his medical care, Mehdi Alighanbari for his always being trustworthy, and Hadi Jorati for his being a shelter when I badly needed one. This last year, I enjoyed a more married style of life by being among Ghazal and Niayesh, Leila and Payam, Mana and Mehdi, Maryam and Saeed, as well as Rosa and Hamed. Last but not least, I'd like to thank Aman, Arash, Arezoo, Bahareh, Basier, Farinaz, Guy, Maral, Maryam, Maziar, Mehdi, Michelle, Mohammad, Nima, Parisa, Payman, Pegah, Rishi, Sara, Shaya, Venkatesh, and Zahra for being kind and helpful to me.

I can hardly express my gratitude towards my family. My mother and father are greatest resources of love and care, from which I have benefited enormously throughout my life. This lately, I was also very fortunate to receive the additional support and love of my parents in law. I owe immensely to my uncle and his family for their love and support during my stay in the States. My lovely sisters, Marzieh with her poetic letters, Razieh with her cheerful laughter, and Mariam with all her care and support, as well as my brothers in law, Afshin, Payman, and Sina, and my cute nephews, Mohsen and Matin, are my precious treasures.

This last year of my Ph.D. was truly the best of year of my life as I shared it with my beloved wife, Sanaz. This thesis is dedicated to her for all her support, kindness, patience, and encouragement throughout this time.

This work was supported by the Department of Defense Multidisciplinary University Research Initiative program under Army Research Office grant DAAD-19-00-1-0177, and by the MIT-HP Alliance.

# Contents

# Chapter 1

# Introduction

Possibilities for revolutionary improvements in computation, measurement, and secure communication have motivated physicists, mathematicians, and engineers to work towards harnessing the mysterious features of quantum mechanics to build a real functional *Quantum Computer*. A quantum computer, by definition, is an apparatus that controls quantum features of a system and uses them for the sake of computation. Whereas a classical digital computer works in the discrete space of binary numbers, a quantum computer is allowed to use any superposition state in the complex vector space that describes its underlying physical system. Since the initial speculations on the computational capability of fundamental quantum systems [1, 2, 3], such as atoms, molecules, and photons, many efforts have been taken to implement a scalable quantum computing system. This is required to perform the first promising applications of quantum computers, the Shor's [4] and the Grover's [5] algorithms, which outperform, respectively, any known classical algorithms for factoring and searching. Practical applications of these algorithms will require large quantum computers—measured in terms of the number of quantum bits (qubits) they can process—which are still years away from realization. There are other quantum information applications, however, that may not need a large quantum computing system, and hence may be realized fairly soon [6, 7, 8, 9]. Among this latter group, distributed or networked applications of quantum information processing may provide an excellent route for the initial deployment and attendant continuing development of this new technology. These applications mostly rely on our ability to transport a quantum state, i.e., they depend on *Quantum Communication.*

Quantum communication is the transferring of a quantum state from one place to another. Over short distances, quantum communication becomes the quantum wires of a quantum computer. Over long distances, quantum communication enables the networking of quantum computers. This allows us to employ several few-qubit processors, possibly based on different technologies each offering its own distinct capabilities, to handle more challenging computational tasks.

Quantum communication is not, however, as easy as it sounds. Physical transportation of the quantum system is not a viable solution for long-distance quantum communication because the interaction of the system with its environment changes the system state. The only feasible physical elements that can carry quantum information over long distances are electromagnetic waves, or their constituents, photons. Photons may be lost, however, en route to the channel output. It is also impossible to send an unknown quantum state via classical communications, because any measurement on that state destroys it without providing enough information to reproduce it [10]. Furthermore, quantum mechanics does not permit cloning of an unknown quantum state [11, 12, 13], thus precluding a multi-measurement experiment to completely determine information sufficient to reconstruct an input quantum state for transmission via a classical channel. Long-distance quantum communication *does* have a solution, first derived by Bennett et al. [14], one that is based on one of the most mysterious features of quantum mechanics, namely, *Quantum Entanglement*.

Entanglement is a quantum resource by which two parties share a joint state that cannot be written in a tensor-product form. This state provides a stronger-than-classical correlation between two quantum systems by which one can perfectly infer quantum measurement results made on one system by observing the results of quantum measurements made on the other. This quantum correlation is the main idea behind *teleportation*: the Bennett et al. protocol for quantum communication. In this protocol, entanglement serves as a quantum wire; once established, it can be used for a one-time communication between the transmitter and the receiver.

Let's review the teleportation protocol for the simplest quantum data unit to be transferred, i.e., a *qubit*. A qubit is a vector in a 2-dimensional Hilbert space. An arbitrary qubit in the space spanned by the orthonormal basis $\{|e\rangle, |g\rangle\}$ can be represented as $|\psi\rangle = \alpha|e\rangle + \beta|g\rangle$, where $\alpha$ and $\beta$ are complex numbers that satisfy $|\alpha|^2 + |\beta|^2 = 1$. The purpose of the qubit teleportation is to transfer the above state from point $A$, which stands for Alice, to point $B$, for Bob, as shown in Fig. 1-1. The first step toward this end is *Entanglement Distribution*:

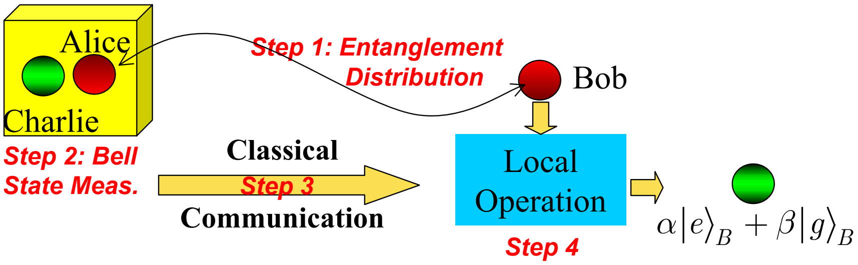

Figure 1-1: Schematic diagram for qubit teleportation. Charlie has an arbitrary unknown quantum state $\alpha\,|e\rangle_C + \beta\,|g\rangle_C$ to be transferred from Alice to Bob. Alice and Bob have initially shared a singlet state. Alice performs a Bell state measurement on her own and Charlie's systems, and sends the result to Bob via a classical communication system. Bob then performs a unitary transformation on his own system, selected in accord with the classical information that he receives from Alice, to reproduce Charlie's initial state.

providing Alice and Bob with an entangled state to share. This state can be any of the following four maximally-entangled Bell states:

$$|\psi^{\pm}\rangle_{AB} = \frac{|g\rangle_A\,|e\rangle_B \pm |e\rangle_A\,|g\rangle_B}{\sqrt{2}} \quad\text{and}\quad |\phi^{\pm}\rangle_{AB} = \frac{|g\rangle_A\,|g\rangle_B \pm |e\rangle_A\,|e\rangle_B}{\sqrt{2}}\,. \tag{1.1}$$

Suppose we have provided Alice and Bob with the singlet state $|\psi^-\rangle_{AB}$ for their use in accomplishing teleportation. Then the initial state of the system comprised of the joint state of Alice, Bob, and Charlie's unknown qubit (to be transferred) is as follows:

$$|\psi\rangle_{ABC} = (\alpha\,|e\rangle_C + \beta\,|g\rangle_C)(|g\rangle_A\,|e\rangle_B - |e\rangle_A\,|g\rangle_B)/\sqrt{2}\,. \tag{1.2}$$

Using

$$|gg\rangle_{CA} = \frac{|\phi^+\rangle_{CA} + |\phi^-\rangle_{CA}}{\sqrt{2}} \quad\text{and}\quad |eg\rangle_{CA} = \frac{|\psi^+\rangle_{CA} - |\psi^-\rangle_{CA}}{\sqrt{2}}\,, \tag{1.3}$$

and two other similar relations for $|ee\rangle_{CA}$ and $|ge\rangle_{CA}$, one can rewrite (1.2) in the following form

$$\begin{aligned} |\psi\rangle_{ABC} &= \frac{1}{2}\left[|\psi^+\rangle_{CA}\,(\alpha\,|e\rangle_B - \beta\,|g\rangle_B) - |\psi^-\rangle_{CA}\,(\alpha\,|e\rangle_B + \beta\,|g\rangle_B)\right] \\ &+ \frac{1}{2}\left[|\phi^-\rangle_{CA}\,(\beta\,|e\rangle_B + \alpha\,|g\rangle_B) + |\phi^+\rangle_{CA}\,(\beta\,|e\rangle_B - \alpha\,|g\rangle_B)\right]\,. \end{aligned} \tag{1.4}$$

It is now clear that when Alice performs the Bell-state measurement (BSM), governed by the states $\{|\psi^{\pm}\rangle_{CA}, |\phi^{\pm}\rangle_{CA}\}$, she projects Bob's state to one of four linearly transformed versions of Charlie's initial state. Thus when Alice performs the BSM and sends her measurement result to Bob via classical communications, he knows exactly which transformation (single-qubit rotation) to apply in order to reproduce Charlie's qubit. These last three steps comprise the *processing* stage of teleportation, all shown schematically in Fig. 1-1.

The main trick in the teleportation protocol is that we have connected Alice and Bob, via entanglement, before sending Charlie's qubit. This way, we need not worry about the channel loss or physical transportation of a qubit once we have established entanglement. This idea can also be used for computational purposes, either within a quantum computer [15] or for distributed quantum processing [16]. In the latter case, distributed entanglement serves as a computational resource. In all these applications, we ought to worry, however, about how to generate, distribute, and maintain entanglement over long distances, i.e., distances over which our physical qubits undergo decoherence. (Short-distance communication has been accomplished with trapped ions [8, 9].) We should also figure out how we can perform a BSM or any other operations that we need on our physical qubits. Solving these problems is crucial to any system that uses entanglement as a resource.

In response to the above concerns, we recognize that, for long-distance applications, there are two inevitable elements to a communication system. The first is an element to store and process the entangled state, which we call a *standing* qubit or a *quantum memory* unit, and the other is a *flying* qubit, which can travel between these units and carries the entanglement. The prime candidate for the latter is a photon in the infrared regime. In this regime, we can use the parametric downconversion process to generate entangled photons [17, 18, 19, 20], and we can transport them via either low-loss fiber or free-space optics. A photon can carry a qubit either in the form of polarization, or photon number, and single-qubit operations can then be realized using wave plates and beam splitters. Photons are not necessarily good candidates for standing qubits, however. First of all, a photon may be lost, in which case we are limited to conditional protocols. Even if we have lossless components, a fully optics-based system may not be an ideal solution to quantum communication because nonlinear interactions between two photons are so weak that we cannot easily perform a full BSM or any other two-qubit operation. It is also impossible to come up with a linear optical BSM device [21], unless we embed our Bell states in a larger Hilbert space, which, unfortunately, reduces the generality and scalability of our BSM device [22, 23].

There are attractive candidates for quantum memory units in the metastable levels of some atomic systems that can interact with the light, and store the photon number

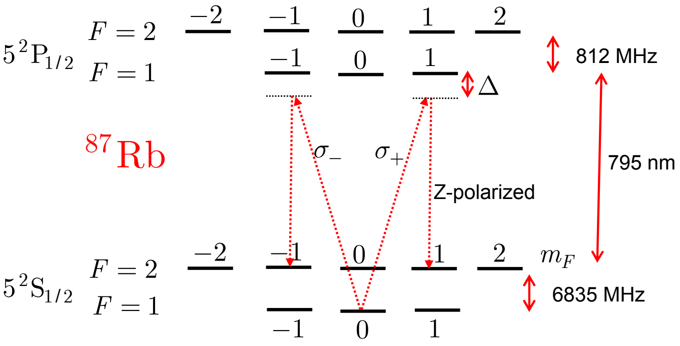

Figure 1-2: Schematic representation of rubidium-atom hyperfine levels. The lower levels ($5^2S_{1/2}$) are attractive venues for standing qubits. Incoming light with an appropriate wavelength ($\approx 795$ nm) can interact with a rubidium atom in its ground state ($5^2S_{1/2}, F = 1, m_F = 0$). The right-circular ($\sigma_+$) and left-circular ($\sigma_-$) components of the light take the atom to different excited states in $5^2P_{1/2}$. By the aid of a $z$-polarized control beam, we can coherently transfer the state of the atom to the metastable levels at $5^2S_{1/2}, F = 2, m_F = 1$ and $5^2S_{1/2}, F = 2, m_F = -1$, respectively. We may use a detuning $\Delta$ in order to mitigate the decoherence effect due to spontaneous emission.

information or the polarization state. The two most popular choices are rubidium and cesium. Figure 1-2 shows the hyperfine levels of a rubidium atom. The levels represented by the $5^2S_{1/2}$ orbital are the ground and metastable levels of the atom. Because of their low energy and their stability, they have long lifetimes, which makes them appropriate for quantum processing. The upper states, represented by the $5^2P_{1/2}$ orbital are excited states of rubidium, and they can be used for transitions between lower atomic states, as well as for interactions between light and the atom. By means of dipole interactions [24], an atom can interact with an incoming photon whose energy is almost equal to the energy gap between the excited and the ground states. Because of the selection rules [25], light beams with different polarizations can only drive certain transitions. For instance, if our rubidium atom is in its ground state $5^2S_{1/2}, F = 1, m_F = 0$, then a right-circularly ($\sigma_+$) polarized light of proper frequency, can only take it to the excited state $5^2P_{1/2}, F = 1, m_F = 1$. If we have a left-circularly ($\sigma_-$) polarized light of proper frequency, then it drives the transition to the excited state $5^2P_{1/2}, F = 1, m_F = -1$. So, because the atom reacts differently to two orthogonal polarizations it can store polarization information. The only problem with our method so far is our leaving the atom in its excited state, whose lifetime is much shorter than what needed for communication or computation purposes. The remedy to this problem is a $z$-polarized control beam that drives a second transition from the upper states to lower metastable levels; see Fig. 1-2. In order to avoid spontaneous emission from the

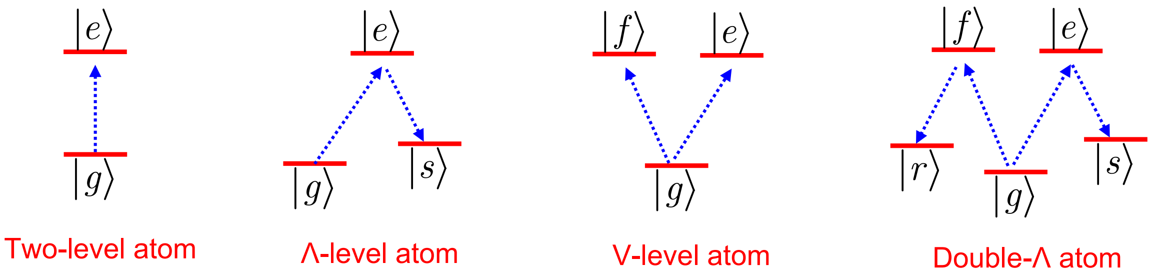

Figure 1-3: Different atomic configurations for a quantum memory. Two-level and $V$-level atoms are simplified versions of the more realistic $\Lambda$-level and double-$\Lambda$-level configurations. The former can store photon-number information, while the latter can maintain polarization information as well.

upper states, we may use a detuning $\Delta$ for the driving beams. This procedure is called an off-resonant Raman transition and is at the heart of many proposals for atomic quantum memories [26, 27, 28, 29, 30].

In quantum communication, we are typically interested in the interaction of weak light, e.g., a single photon, with an atomic system. The strength of this interaction is usually expressed in terms of its Rabi frequency, which is proportional to the optical field amplitude as well as some atomic parameters. For a single atom in free space, this interaction is generally weak, and it can hardly be used for any practical purposes. There are two ways to enhance this interaction. In one approach, based on cavity quantum electrodynamics, a single atom is trapped in a small high-finesse cavity. The effective field amplitude for a single photon is then increased because of confining its energy to the small volume of the cavity. The resulted module is a trapped-atom quantum memory, whose response to single-photon states will be discussed in detail in Chapter 2. Figure 1-3 shows different atomic configurations that we will consider. This includes all possible configurations that can be deduced from Fig. 1-2 for storing either photon-number information (two-level and $\Lambda$-level atoms) or polarization states ($V$-level and double-$\Lambda$ atoms).

The second approach to enhancing light-matter interaction is by increasing the number of atoms that are interacting with the incoming light. Chapter 4 deals with a quantum communication system that uses atomic ensembles for its quantum memories. This system—first proposed by Duan, Lukin, Cirac, and Zoller (termed DLCZ, hereafter)—has the advantage of not dealing with the difficulty associated with trapping and cooling a single atom and can be realized and operate in the bad-cavity regime. It is not, however, without its own drawbacks, as will be seen from our quantitative analysis of its performance in Chapter 4.

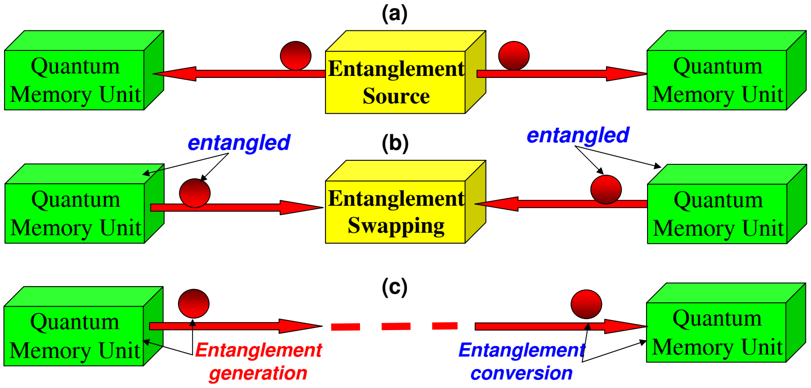

Figure 1-4: Three architectures for entanglement distribution: (a) To-the-memory architecture, in which two entangled photons, generated at the source, carry the entangled state to the QMUs and load them with this state. (b) From-the-memory architecture, in which by the use of a common source, each QMU generates a flying qubit entangled with itself. We can swap the entanglement by performing a BSM on the photons, at the midpoint, which leaves the QMUs in an entangled state. (c) Memory-to-memory configuration, in which we first generate a flying qubit entangled with one of the memories. We let this flying qubit propagate and load the other QMU, i.e., transfer its state to that memory.

Having commented on possible standing and flying qubits, let's return to our main problem, i.e., entanglement distribution. There are three commonly suggested approaches for long-distance entanglement distribution. They are shown schematically in Fig. 1-4. In the first approach, we produce a pair of entangled photons at an optical source, and let the photons travel to and be stored in the quantum memory units (QMUs). This is how a group of researchers from the Massachusetts Institute of Technology (MIT) and Northwestern University (NU) have proposed distributing entanglement. Their system—termed MIT-NU hereafter—uses the trapped-rubidium-atom quantum memories in conjunction with the above to-the-memory scheme for entanglement distribution. In Chapter 3, we review the results obtained for the MIT-NU architecture and extend our results in Chapter 2 to find, for the first time, the entanglement loading probability, viz., the probability of transferring the entangled state of photons to trapped rubidium atoms. In the second approach, we use the idea of entanglement swapping [31] to distribute the entanglement. According to entanglement swapping, if bipartite systems $A$-$C$ and $D$-$B$ are each maximally entangled, we can entangle $A$ and $B$ by performing a BSM on $C$ and $D$. Suppose we generate entanglement between a standing qubit and a flying qubit at location $A$ and do the same at location $B$. We can then let the photons travel to the midpoint between $A$ and $B$ at which a BSM apparatus destroys them, leaving the QMUs at $A$ and $B$ in an entangled state. The DLCZ scheme is an example of this approach; it will be described and analyzed in Chapter 4. For the sake of completeness, in Fig. 1-4(c), we have shown the third approach to distributing entanglement. In this approach, which is a combination of the previous methods, we generate a single photon entangled with one of the QMUs, and let this photon propagate and load the other QMU. There are several groups who are employing this architecture [26, 32], and we will refer to their work in different chapters.

Whereas the nonlinear interaction between single photons is weak, a single photon could possibly induce a measurable amount of phase shift on a *strong* coherent beam. A group of researchers in Hewlett-Packard (HP) Laboratories made this idea the foundation for their proposed universal set of distributed gates [33, 34]. These gates are called distributed because the coherent beam serves as a *bus*, which interacts with and couples different single-photon qubits as it propagates. The main advantage of the HP Laboratories proposal is its viable optics-based implementation with no need for quantum memory units. Ideal cross-Kerr nonlinearity, which is another manifestation of light-matter interactions, is at the core of their system. This kind of nonlinearity can be modeled from different perspectives. One may consider the medium as an ensemble of atoms, which is illuminated by a single photon in one spatial mode, and by a coherent beam in another spatial mode or polarization. The analysis of this system requires the same type of analysis that we will employ in Chapters 2–4. The medium can, however, be a bulk material, such as an optical fiber, in which case atoms are bound to their environments, and the system behavior can better be understood through input-output relationships. In Chapter 5, we employ such a quantum formalism for a cross-Kerr medium [35] to analyze the performance of the HP Laboratories distributed parity gates. Our results reveal some hitherto unexpected limits on the efficiency and practicality of this approach.

Chapter 6 summarizes the principal original contributions that will be made in this thesis. In brief, these contributions are as follows:

- We employ a system-reservoir approach to quantify the interaction of single photons with single atoms trapped in high-finesse optical cavities. We propose a non-adiabatic mechanism for loading such trapped-atom quantum memories, and compare this loading mechanism to two previously known methods for adiabatic passage in terms of their dependence on the atom-light coupling rate, input bandwidth, and cavity decay rate.

- We analyze the MIT-NU entanglement distribution problem in which two trapped rubidium atoms are loaded by a pair of polarization entangled photons [30]. We obtain analytical results for the loading probability in the cases of adiabatic and non-adiabatic loading.

- We perform a Gaussian-state analysis of the DLCZ system [29] that takes the deteriorating effects of multiple excitations and loss into account. Our analysis also treats the effects of other sources of error, such as asymmetry in the path loss and phase offset. We compare the fidelity and the throughput achieved by the DLCZ entanglement distribution protocol with that of the MIT-NU architecture. We also derive the fidelity that can be achieved by the DLCZ repeater and teleportation protocols using resolving and non-resolving photodetectors.

- We apply a quantum model for continuous-time cross-phase modulation to analyze the distributed parity gate proposed by the HP Laboratories [33]. Our model uses an input-output field-operator formalism that associates a non-instantaneous causal response function with the nonlinear medium and a phase noise term with the output field.

All the methods that we will employ in this thesis are based on our basic understanding of physics, and they should be applicable to a range of other problems in quantum optics and quantum computation. Some of these problems, which will constitute possible future directions for extending the results of this thesis, will be described in Chapter 6.

# Chapter 2

# Trapped-atom Quantum Memories: Single Atoms in Optical Cavities

A quantum memory is a basic unit of a quantum computer that ideally has the following three fundamental properties. First, it should reliably maintain its state for a period of time that is much longer than that of a quantum gate operation. Second, it should be possible to perform quantum gate operations inside the memory. Finally, it should be easily accessible for writing quantum data into it and reading quantum data out of it. For all the methods introduced and shown in Fig. 1-4 for entanglement distribution, the last task is of crucial importance. In particular, in some realizations of the to-the-memory configuration [30] as well as that of the memory-to-memory configuration [26], we are interested in transferring the state of single photons to single trapped atoms. In this chapter, we study this problem—which we refer to by the term *loading* (a quantum memory)—by considering each of the quantum memories shown in Fig. 1-3. Of particular interest is finding a mechanism that optimizes loading performance by choice of various system parameters, such as the input photon bandwidth and the atom-light coupling rate. In this chapter we propose a new non-adiabatic loading mechanism and find analytical solutions for its respective loading probability. We also compare our proposed method with previously proposed adiabatic loading mechanisms [26, 28]. Our analysis reveals a trade-off between the required coupling rate and the input photon bandwidth, for both adiabatic and non-adiabatic mechanisms, which is of practical importance.

A quantum memory, in general, is an *open* quantum system. Whereas for the purpose of storage, we desire a memory that does not interact with the outside world, for the purpose of writing into the memory, we definitely need the memory to couple to an external source. However, even in the latter problem, the system consisting of the quantum memory and its driving source can be modeled as a larger *closed* system. To analyze such a large system, we initially try to eliminate the external drive and find a series of equations that model the evolution of our system of interest. The latter, in our case, is the cavity and its trapped atom.

There are two methods for analyzing open quantum systems. In one approach, we write down the most general state for the entire system, typically consisting of a reservoir of harmonic oscillators that are linearly coupled to a field operator in the cavity, and solve the Schrödinger equation for this state. In the other approach, we use Heisenberg equations of motion to find out the evolution of system operators. In Section 2.1, we describe both these methods for the simple case of a cold cavity, viz. an optical cavity which has no atom therein, illuminated by a single photon. This also provides us with a general guideline for dealing with decay processes into a continuum of modes that will be used in the forthcoming sections.

Other problems that will be discussed in this chapter are related to loading a *hot cavity*—which, as opposed to a cold cavity, is an optical cavity with a trapped atom therein[1]. In each of these problems, we are trying to obtain an *analytical* solution to the system loading probability, i.e, the probability of successfully transferring the state of the photon to the atom. In Section 2.2 we analyze a two-level atom trapped in an optical cavity driven by an external single-photon source. This is the most basic quantum memory of Fig. 1-3, and it will turn out that most of other configurations in this figure have an equivalent two-level counterpart. In Section 2.3, we consider the loading of a $\Lambda$-level atom, by first reviewing the traditional adiabatic passage approach [36], and then, comparing it to a simpler approach that we propose. Section 2.4 considers the last two quantum memories in Fig. 1-3, and proves that they are equivalent to simpler configurations. In all these problems, we employ a system-reservoir approach, based on the work of Gardiner and Collett [37], to find the Schrödinger equations of motion for the system that includes trapped atoms, single-mode

---

[1] Our terminology for cold and hot cavities is in accordance with the language of the laser community rather than that of atomic physics. Either way, neither of these terms refers to the actual temperature in the cavity. In fact, in order to trap an atom in a cavity (hot-cavity case) we need to cool the atom to near zero Kelvin, as opposed to what the term *hot* cavity suggests.

single-ended optical cavities, and driving optical sources. It is possible to obtain the same results using Heisenberg equations of motion. It turns out, however, that in some cases this could be a very cumbersome task. In Appendix A, we show the equivalence of these two methods, and outline alternative derivations for the problems that we consider in this chapter using the latter approach.

## 2.1 A two-level system driven by a single-excitation source

Suppose we have a single-ended optical cavity illuminated by a single-photon source, through the partially reflecting mirror, in a specific spatial and polarization mode matched to the cavity's mode of interest. We assume that the incoming light has such a narrow bandwidth that only this particular mode of the cavity may be excited. The loading event in this case is to have one single photon in the cavity mode. This is a special case of a more general situation in which a two-level system is interacting with a reservoir of modes. The driving source can be modeled by a set of annihilation operators $\hat{a}_\omega$, each corresponding to a different temporal (spectral) mode of frequency $\omega$, that satisfy $[\hat{a}_\omega, \hat{a}^\dagger_{\omega'}] = \delta(\omega - \omega')$, [38]. We assume that the driving field is initially in the following single-photon state

$$|\psi_0\rangle = \int d\omega \phi(\omega)\, |1_\omega\rangle, \tag{2.1}$$

where $\int d\omega |\phi(\omega)|^2 = 1$, and $|1_\omega\rangle = \hat{a}^\dagger_\omega |\mathbf{0}\rangle_R$, where $|\mathbf{0}\rangle_R$ is the multi-mode vacuum state, is the multi-mode state representing one photon at frequency $\omega$ and vacuum state in all other modes. Here and elsewhere in this chapter, we assume that the initial time is before occurrence of any possible interactions between the source and the cavity. For simplicity, and without loss of generality, we assume that this initial time is 0. We will relax this assumption after obtaining our final result.

The Gardiner-Collett Hamiltonian for the above cold-cavity system can be written as follows[2]:

$$\hat{H}_{cc} = \hbar \int d\omega\, \omega \hat{a}^\dagger_\omega \hat{a}_\omega + \hbar\omega_0 \hat{b}^\dagger \hat{b} + \hbar\Gamma \int d\omega (\hat{a}^\dagger_\omega \hat{b} + \hat{b}^\dagger \hat{a}_\omega), \tag{2.2}$$

---

[2] This is a phenomenological approach to modeling the cavity and its incoming/outgoing fields to capture the idea that a photon in the cavity should leak out to a continuum of states representing each epoch of time. In other words, we can associate a temporal, and, correspondingly, a spectral pulse shape with the photon packet that leaves the cavity, and that leads us to defining a continuum of operators $\hat{a}_\omega$ to model the reservoir. This model agrees with more rigorous models, up to the first order in the mirror transmissivity, in the regime of high-$Q$ cavities [39].

where $\hat{b}$ represents the annihilation operator associated with the cavity mode of frequency $\omega_0$, initially in the vacuum state, and $\Gamma$ is the frequency-independent, but possibly time-dependent[3], coupling constant that connects the external world to the cavity. Because of the source's narrow bandwidth, we can and will assume that all integrals in (2.2) run from $-\infty$ to $+\infty$. Then, because there is exactly one excitation in the entire system, the system's quantum state as a function of time can be written as

$$|\psi(t)\rangle = \int d\omega \alpha_\omega(t)|1_\omega\rangle|0\rangle_b + \beta(t)|\mathbf{0}\rangle_R|1\rangle_b, \tag{2.3}$$

where $|k\rangle_b$ represents the $k$-photon Fock state of the cavity mode. Using the Schrödinger equation, $i\hbar|\dot{\psi}(t)\rangle = \hat{H}_{cc}|\psi(t)\rangle$, we derive

$$\begin{aligned} i|\dot{\psi}(t)\rangle &= \int d\omega\, \omega\alpha_\omega(t)|1_\omega\rangle|0\rangle_b + \omega_0\beta(t)|\mathbf{0}\rangle_R|1\rangle_b \\ &+ \Gamma(t)\int d\omega\, \beta(t)|1_\omega\rangle|0\rangle_b + \Gamma(t)\int d\omega\alpha_\omega(t)|\mathbf{0}\rangle_R|1\rangle_b, \end{aligned} \tag{2.4}$$

which results in the following set of equations

$$\dot{\alpha}_\omega(t) = -i(\omega\alpha_\omega(t) + \Gamma(t)\beta(t)), \tag{2.5a}$$

$$\dot{\beta}(t) = -i(\omega_0\beta(t) + \Gamma(t)\textstyle\int d\omega\, \alpha_\omega(t))\,. \tag{2.5b}$$

Equation (2.5a) can be easily solved to give

$$\alpha_\omega(t) = e^{-i\omega t}\alpha_\omega(0) - i\int_0^t d\tau\Gamma(\tau)e^{-i\omega(t-\tau)}\beta(\tau), \tag{2.6}$$

where, in our case, $\alpha_\omega(0) = \phi(\omega)$. By employing this result, as well as $\int d\omega \exp(-i\omega(t-\tau)) = 2\pi\delta(t-\tau)$ and $\int_0^t d\tau\Gamma(\tau)\beta(\tau)\delta(t-\tau) = \Gamma(t)\beta(t)/2$, in (2.5b), we obtain

$$\dot{\beta}(t) = -i\omega_0\beta(t) - i\sqrt{2\kappa(t)}\Phi(t) - \kappa(t)\beta(t), \tag{2.7}$$

where $\kappa \equiv \pi\Gamma^2$ is the cavity decay rate, and $\Phi(t) = \int d\omega e^{-i\omega t}\phi(\omega)/\sqrt{2\pi}$ is the temporal pulse shape associated with the incoming photon. Equation (2.7) summarizes, in a compact

---

[3] It is not typically the case that $\Gamma$ is a function of time. However, later in this chapter, we will encounter a problem in which $\Gamma$ is time dependent. In general, unless we explicitly mention this time dependence, we assume that $\Gamma$ and later $\kappa$ are both time independent.

form, the main characteristics of the interaction of a two-level system with a bath of field operators. The first term on the right-hand side of (2.7) is the Hamiltonian evolution of the two-level system in the absence of any decay to the reservoir. The second term models the system evolution in the presence of a driving source, and the third term stands for the cavity decay to the reservoir. Equation (2.7) provides us with a prescription to circumvent the reservoir variables and just study our system of interest. For instance, suppose that there is a single atom in the cavity, which interacts *strongly* with only one of the cavity modes and *weakly* with all other non-cavity modes. The latter, in our context, can be modeled via a decay rate $\gamma$ with no driving force. We will encounter this example later in this chapter.

Equation (2.7) can be solved to obtain

$$e^{i\omega_0 t}\beta(t) = e^{-K(t)}\beta(0) - i\int_0^t d\tau\sqrt{2\kappa(\tau)}e^{-K(t)+K(\tau)}\Phi_b(\tau), \tag{2.8}$$

where $K(t) = \int_0^t d\tau\kappa(\tau)$, and $\Phi_b(t) = e^{i\omega_0 t}\Phi(t)$ is the baseband input pulse shape[4]. By using $\beta(0) = 0$ and noting that $P_{loading}(t) = \langle\psi(t)|\hat{b}^\dagger\hat{b}|\psi(t)\rangle = |\beta(t)|^2$, we obtain the following loading probability for the cold-cavity case:

$$P_{loading}(t) = \left|\int_0^t d\tau\sqrt{2\kappa(\tau)}e^{-K(t)+K(\tau)}\Phi_b(\tau)\right|^2. \tag{2.9}$$

Here, we implicitly assume that the driving pulse shape is zero for $t < 0$. This may not be the case for many pulse shapes that we may encounter in practice or we will use in our numerical results. In those cases we need to replace the lower limit in the above integral with an appropriate time before which $\Phi_b(t)$ is effectively zero. Moreover, we have assumed that there is no loss from the optical source to the cavity, i.e., the Hamiltonian evolution of $\alpha_\omega(t)$ is modeled by $\alpha_\omega(0)e^{-i\omega t}$. Therefore, we can model the photon's propagation time, $t_0$, from the source to the cavity by a time shift in $\Phi(t)$. From now on, we assume that $t_0 = 0$.

Note that the set of equations in (2.5) is in the linear form $\dot{\mathbf{X}} = -i\mathbf{A}\mathbf{X}$, where $\mathbf{X}$ is a column matrix representing all amplitude variables (here, $\alpha_\omega(t)$ and $\beta(t)$), and $\mathbf{A}$ is a square matrix representing the mutual coupling rates (here, between $|\mathbf{0}\rangle_R|1\rangle_b$ and $|1_\omega\rangle|0\rangle_b$)[5]. That

---

[4] $\Phi_b(t)$ is a baseband form of $\Phi(t)$ if and only if the central carrier frequency of $\Phi(t)$, $\omega_f$, is equal to $\omega_0$. It is implicitly assumed that $\omega_f \approx \omega_0$ and that the bandwidth of $\Phi_b(t)$ is much less than the cavity free spectral range, so that we can use a single-mode treatment for the cavity analysis.

[5] As a rule of thumb, if the interaction terms in the system Hamiltonian are of the form $\hat{a}\hat{b}^\dagger + \hat{b}\hat{a}^\dagger$, then the evolution of a probability amplitude $a(t)$ associated with the state $|A\rangle$ is given by $\dot{a}(t) = -iE_A a(t) - i\sum_B g_{AB}b(t)$. Here, the sum is over all states $|B\rangle$, with probability amplitudes $b(t)$, that are coupled to $|A\rangle$

makes the system behave linearly in response to its initial state. For instance, assuming that $\phi(\omega) = \phi_1(\omega) + \phi_2(\omega)$, $\beta(t)$ will be equal to $\beta_1(t) + \beta_2(t)$, where $\beta_i(t)$, for $i = 1, 2$, is given by (2.8) if we replace $\Phi_b(t)$ with its corresponding term for $\phi_i(\omega)$, i.e., $\int d\omega \phi_i(\omega) e^{-i(\omega-\omega_0)t}/\sqrt{2\pi}$. By the same token, we can think of the initial state in (2.1) as a superposition of its infinitesimal constituents $d\omega\phi(\omega)|1_\omega\rangle$. For $\beta(0) = 0$, using (2.8), the probability amplitude $\beta_\omega(t)$ associated with these unnormalized states is then given by

$$e^{i\omega_0 t}\beta_\omega(t) d\omega = -i \int_0^t d\tau \sqrt{2\kappa(\tau)} e^{-K(t)+K(\tau)} d\omega \phi(\omega) e^{-i(\omega-\omega_0)\tau}/\sqrt{2\pi}. \qquad (2.10)$$

The original equation (2.8) can then be obtained by integrating the above formula over $\omega$. The above equation will be handy when we deal with the more complicated problems that we will encounter in Chapter 3.

We can alternatively model our loading problem in the Heisenberg picture in which field operators are functions of time, and they are evolving according to the Heisenberg equation $i\hbar\, d\hat{a}/dt = [\hat{a}, \hat{H}_{cc}]$, for any operator $\hat{a}$. We then obtain

$$\begin{array}{c} d\hat{a}_\omega(t)/dt = -i\omega\hat{a}_\omega(t) - i\Gamma(t)\hat{b}(t) \\ \Rightarrow \hat{a}_\omega(t) = e^{-i\omega t}\hat{a}_\omega(0) - i\int_0^t d\tau \Gamma(\tau)\hat{b}(\tau)e^{-i\omega(t-\tau)} \end{array} \qquad (2.11)$$

$$\begin{array}{c} d\hat{b}(t)/dt = -i\omega_0\hat{b}(t) - i\Gamma(t)\int d\omega \hat{a}_\omega(t) \\ \Rightarrow d\hat{b}(t)/dt = -i\omega_0\hat{b}(t) - i\sqrt{2\kappa(t)}\hat{A}_{in}(t) - \kappa(t)\hat{b}(t) \quad , \end{array} \qquad (2.12)$$

where $\hat{A}_{in}(t) = (1/\sqrt{2\pi})\int d\omega \hat{a}_\omega(0)e^{-i\omega t}$. The last equation is the counterpart of (2.7) in the Heisenberg picture. The driving source is now represented by a field operator $\hat{A}_{in}(t)$, which is historically called a Langevin operator [40]. Hence, (2.11) and (2.12) are usually called Heisenberg-Langevin (HL) equations of motion. We can solve for $\hat{b}$ in terms of the Langevin operator to find

$$e^{i\omega_0 t}\hat{b}(t) = e^{-K(t)}\hat{b}(0) - i\int_0^t d\tau \sqrt{2\kappa(\tau)}\hat{A}_b(\tau)e^{-K(t)+K(\tau)}. \qquad (2.13)$$

where $\hat{A}_b = e^{i\omega_0 t}\hat{A}_{in}$ and $\hat{b}(0)$ and $\hat{a}_\omega(0)$ are respectively $\hat{b}$ and $\hat{a}_\omega$ in the Schrödinger picture.

---

with coupling rates $g_{AB}$, and $\hbar E_A$ is the energy associated with $|A\rangle$ with respect to a reference level.

The loading probability is then calculated as follows,

$$\begin{aligned}\left\langle \hat{b}^\dagger(t)\hat{b}(t)\right\rangle &= \int_0^t d\tau \int_0^t d\tau' \sqrt{2\kappa(\tau)}\sqrt{2\kappa(\tau')} e^{-K(t)+K(\tau')} e^{-K(t)+K(\tau)} \left\langle \hat{A}_b^\dagger(\tau)\hat{A}_b(\tau')\right\rangle \\ &= \left| \int_0^t d\tau \sqrt{2\kappa(\tau)} e^{-K(t)+K(\tau)} \Phi_b(\tau)\right|^2 , \qquad (2.14)\end{aligned}$$

where, in the last step, we averaged over $|\psi_0\rangle$ in (2.1) according to the the following formula

$$\begin{aligned}\hat{A}_{in}(t)\int d\omega \phi(\omega)\left|1_\omega\right\rangle &= \frac{1}{\sqrt{2\pi}}\int d\omega' \int d\omega \phi(\omega) e^{-i\omega' t}\hat{a}(\omega')\left|1_\omega\right\rangle \\ &= \frac{1}{\sqrt{2\pi}}\int d\omega' \int d\omega \phi(\omega) e^{-i\omega' t}\delta(\omega'-\omega)\left|\mathbf{0}\right\rangle_R \\ &= \frac{1}{\sqrt{2\pi}}\int d\omega \phi(\omega) e^{-i\omega t}\left|\mathbf{0}\right\rangle_R \\ &= \Phi(t)\left|\mathbf{0}\right\rangle_R . \qquad (2.15)\end{aligned}$$

As can be seen, both methods give rise to the same result. In the subsequent sections, we will only use the simpler system-reservoir approach for the problems of interest. More on the Heisenberg-Langevin treatment will be given in Appendix A.

### 2.1.1 The reverse problem: the cavity decay to the reservoir

So far, we have assumed that there is no excitation in the cavity, and that the cavity is driven by an external source. We can also consider the inverse problem, i.e., that the cavity mode is initially in its single-photon excited state, and find out the reservoir state after the two systems have interacted for a time duration $t$. Because of the time reversibility of closed quantum systems, the answer to this question provides us with the optimum pulse shape for loading the cavity with a single photon. Using $\beta(0) = 1$ and $\Phi(\tau) = 0$ in (2.8), and the result in (2.6), we obtain for a time-independent $\Gamma$

$$\alpha_\omega(t) = -i\Gamma \frac{e^{-i\omega t} - e^{-(\kappa+i\omega_0)t}}{\kappa + i(\omega_0-\omega)}. \qquad (2.16)$$

We can see that the second term in the above equation vanishes at $t \to \infty$; hence, $\alpha_\omega(t)$ takes the form of a Lorentzian pulse shape. This shows that the ideal pulse shape for loading the cavity with a single photon is exponentially rising.

### 2.1.2 Exponential pulse shapes: numerical results

It is interesting to find the loading probability in (2.9) for a general, finite-duration exponential pulse with rate $\lambda$ in the following form

$$\Phi(\tau) = \sqrt{\frac{2\lambda}{e^{2\lambda T} - 1}} e^{(-i\omega_0 + \lambda)\tau} \quad , \quad 0 \leq \tau \leq T \, . \tag{2.17}$$

[Note that we will allow $\lambda$ to be either positive (exponentially-rising pulse) or negative (exponentially-decaying pulse).] The resulting loading probability for this pulse is as follows:

$$\begin{aligned} P_{loading}(t) &= \begin{cases} \frac{4\kappa\lambda}{(\lambda+\kappa)^2} \frac{(e^{\lambda t} - e^{-\kappa t})^2}{e^{2\lambda T} - 1} \, , & 0 \leq t \leq T \, , \\ e^{-2\kappa(t-T)} P_{loading}(T) \, , & t > T \, , \end{cases} \\ &= \begin{cases} \frac{4(\kappa T)(\lambda T)}{(\lambda T + \kappa T)^2} \frac{(e^{(\lambda T)(t/T)} - e^{-(\kappa T)(t/T)})^2}{e^{2\lambda T} - 1} \, , & 0 \leq t \leq T \, , \\ e^{-2(\kappa T)(t/T - 1)} P_{loading}(T) \, , & t > T \, . \end{cases} \end{aligned} \tag{2.18}$$

It can be seen from the above equations that, using a finite-width input pulse, the system evolution has two stages: the loading stage and the decaying stage. For $t > T$, i.e., after the input pulse has ended, the system has a purely decaying behavior. Therefore, the system loading probability peaks somewhere in the interval $0 \leq t \leq T$. The maximum success probability is a function of $\lambda T$ and $\kappa T$. To find the optimum rate for the pulse, we can apply the Cauchy-Schwarz inequality to (2.9) to show that

$$\begin{aligned} P_{loading}(t) &\leq \int_0^t d\tau \left| \sqrt{2\kappa} e^{-\kappa(t-\tau)} \right|^2 \int_0^t d\tau \, |\Phi(\tau)|^2 \\ &\leq 1 - e^{-2\kappa t}, \end{aligned} \tag{2.19}$$

where equality is achieved at $t = T$ by an exponentially-rising pulse shape with rate $\lambda = \kappa$. This is intuitively correct: if we start with a photon in the cavity, it decays exponentially out of the cavity. Now, if we move backward in time, we need an exponentially-rising input pulse in order to load the cavity with the photon. From (2.18), with $\lambda = \kappa$, the loading probability is a function of $\kappa T$. In this case, from (2.19), lower decay rates will require longer pulses in order to realize near-unity loading probabilities.

It is interesting, however, that even an exponentially-decaying pulse can yield a loading probability as high as 81%. In this case, $\lambda$ is negative, and the loading probability in (2.18),

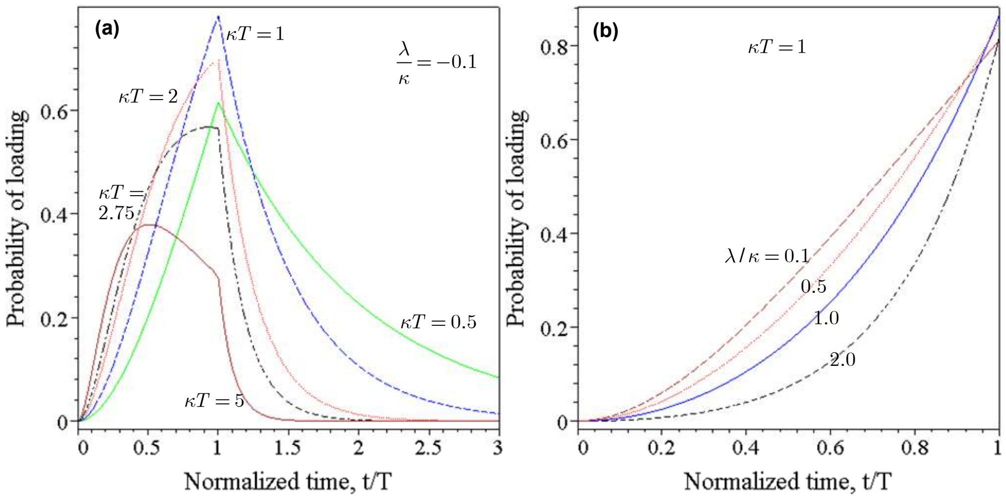

Figure 2-1: Loading probability, $\langle \hat{b}^\dagger(t)\hat{b}(t)\rangle$, for a cold cavity illuminated by (a) exponentially-decaying pulse shapes with different values of $\kappa T$, and (b) exponentially-rising pulse shapes with different rate ratios $\lambda/\kappa$.

for $t \leq T$, is comprised of two terms. The first term, $-4\lambda\kappa/(\lambda+\kappa)^2$, takes its maximum, viz. unity, at $\lambda = -\kappa$. This condition, however, forces the second term, $(e^{\lambda t} - e^{-\kappa t})^2/(1 - e^{2\lambda T})$, to zero. This latter term actually takes its maximum for $|\lambda| \ll \kappa$. Hence, for any fixed value of $\kappa T$, there must exist an optimum value for $|\lambda/\kappa|$ that maximizes the loading probability. One strategy then to maximaize the loading probability is to choose a small $|\lambda/\kappa|$, so that the input pulse bandwidth is mostly determined by $T$, and then try to find the optimum $\kappa T$. This way, numerically, it can be shown that $\langle \hat{b}^\dagger(T)\hat{b}(T)\rangle$ can be as high as 0.8145.

Figure 2-1 plots some loading probability examples. In Fig. 2-1(a), we have plotted the loading probability for an exponentially-decaying pulse shape with $\lambda/\kappa = -0.1$ for different values of $\kappa T$. It is clear from this figure that for this value of $\lambda/\kappa$ there exists an optimum value (close to one) for the product $\kappa T$, as predicted. Figure 2-1(b) shows the loading probability for exponentially-rising pulse shapes with different positive rates $\lambda$. It can be seen that the case of $\lambda/\kappa = 1$ eventually outperforms other cases as $t \to T$, although this is not necessarily the case for $t < T$. Also, for our $\kappa T = 1$ example, an exponentially-decaying pulse shape can be as effective in cavity loading as an exponentially-rising pulse shape. Ease of implementation should then dictate whether to use one or the other of these pulse shapes.

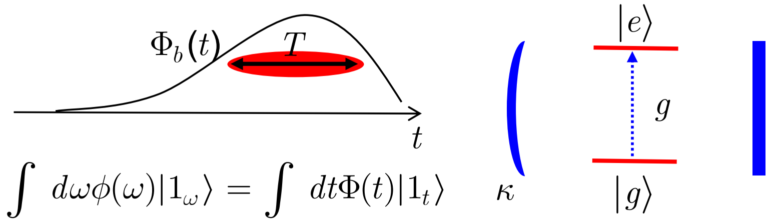

Figure 2-2: A single two-level atom trapped in a single-ended high-finesse optical cavity. A single photon illuminates the cavity at the proper frequency to excite the atom to its upper state.

## 2.2 A two-level atom in an optical cavity driven by a single-photon source

Suppose there is a single two-level atom, with excited state $|e\rangle$ and ground state $|g\rangle$, inside our single-ended high-$Q$ cavity. We assume that the frequency-$\omega_a$ atomic transition between $|e\rangle$ and $|g\rangle$ is coupled, at coupling rate $g$, to the cavity field operator $\hat{b}$ of frequency $\omega_0$. This implies a detuning $\Delta = \omega_0 - \omega_a$, which is assumed to be much less than $\omega_0$. We also assume that $g$ and $\kappa$ are time-independent parameters. In analogy to the previous section, we assume that this trapped-atom module is illuminated by a single photon, as shown in Fig. 2-2. The Hamiltonian for this system is as follows

$$\hat{H}_a = \hat{H}_{cc} + \hbar\omega_a\hat{\sigma}_{ee} + \hbar g(\hat{b}^\dagger\hat{\sigma}_{ge} + \hat{b}\hat{\sigma}_{eg}), \tag{2.20}$$

where $\hat{\sigma}_{ij} = |i\rangle\langle j|$, $i, j \in \{g, e\}$. Now, starting with the atom initially in its ground state and with no excitation in the cavity, the system quantum state has the following form

$$|\psi(t)\rangle = \int d\omega\alpha_\omega(t)|1_\omega\rangle|0\rangle_b|g\rangle + \beta'(t)|\mathbf{0}\rangle_R|1\rangle_b|g\rangle + c'_e(t)|\mathbf{0}\rangle_R|0\rangle_b|e\rangle, \tag{2.21}$$

where we assume that the driving field is in the initial state prescribed by (2.1). The goal of this section is to provide analytical results for the memory loading probability—the probability of absorbing the external photon by the trapped atom—$|c'_e(t)|^2$. Note that the connection between the atom and the driving source is through the cavity mode. We can assume, however, that the atom can spontaneously decay to modes other than the cavity mode with an overall decay rate $\gamma$. Assuming[6] that $\gamma \ll \kappa, g$, and applying the Schrödinger

---

[6] It is not required at this stage to make this assumption. However, it is a reasonable assumption for a quantum memory device, and we will use it later in all our numerical results.

equation to (2.21), we obtain

$$\dot{\beta}'(t) = -i\omega_0\beta'(t) - igc'_e(t) - i\sqrt{2\kappa}\Phi(t) - \kappa\beta'(t), \tag{2.22a}$$

$$\dot{c}'_e(t) = -i\omega_a c'_e(t) - ig\beta'(t) - \gamma c'_e(t), \tag{2.22b}$$

where we have included the results of the previous section to model the decay processes. The above equations can be simplified by defining slowly-varying probability amplitudes $c_e(t) = e^{i\omega_0 t}c'_e(t)$ and $\beta(t) = e^{i\omega_0 t}\beta'(t)$, for which we have

$$\dot{\beta}(t) = -igc_e(t) - i\sqrt{2\kappa}\Phi_b(t) - \kappa\beta(t), \tag{2.23a}$$

$$\dot{c}_e(t) = i\Delta c_e(t) - ig\beta(t) - \gamma c_e(t), \tag{2.23b}$$

where $\Delta = \omega_0 - \omega_a$. Using the Laplace transform, $\tilde{f}(s) \equiv \int dte^{-st}f(t)$, we obtain

$$\tilde{\beta}(s) = \frac{-ig\tilde{c}_e(s) - i\sqrt{2\kappa}\tilde{\Phi}_b(s)}{s+\kappa} \tag{2.24}$$

and

$$\tilde{c}_e(s) = \frac{-\sqrt{2\kappa}g\tilde{\Phi}_b(s)}{s^2 + (\kappa+\gamma')s + g^2 + \kappa\gamma'}\,, \tag{2.25}$$

which results in

$$\beta(t) = -(i\sqrt{2\kappa}/\xi)\int_0^t d\tau\Phi_b(\tau)(\kappa'_+e^{-\kappa_+(t-\tau)} - \kappa'_-e^{-\kappa_-(t-\tau)}), \tag{2.26}$$

$$c_e(t) = (g\sqrt{2\kappa}/\xi)\int_0^t d\tau\Phi_b(\tau)(e^{-\kappa_+(t-\tau)} - e^{-\kappa_-(t-\tau)}), \tag{2.27}$$

where

$$\kappa_\pm = (\kappa + \gamma' \pm \xi)/2, \kappa'_\pm = \kappa_\pm - \gamma',$$
$$\xi = \sqrt{(\kappa+\gamma')^2 - 4(g^2+\kappa\gamma')}, \gamma' = \gamma - i\Delta. \tag{2.28}$$

Similar to what we stated in the previous section, and for further use in the next chapter, we can think of the initial state in (2.1) as a superposition of its infinitesimal constituent states $d\omega\phi(\omega)|1_\omega\rangle$, to which we can associate slowly-varying probability amplitudes $c_{e,\omega}(t)$

given by

$$c_{e,\omega}(t)d\omega = (g\sqrt{2\kappa}/\xi)\int_0^t d\tau d\omega \phi(\omega)e^{-i(\omega-\omega_0)\tau}(e^{-\kappa_+(t-\tau)} - e^{-\kappa_-(t-\tau)})/\sqrt{2\pi}. \tag{2.29}$$

We then have $c_e(t) = \int d\omega c_{e,\omega}(t)$ as obtained in (2.27).

This system-reservoir calculation gives a more compact form for the loading probability, $\langle\hat{\sigma}_{ee}(t)\rangle = |c_e(t)|^2$, than what we will obtain later in (A.25) via the HL equations for the case of on-resonance illumination at $\gamma = 0$. The two results are nevertheless equivalent, and their equivalence can be verified by a tedious algebraic manipulation that we shall omit.

### 2.2.1 The reverse problem: the atomic decay to the reservoir

Similar to the previous section, we can start with the atom in its excited state, the reservoir unexcited, and observe the evolution of the reservoir state. In this case, using the initial conditions $\beta(0) = 0$ and $c_e(0) = 1$, we obtain from (2.23)

$$\tilde{\beta}(s) = \frac{-ig}{s^2 + (\kappa+\gamma')s + g^2 + \kappa\gamma'} \tag{2.30}$$

which results in

$$\beta(t) = (ig/\xi)(e^{-\kappa_+ t} - e^{-\kappa_- t}). \tag{2.31}$$

Plugging the above equation into (2.6), we obtain

$$\alpha_\omega(t) = \frac{\Gamma g e^{-i\omega t}}{\xi}\left[\frac{1 - e^{-[\kappa_+ + i(\omega_0-\omega)]t}}{\kappa_+ + i(\omega_0-\omega)} - \frac{1 - e^{-[\kappa_- + i(\omega_0-\omega)]t}}{\kappa_- + i(\omega_0-\omega)}\right], \tag{2.32}$$

which results in a double-Lorentzian pulse shape as $t \to \infty$.

### 2.2.2 Numerical results

We learned from the cold-cavity loading problem that there is an optimum value of $\kappa T$, where $\kappa$ is the cavity linewidth and $T$ is the width of an exponential pulse, that maximizes the loading probability. That is, for every exponential pulse shape there is a cavity whose linewidth best matches the input bandwidth. In the hot-cavity case, we may expect to see the same filtering behavior modified by the additional effect imposed by the trapped atom. A reasonable parameter to account for possible new effects is $g/\kappa$, which is the ratio between the atom-photon coupling rate and the cavity decay rate. In fact, in the ideal case of $\gamma = \Delta = 0$, (2.27) can be written in terms of dimensionless parameters $\kappa T$, $g/\kappa$, and $t/T$, as follows

$$\begin{aligned} c_e(t) \quad = \quad & \frac{\sqrt{2\kappa T}}{\sqrt{(\kappa/g)^2 - 4}} \int_0^{t/T} du \Phi'_b(u) \times \\ & \left[ e^{-\kappa T(1+\sqrt{1-4g^2/\kappa^2})(t/T-u)/2} - e^{-\kappa T(1-\sqrt{1-4g^2/\kappa^2})(t/T-u)/2} \right], \end{aligned} \tag{2.33}$$

where $\Phi_b(t) = \Phi'_b(t/T)/\sqrt{T}$, i.e., $\Phi'_b(u)$ is a compressed/stretched version of $\Phi_b(t)$, which has unity width, in its normalized time coordinate, and has been normalized to satisfy $\int du|\Phi'_b(u)|^2 = 1$.

Parameters $g/\kappa$ and $\kappa T$ are of implementation importance as well. Assuming $\kappa$ is fixed (it is determined by the reflectivity of cavity mirrors), the required value for $g/\kappa$ determines the length of the cavity; the shorter this length, the higher $g$ will be. Our general conception of atom-light interaction would therefore suggest that higher values of $g$ should result in higher loading probabilities. This is not generally true, as we will see soon. Higher $g$ values are also not desirable from an implementation point of view: the smaller the cavity, the more difficult it becomes to trap and cool the atom. For a fixed $\kappa$, it is the bandwidth of the input pulse shape, $B_0$, that determines $\kappa T$; the higher the desired $\kappa T$, the lower the required $B_0$. The value of $B_0$ is determined by our single-photon source. If the source operation is based on downconversion processes, it has generally a broad bandwidth, ~THz, unless we use cavities for parametric amplification [41]. Thus it is desirable to work at a low value of $\kappa T$, which allows a larger bandwidth, and consequently, a higher flux of single photons to enter the cavity.

Figure 2-3 shows the loading probability for the two-level atom of Fig. 2-2 in the ideal case of no non-cavity decay ($\gamma = 0$) and no detuning ($\Delta = 0$) for a secant hyperbolic pulse shape[7] $\Phi'_b(u) = \sqrt{2}\text{sech}[4(u-1)]$. In this figure, we have fixed the value of $\kappa T$ to 2 and varied the value of $g/\kappa$. It can be seen that there exists an optimum value of $g/\kappa$, which maximizes the loading probability. Higher ratios than this optimum value just increase the Rabi oscillation between the two atomic levels, making it harder to find the atom in its excited state with high probability. By keeping $g$ constant, the process of loading/unloading

---

[7] Our choice of a secant hyperbolic pulse shape in this section is because of mathematical convenience in the subsequent sections. We will show later that the loading probability is only slightly affected by the choice of the pulse shape so long as different pulse shapes have the same bandwidth.

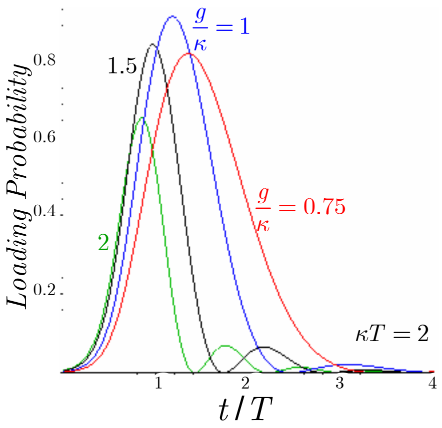

Figure 2-3: Loading probability versus normalized time for $\kappa T = 2$ and a secant hyperbolic pulse shape at $\gamma = \Delta = 0$. Upon arrival of the photon, there is a peak in the loading probability, which occurs at the time that the photon has most likely been absorbed by the atom. This maximum loading probability is a function of $g/\kappa$, and there exists an optimum value for this parameter that maximizes the chance of loading.

the atom continues for several cycles until the photon decays out of the cavity. Hence, by this method we cannot hold the atom in its excited state unless we drive the value of $g$ to zero at an appropriate point in the process, $t = T_{Load}$, when the loading probability attains its maximum. In the next section, we show how we can accomplish this turn-off of the coupling in a $\Lambda$-level atom, in which we can use a control field to vary $g$.

Figure 2-4 shows the optimum value of $g/\kappa$ for different values of $\kappa T$. It also shows the maximum probability that we can achieve as well as the proper time for stopping the process, $T_{Load}$, using $\Phi_b'(u) = \sqrt{2}\mathrm{sech}[4(u-1)]$. It can be seen that the maximum loading probability is above 90% for $\kappa T \geq 2$. It drops off somewhat for larger values of $\kappa T$, but it is still high. It can also be seen that the optimum value of $g/\kappa$, at the highest loading probabilities, is on the order of one. Its value can be driven below one by narrowing the input bandwidth, but the price that we have to pay is an exponential increase in $\kappa T$. For instance (not shown on the graph), to get $(g/\kappa)_{opt} = 0.1$, we need $\kappa T$ to be approximately 100. Finally, we observe that $T_{Load}$ approaches a non-zero asymptote, close to the effective width of our input pulse, as we increase $\kappa T$.

Figure 2-5 shows the loading probability as a function of time for $g/\kappa = 1$ and $\kappa T = 2$, for different pulse shapes of approximately the same effective width. The four different shapes we have used are: a secant hyperbolic pulse; a rectangular pulse; an exponentially-rising pulse; and an exponentially-decaying pulse. The difference between their loading probabilities is

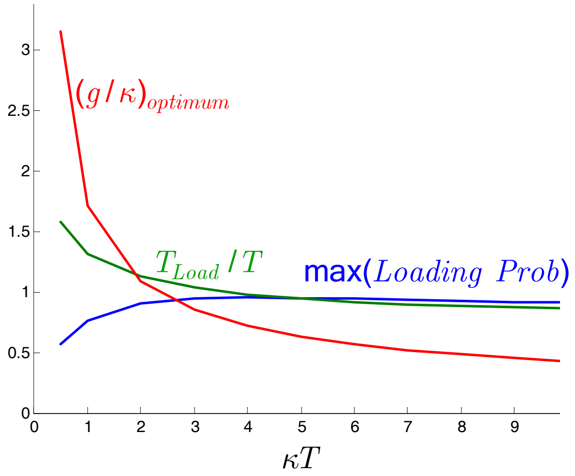

Figure 2-4: Optimum value of $g/\kappa$ versus $\kappa T$. The maximum loading probability obtained at $(g/\kappa)_{opt}$ as well as the corresponding loading time are also shown. All points are obtained for a secant hyperbolic pulse shape $\Phi_b'(u) = \sqrt{2}\text{sech}[4(u-1)]$ and at $\gamma = \Delta = 0$.

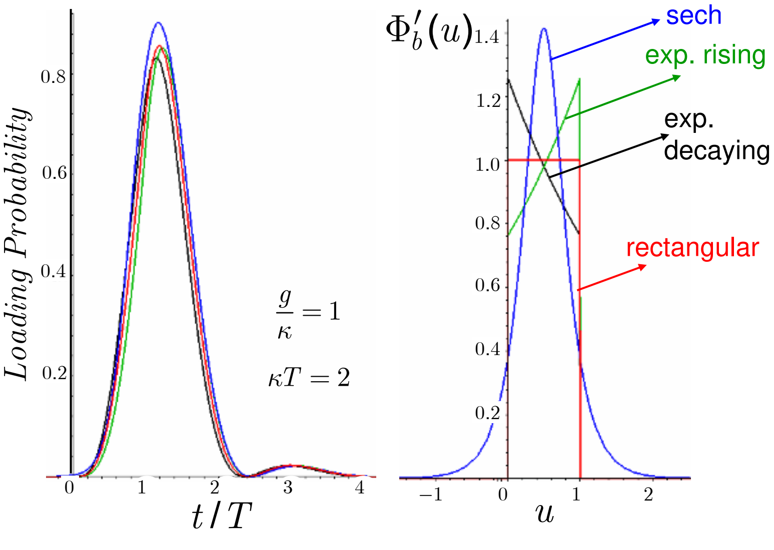

Figure 2-5: Loading probability at $\kappa T = 2$, $g/\kappa = 1$, and $\gamma = \Delta = 0$ for various pulse shapes. The baseband pulse shapes are shown on the right-hand-side graph, and they correspond, with respect to the highest probability that they can achieve, to secant hyperbolic (with the highest peak), rectangular, exponentially-rising, and exponentially-decaying pulse shapes on the left-hand-side graph.

seen to be very minor. It seems that so long as we have matched the input bandwidth to the cavity parameters $g$ and $\kappa$, we can achieve high loading probability regardless of the photon pulse shape.

## 2.3 Loading a $\Lambda$-level atom

In order to realize quantum memories with long lifetimes, one should store the quantum information in atomic states that have low energy levels as well as low decay rates, e.g., the $5\,^2S_{1/2}$ levels of the rubidium atom shown in Fig. 1-2. However, selection rules forbid any direct optical transition between two such levels, and therefore, the two-level ground-excited atomic system that we studied in the previous section is not a viable solution for quantum storage. In order to drive a transition between two metastable levels, we need a three-level atomic system. This forms a $\Lambda$-level atom as shown in Fig. 2-6. To induce the desired transition between $|g\rangle$ and $|e\rangle$ in this figure, one may think of first driving the atom from $|g\rangle$ to $|r\rangle$ by an optical beam on-resonance with the cavity, and then, driving it back to $|e\rangle$ by another optical source, e.g., a $z$-polarized beam as explained in the caption of Fig. 1-2. This two-step process can be performed without populating the third level by introducing detunings in both transitions, resulting in what is called an off-resonant Raman transition (ORT). In this section we study the ORT in the context of a $\Lambda$-level quantum memory being driven by a *single photon*. Our principal contributions in this section are introducing a non-adiabatic approach to ORT, evaluating its performance, and comparing it to two known adiabatic mechanisms.

Figure 2-6 shows a trapped $\Lambda$-level atom and its corresponding driving beams. Here, we assume that an external single-photon beam, in the initial state given by (2.1), is spatially matched to a mode of cavity with annihilation operator $\hat{b}$ and resonance frequency $\omega_0$. This cavity mode drives the $|g\rangle$-to-$|r\rangle$ transition with coupling rate $g_c$. There may exist a detuning $\Delta_1 \equiv \omega_0 - \omega_{gr}$ in this transition, where $\omega_{ij}$ denotes the transition frequency between levels $|i\rangle$ and $|j\rangle$, for $i, j \in \{g, r, e\}$. The second beam is assumed to be a $z$-polarized classical plane wave with frequency $\omega_z$ and a possibly time-dependent phase $\phi_z(t)$. The field's amplitude is under our control and may vary with time, and it determines the Rabi frequency $\Omega(t)$ that couples $|r\rangle$ and $|e\rangle$ via the following Hamiltonian, which is obtained under the rotating-wave

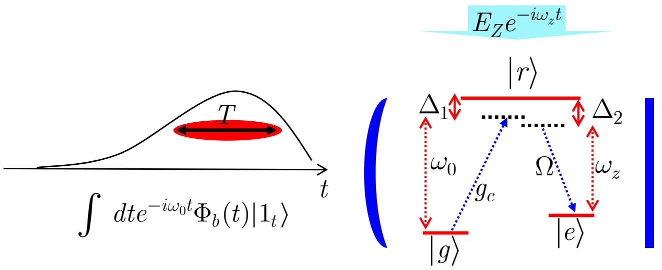

Figure 2-6: A $\Lambda$-level trapped atom illuminated by a single photon. The cavity mode corresponding to the single photon drives the atom from its ground state $|g\rangle$ to the auxiliary state $|r\rangle$. A $z$-polarized beam then shelves the atom in the metastable level $|e\rangle$. Here, $g_c$ is the Rabi frequency associated with a single photon, which is proportional to $E_{photon} \equiv \sqrt{\hbar\omega_0/(2\epsilon_0 V)}$, where $V$ is the cavity mode volume. $\Omega$ is the Rabi frequency associated with the control beam and is proportional to $|E_Z|$. These transitions are off-resonant by detunings $\Delta_1$ and $\Delta_2$, respectively, as defined in the text. The control field may also include a time-varying phase $\phi_z(t)$.

approximation [24]:

$$\hat{H}_R = \hat{H}_{cc} + \hbar\omega_{gr}\hat{\sigma}_{rr} + \hbar\omega_{ge}\hat{\sigma}_{ee} + \hbar g(\hat{\sigma}_{gr} + \hat{\sigma}_{rg}) + \hbar\Omega(t)(e^{-i[\omega_z t+\phi_z(t)]}\hat{\sigma}_{re} + e^{i[\omega_z t+\phi_z(t)]}\hat{\sigma}_{er}), \tag{2.34}$$

where $\Omega(t)$ and $\phi_z(t)$ are assumed to be real. The $|r\rangle$-to-$|e\rangle$ transition may also be off-resonant, by a detuning $\Delta_2 \equiv \omega_z - \omega_{er}$. Similar to the previous sections, with no initial excitation in the cavity and assuming that the atom is initially in the ground state $|g\rangle$, we can write down the most general state of the system as a function of time as follows

$$|\psi(t)\rangle = \int d\omega\alpha_\omega(t)|1_\omega\rangle|0\rangle_b|g\rangle + e^{-i\omega_0 t}\beta(t)|G\rangle + e^{-i\omega_0 t}c_r(t)|R\rangle + e^{-i(\omega_0-\omega_z)t+i\phi_z(t)}c_e(t)|E\rangle, \tag{2.35}$$

where

$$\begin{aligned}
|G\rangle &\equiv |\mathbf{0}\rangle_R|1\rangle_b|g\rangle, \\
|R\rangle &\equiv |\mathbf{0}\rangle_R|0\rangle_b|r\rangle, \\
|E\rangle &\equiv |\mathbf{0}\rangle_R|0\rangle_b|e\rangle.
\end{aligned} \tag{2.36}$$

Applying the Schrödinger equation to (2.35), we get

$$\begin{aligned}
\dot{\beta}(t) &= -ig_c c_r(t) - i\sqrt{2\kappa}\Phi_b(t) - \kappa\beta(t) \\
\dot{c}_r(t) &= -ig_c\beta(t) + i\Delta_1 c_r(t) - i\Omega(t)c_e(t) - \gamma_r c_r(t) \\
\dot{c}_e(t) &= -i\Omega(t)c_r(t) - i(\Delta_2 - \Delta_1 + \dot{\phi}_z(t))c_e(t),
\end{aligned} \tag{2.37}$$

where we used (2.7) in the first equation and included a non-cavity decay rate $\gamma_r$ for the upper state. We assume that the corresponding decay rate to the state $|e\rangle$ is negligible for the purpose of loading; it comes into play when we need to determine the storage time of the quantum memory. The above equations are not analytically tractable for arbitrary $\Omega(t)$ and $\phi_z(t)$. However, for our loading problem, we are looking for particular pulse shapes for $\Omega(t)$ and $\phi_z(t)$ that help the $|g\rangle$-to-$|e\rangle$ transition occur with high probability. In this section, we consider two of these loading mechanisms and provide approximate analytical solutions in each case. The first approach is based on known adiabatic transfer techniques [42, 36, 26, 28], and the second one is based on the simple idea that we came up with in the last section, i.e., turning off the coupling between $|g\rangle$ and $|e\rangle$ when the loading probability is maximum. We conclude this analysis by comparing the loading probabilities for these two methods as functions of $g_c/\kappa$ and $\kappa T$, and we examine their sensitivity to timing offsets.

### 2.3.1 Adiabatic loading of a Λ-level atom

It is a consequence of the Schrödinger equation that a system with a time-independent Hamiltonian—initially in one of its eigenstates—does not evolve with time. This is not necessarily the case for a time-dependent Hamiltonian, such as the one in (2.34), because the eigenstates, themselves, are functions of time, i.e., at each time $t$ there exists a set of eigenstates $\{|\psi_i(t)\rangle\}$. Suppose that, at $t = 0$, we start with the system in the eigenstate $|\psi_1(0)\rangle$. Then, for a sufficiently slowly-varying Hamiltonian, we expect to be in the eigenstate $|\psi_1(t)\rangle$ at time $t$, provided that $t$ is less than the time scale on which the Hamiltonian changes[8]. This is the main idea behind adiabatic passage. To employ this idea in our loading problem, we need to begin in a system eigenstate that resembles $|G\rangle$, and then, by changing $\Omega$, gradually transform this eigenstate into one that resembles our desired final

---

[8] Here, we have assumed that we have labeled the eigenstates at time $t$ in accordance with the same labeling at time $t - \delta t$. That should be doable if the Hamiltonian, and, consequently, its eigenvalues change continuously with time.

state, $|E\rangle$. To find such an eigenstate, let's have a look at the effective Hamiltonian that (2.37) suggests for the intracavity system:

$$\begin{aligned} \hat{H}_{\text{eff}} &= -\hbar\Delta_1|R\rangle\langle R| - \hbar(\Delta_1 - \Delta_2 - \dot{\phi}_z(t))|E\rangle\langle E| \\ &\quad +\hbar g_c(|R\rangle\langle G| + |G\rangle\langle R|) + \hbar\Omega(t)(|R\rangle\langle E| + |E\rangle\langle R|). \end{aligned} \tag{2.38}$$

Under the two-photon resonance condition, $\Delta_1 = \Delta_2$, and assuming that $\phi_z(t) = 0$, the above Hamiltonian can be written as follows

$$\hat{H}_{\text{eff}} = -\hbar\Delta_1|R\rangle\langle R| + \hbar\Omega_0(|R\rangle\langle B| + |B\rangle\langle R|), \tag{2.39}$$

where

$$|B\rangle = \sin\theta(t)|G\rangle + \cos\theta(t)|E\rangle \tag{2.40}$$

is called the *Bright* state, and we have $\cos\theta(t) \equiv \Omega(t)/\Omega_0$, $\sin\theta(t) \equiv g_c/\Omega_0$, and $\Omega_0 \equiv \sqrt{\Omega^2(t) + g_c^2}$. It can be seen that we have reduced the number of orthogonal states in the Hamiltonian by one. The missing state, orthogonal to both $|B\rangle$ and $|R\rangle$, is called the *Dark* state (because it does not interact with the upper state $|R\rangle$) and is given by

$$|D\rangle = -\cos\theta(t)|G\rangle + \sin\theta(t)|E\rangle. \tag{2.41}$$

The dark state is a zero-eigenvalue eigenstate of $\hat{H}_{\text{eff}}$, and it has the nice property that we are indeed looking for: for $\Omega(t) \gg g_c$, $|D\rangle \approx -|G\rangle$, but for $\Omega(t) \ll g_c$, $|D\rangle \approx |E\rangle$. This implies that if we start with a high value of $\Omega$ when the photon arrives, and then, slowly, reduce $\Omega$ to zero, we can adiabatically transfer the system from $|G\rangle$ to $|E\rangle$. The timing is of crucial importance, because if we turn off the pump either before or long after the photon arrives we lose the chance of absorbing the photon. There is also a slight chance of jumping into states that are orthogonal to $|D\rangle$, i.e., $|E\rangle$ or $|B\rangle$, in which case, the loading process has failed completely.

To study the loading problem in the new dark-bright state picture, it is convenient to change our basis from $\{|G\rangle, |E\rangle\}$ to $\{|B\rangle, |D\rangle\}$. We can then rewrite $\beta(t)|G\rangle + c_e(t)|E\rangle$ in the new form $B(t)|B\rangle + D(t)|D\rangle$, where

$$\begin{aligned} D(t) &= -\cos\theta(t)\beta(t) + \sin\theta(t)c_e(t), \\ B(t) &= \sin\theta(t)\beta(t) + \cos\theta(t)c_e(t). \end{aligned} \tag{2.42}$$

In terms of our new variables, and assuming $\Delta_1 = \Delta_2 + \dot{\phi}_z(t)$, (2.37) becomes

$$\begin{aligned} \dot{B}(t) &= -\dot{\theta}(t)D(t) - i\Omega_0(t)c_r(t) - i\sqrt{2\kappa}\sin\theta(t)\Phi_b(t) \\ &\quad -\kappa\sin^2\theta(t)B(t) + \kappa\sin\theta(t)\cos\theta(t)D(t) \\ \dot{D}(t) &= \dot{\theta}(t)B(t) - i\sqrt{2\kappa\cos^2\theta(t)}\Phi_b(t) - \kappa\cos^2\theta(t)D(t) + \kappa\cos\theta(t)\sin\theta(t)B(t) \\ \dot{c}_r(t) &= -i\Omega_0(t)B(t) - (\gamma_r - i\Delta_1)c_r(t). \end{aligned} \tag{2.43}$$

Now, it is the right time to apply our dark-state approximation, by which we assume that during the loading process there will be no quantum jumps to the bright state $|B\rangle$, i.e., $B(t) = 0$ . This will automatically forces $c_r(t)$ and $\dot{c}_r(t)$ to zero, i.e., there will be no quantum jumps to the auxiliary state $|R\rangle$ either. With this approximation, the above equations yield the following result for the dark-state evolution

$$\dot{D}(t) = -i\sqrt{2\kappa\cos^2\theta(t)}\Phi_b(t) - \kappa\cos^2\theta(t)D(t). \tag{2.44}$$

This equation resembles (2.7) for the cold-cavity case (after transforming $\beta(t)$ to $e^{i\omega_0 t}\beta(t)$ ). Therefore, the dark-state approximation has reduced our three-level problem to an equivalent cold-cavity problem whose cavity decay rate is $\kappa\cos^2\theta(t)$; see Fig. 2-7. In the cold-cavity case, we found the loading probability in the general case of time-dependent cavity decay rate, which thus applies to our current problem. Using (2.9), the loading probability for the $\Lambda$-level atom is given by

$$P_{loading}(t) = \left| \int_0^t d\tau \sqrt{2\kappa}\cos\theta(\tau)e^{-K(t)+K(\tau)}\Phi_b(\tau) \right|^2, \tag{2.45}$$

where $K(t) = \kappa\int_0^t d\tau\cos^2\theta(\tau)$.

To maximize the loading probability, we need to find an optimum assignment for $\cos\theta(t)$ that not only maximizes the loading probability, but also satisfies our adiabatic conditions. In order to achieve a maximum transfer of free-field photons into the cavity mode, we need

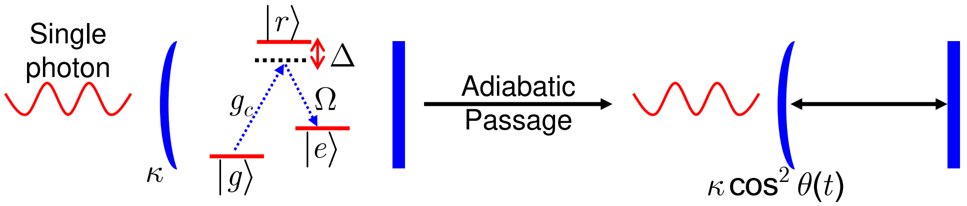

Figure 2-7: The loading problem for a $\Lambda$-level atom driven—on the two-photon resonance—by a single photon and a classical control field is adiabatically equivalent to the cold-cavity loading problem. The cavity decay rate is a function of time, and is determined by the control field.

to minimize the outgoing field components by destructively interfering the directly reflected and the circulating fields. Fleischhauer et al. have shown that a necessary condition for destructive interference is [28]:

$$-\frac{d}{dt}\ln\cos\theta(t)+\frac{d}{dt}\ln\Phi_b(t)=\kappa\cos^2\theta(t). \tag{2.46}$$

For our particular example of a secant hyperbolic pulse shape $\Phi_b(t)=\sqrt{2/T}\mathrm{sech}(4t/T)$, it turns out that [28]

$$\cos\theta(t)=\sqrt{2/(\kappa T)}\frac{\mathrm{sech}(4t/T)}{\sqrt{1+\tanh(4t/T)}} \tag{2.47}$$

and

$$\Omega(t)=\frac{g_c\mathrm{sech}(4t/T)}{\sqrt{[1+\tanh(4t/T)][\tanh(4t/T)+\kappa T/2-1]}}. \tag{2.48}$$

In order that the above relation for $\Omega(t)$ provides us with a positive real Rabi frequency, we must satisfy the condition $\kappa T\geq 4$. This, on the other hand, implies that for a successful adiabatic transfer, our input pulse must be long enough so that we can slowly change the quantum memory state.

Employing (2.48) in (2.45), it can be shown that $|D(t)|^2=[1+\tanh(4t/T)]/2$, which approaches one as $t\rightarrow\infty$. This result does not give us any information, however, about the required values for $\kappa T$ and $g_c/\kappa$. In fact, because $\cos\theta(t)$, as given by (2.47), is only a function of $\kappa T$, our equivalent cold-cavity model does not have any dependence on $g_c$. This is a consequence of the dark-state approximation that we used to eliminate the bright state. In order to reveal the dependence of the loading probability on the coupling rate, and also to obtain more accurate results, we must return to the original differential equations in (2.37) or (2.43), and try to solve them numerically. In order to simplify this numerical analysis, we first adiabatically eliminate the upper state $|R\rangle$ by assuming that $\dot{c}_r(t) = 0$. This is a reasonable assumption provided that we have large enough detunings, i.e., $\Delta_1, \Delta_2 \gg \Omega, g_c$, and it provides us with more accurate results than can be obtained under the dark-state condition $B(t) = c_r(t) = 0$. As a result of the adiabatic-elimination condition, $\dot{c}_r(t) = 0$, we obtain

$$c_r(t) = \frac{g_c}{i\gamma_r'}\beta(t) + \frac{\Omega(t)}{i\gamma_r'}c_e(t) \tag{2.49}$$

where we used (2.37) and $\gamma_r' = \gamma_r - i\Delta_1$. For large enough detuning, i.e., for $\Delta_1 \gg \gamma_r$, we can replace $i\gamma_r'$ with $\Delta_1$. Plugging the above equation into the rest of (2.37), we then obtain

$$\begin{aligned}\dot{\beta}(t) &= -i(g_c^2/\Delta_1)\beta(t) - igc_e(t) - i\sqrt{2\kappa}\Phi_b(t) - \kappa\beta(t),\\ \dot{c}_e(t) &= -ig\beta(t) - i(\Omega^2/\Delta_1)c_e(t) - i(\Delta_2 - \Delta_1 + \dot{\phi}_z(t))c_e(t),\end{aligned} \tag{2.50}$$

where $g = g_c\Omega/\Delta_1$ is the effective coupling rate between $|g\rangle$ and $|e\rangle$. The above equations resemble the equations in (2.22), and therefore, they model the evolution of a two-level system, with coupling rate $g$ and detuning $\Delta = [g_c^2 - \Omega^2(t)]/\Delta_1 + \Delta_1 - \Delta_2 - \dot{\phi}_z(t)$, driven by a single photon[9]. In the above equations, the effective coupling rate and detuning are both generally functions of time. At the end of this section, we will investigate the performance of adiabatic loading mechanisms by numerically solving the equations in (2.50).

### 2.3.2 Non-adiabatic loading of a $\Lambda$-level atom

The adiabatic-passage approach presented in the previous section is an elegant way to handle atomic quantum memories. It, however, requires the input pulse shape to be several times longer than the cavity decay time, $1/\kappa$ [28]. We also need to use the appropriate pulse shaping for the control field in accord with the input pulse shape. Here, we propose a simpler approach for loading a $\Lambda$-level atom, which does not impose any restrictions on the input pulse shape and does not need any adiabatic pulse shaping for the control field. As was mentioned for adiabatic passage, however, this non-adiabatic approach to loading is also sensitive to the photon arrival time. Our method is based on what we observed in Section 2.2 for a two-level atom with a constant coupling rate $g$. There, we realized that a maximum loading probability of greater than 90% was achievable provided that we could turn off the

---

[9] Note that the new baseband pulse shape is given by $e^{ig_c^2 t/\Delta_1}\Phi_b(t)$. We will denote this new function by $\Phi_b(t)$ again for convenience.

Figure 2-8: The loading problem for a $\Lambda$-level atom driven by a single photon and a constant classical control beam is equivalent to the two-level hot-cavity loading problem. The new coupling rate $g$ is equal to $g_c\Omega/\Delta_1$ and the detuning $\Delta$ (the difference between the optical frequency and the atomic transition frequency) is $\Delta_1 - \Delta_2 + (g_c^2 - \Omega^2)/\Delta_1$.

atom-light coupling at $t = T_{Load}$. Here, we show that this is indeed possible to do for a $\Lambda$-level atom, by turning off the control field, which has a constant value otherwise, at the right time. The mathematical analogy between loading a $\Lambda$-level atom and a two-level atom both driven by single photons was shown in (2.50). Figure 2-8 illustrates this equivalence. In the non-adiabatic case, where $\Omega$ is time independent and $\phi_z(t) = 0$, the effective coupling rate, $g = g_c\Omega/\Delta_1$, is proportional to the control field's amplitude. By turning off the control field at $t = T_{Load}$, or, effectively, by imposing $\Omega(t) = 0$ for $t > T_{Load}$, the coupling rate $g$ vanishes for $t > T_{Load}$. Hence, if we are in the state $|e\rangle$ at $t = T_{Load}$, we will stay there until a decay process returns the atom to its ground state. The loading probability is then given by $|c_e(T_{Load})|^2$ as obtained in (2.27). The effective detuning, $\Delta = (g_c^2 - \Omega^2)/\Delta_1 + \Delta_1 - \Delta_2$, can be forced to zero, by properly choosing $\Delta_1$ and $\Delta_2$, thus compensating for the induced Stark shift and enabling us to obtain a higher loading probability.

It is worth mentioning that the only condition that we need to satisfy for our adiabatic elimination is $\Delta_1, \Delta_2 \gg \Omega, g_c$. This condition ensures that we never populate the upper state. However, it is possible to go to the bright state, because, in the non-adiabatic case, our control pulse shape is not matched to the input pulse shape.

### 2.3.3 Adiabatic versus non-adiabatic loading: numerical comparison

In this section, we compare our proposed non-adiabatic approach to loading a quantum memory with those methods that use adiabatic-transfer techniques. Because of the equivalence of the non-adiabatic loading of a $\Lambda$-level atom to the two-level atom problem that we studied in Section 2.2, all the numerical results that we obtained in Section 2.2.2 are applicable to the current non-adiabatic case provided that we employ the effective coupling rate and detuning in our calculations. The adiabatic-transfer technique that we described in Section 2.3.1 is a well-studied problem in the literature. To make our comparison more concrete, in this section, we will consider two particular examples of adiabatic loading, which have been proposed in [26] and [28]. In [26], the authors have devised a method for transferring the state of a trapped-atom quantum memory to another trapped-atom quantum memory. Their approach is based on adiabatically transferring the state of one memory to a single photon, which will then propagate and load the other memory with the desired state. Their loading process is facilitated by forcing the photon's pulse shape to be symmetric, so that, at the receiver end, we can employ the time-reverse of the control pulse shape that was used at the transmitter. The desired pulse shape for the control field under the dark-state condition at zero effective detuning can be found numerically by solving the corresponding Schrödinger equations. However, the approach from [26] is not suitable for an incoming photon with an arbitrary pulse shape. In [28], the authors have employed the adiabatic-transfer technique to load an atomic ensemble with the state of a single photon. Their approach can be easily extended to the single-atom case, and that is what we did in Section 2.3.1. They have employed the dark-state approximation under the two-photon resonance condition with a constant-phase control field. Their approach sets certain limitations on the length of the input pulse shape. In fact, in order to fulfill the dark-state condition, the input pulse shape must be longer than a threshold value. As compared to these two adiabatic mechanisms, our non-adiabatic approach puts no constraints on the input pulse shape.

Several issues make our work in this chapter, and the numerical results presented in this section, distinct from the previous works reported in the literature. The first issue is our accounting for a nonzero probability for populating the bright state. This probability is neglected in all the methods that use the dark-state approximation, e.g, [26] and [28]. We will see in this section how the nonzero probability of being in the bright state affects the loading performance. That also makes it possible to scrutinize the dependence of the loading probability, in both adiabatic and non-adiabatic mechanisms, on the key system parameters, e.g., $g_c/\kappa$ and $\kappa T$. This evaluation is one of the original contributions of this thesis.

As mentioned before, it is of practical importance to know at what values of input bandwidth, represented by $\kappa T$, and atomic coupling rate, represented by $g_c/\kappa$, a desired system performance can be achieved. For our non-adiabatic approach, at $\Delta = 0$—which can be achieved by setting $\Delta_2 = (g_c^2 - \Omega^2)/\Delta_1 + \Delta_1$—system performance is governed by the

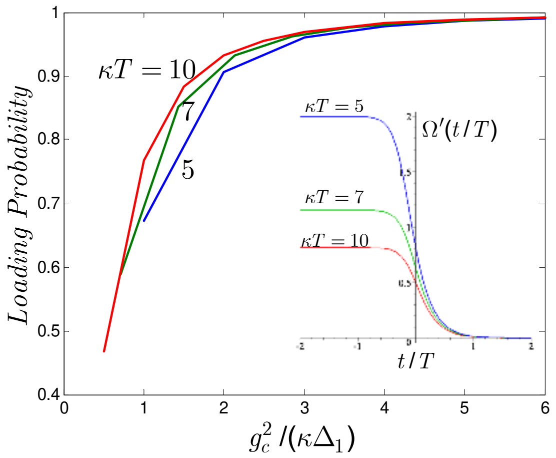

Figure 2-9: The loading probability for the adiabatic method for different values of $\kappa T$ versus $g_c^2/(\kappa\Delta_1)$, at the two-photon resonance $\Delta_1 = \Delta_2$ and for $\phi_z(t) = 0$. These graphs are obtained by numerically solving (2.50) for the control pulse shapes given in the inset corresponding to a secant hyperbolic input pulse shape.

effective coupling rate $g = g_c\Omega/\Delta_1$, as shown in Fig. 2-4. The optimum value of $g/\kappa$ can then be obtained by making appropriate choices for $g_c$, $\Omega$, and $\Delta_1$. The only conditions that we need to satisfy are $\Delta_1 \gg \gamma_r$ and $g_c, \Omega \ll \Delta_1$. That leaves us some room to pick a smaller value for $g_c$, which determines the cavity length, and larger values for $\Omega$, which is classically applied. This is not the case for the adiabatic approach proposed in [28]. For instance, for the secant hyperbolic pulse shape, using the optimum control pulse shape given by (2.48), we have $g_c\Omega(t) = g_c^2\Omega'(t)$, where $\Omega'(t)$ is only a function of $\kappa T$ and not $g_c$. Therefore, for a fixed value of $\kappa T$, the only way to increase the coupling rate is to use a shorter cavity, which yields a larger $g_c$.

In this section, we consider two approaches to specifying the effective detuning in the adiabatic case. The first case, employed in [28], is for the two-photon-resonance condition for which $\Delta_1 = \Delta_2$ and $\phi_z(t) = 0$. The second, used in [26], is for the zero-effective-detuning case, which can be achieved by setting $\dot{\phi}_z(t) = \Delta_1 - \Delta_2 + [g_c^2 - \Omega^2(t)]/\Delta_1$.

It is interesting to find the dependence of the loading probability, for the adiabatic scheme proposed in [28], on the coupling rate $g_c$. For this purpose, we have numerically solved the Schrödinger equations in (2.50), for $\Omega(t)$ given by (2.48) at the two-photon resonance $\Delta_1 = \Delta_2$ and for $\phi_z(t) = 0$. In Fig. 2-9 we have plotted $|c_e(5T)|^2$ versus an effective coupling rate $g' \equiv g_c^2/\Delta_1$. Choosing $t = 5T$ ensures that the loading process has ended, and therefore $|c_e(5T)|^2$ is effectively the loading probability. This figure shows that for the two-photon

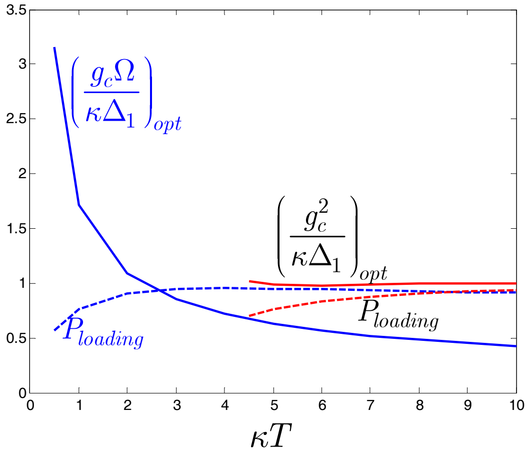

Figure 2-10: The optimum coupling rate and the maximum loading probability achieved at this rate for both adiabatic and non-adiabatic approaches. (Non-adiabatic graphs start from $\kappa T = 0.5$; Adiabatic graphs start from $\kappa T = 4.5$.) For all graphs, we assume that $\dot{\phi}_z(t) = \Delta_1 - \Delta_2 + [g_c^2 - \Omega^2(t)]/\Delta_1$. A secant hyperbolic pulse shape has been used for the incoming photon.

resonance case, higher $g_c$ values yield higher loading probabilities. The effective coupling rate $g'$ that we need is about $2\kappa$ for 90% loading probability at $\kappa T = 5$. It can be seen that there is an advantage for pulses with higher values of $\kappa T$. This is because our adiabatic scheme is more efficient for longer input pulses.

We can also solve the Schrödinger equations in (2.50), for $\Omega(t)$ given by (2.48), at zero effective detuning as proposed in [26][10], i.e., when $\dot{\phi}_z(t) = \Delta_1 - \Delta_2 + [g_c^2 - \Omega^2(t)]/\Delta_1$. In this case, in analogy to the non-adiabatic case, we observe the existence of an optimum value for $g'/\kappa$. Figure 2-10 shows the optimum coupling rates and the maximum loading probabilities achieved at these rates for the adiabatic and non-adiabatic approaches. Here, $(g'/\kappa)_{opt}$ is almost constant, and close to unity, for all values of $\kappa T$, whereas $(g/\kappa)_{opt}$ goes down gradually to zero as we increase $\kappa T$. Again, we note that the non-adiabatic approach has no constraint on the input pulse width, which allows a larger class of single-photon sources to be used in quantum communication systems. The maximum loading probability that can be achieved by the adiabatic approach asymptotically goes to one; this is not the case for the non-adiabatic approach, however.

---

[10] The control field's Rabi frequency given by (2.48) has been obtained under the two-photon resonance and dark-state conditions, and it is not therefore the optimum pulse shape for the zero-effective-detuning case. It can however be verified numerically that this pulse shaping for the control field provides us with a close-to-optimum performance. This is in accord with the results reported in [28] implying that the loading probability will only be slightly affected by small deviations from the optimum control field pulse shape.

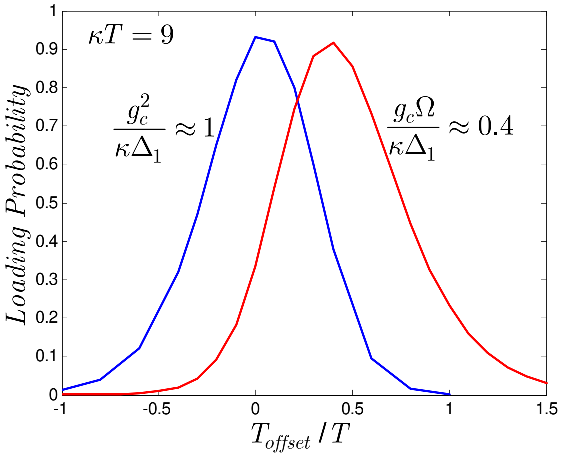

Figure 2-11: Loading probability versus normalized timing offset in the photon arrival. In the adiabatic case (the graph on the left), this timing error results in applying the control field earlier or later than the correct time. In the non-adiabatic case, it results in stopping the control field earlier or later than $T_{Load}$. Both graphs have been obtained at $\dot{\phi}_z(t) = \Delta_1 - \Delta_2 + [g_c^2 - \Omega^2(t)]/\Delta_1$ for their corresponding optimum coupling rates for secant hyperbolic input pulse shapes.

Finally, Fig. 2-11 shows the sensitivity of both schemes to timing offsets. Here, $T_{\text{offset}}$ refers to the time that we stop the control field in the non-adiabatic approach, and it represents a time shift in the adiabatic approach, i.e., using $\Omega(t - T_{\text{offset}})$ instead of $\Omega(t)$. Both cases may occur if we have an inaccurate estimate of the photon arrival time. This figure shows that both schemes have almost the same tolerance against timing offsets. A 50% loading probablity (3 dB loss) is achievable even if we are about $\pm T/2$ off from the correct loading time. Although not shown on the graph, the same result holds if we use the adiabatic approach under the two-photon-resonance condition.

## 2.4 Other single-excitation problems

The results we obtained in this section are directly applicable to several other problems. For instance, consider the double-$\Lambda$ atom in Fig. 2-12(a). Here, we are trying to load the memory with a single photon in an arbitrary polarization state as follows:

$$|\psi_0\rangle = \int d\omega \phi(\omega)(\alpha|1_\omega\rangle_{\sigma_+} + \beta|1_\omega\rangle_{\sigma_-}), \tag{2.51}$$

where $|\alpha|^2 + |\beta|^2 = 1$. Here, $|1_\omega\rangle_{\sigma_\pm}$ refers to a single-photon state at frequency $\omega$ in the $\sigma_\pm$ polarization. The goal of the loading process is to absorb this photon, by properly choosing

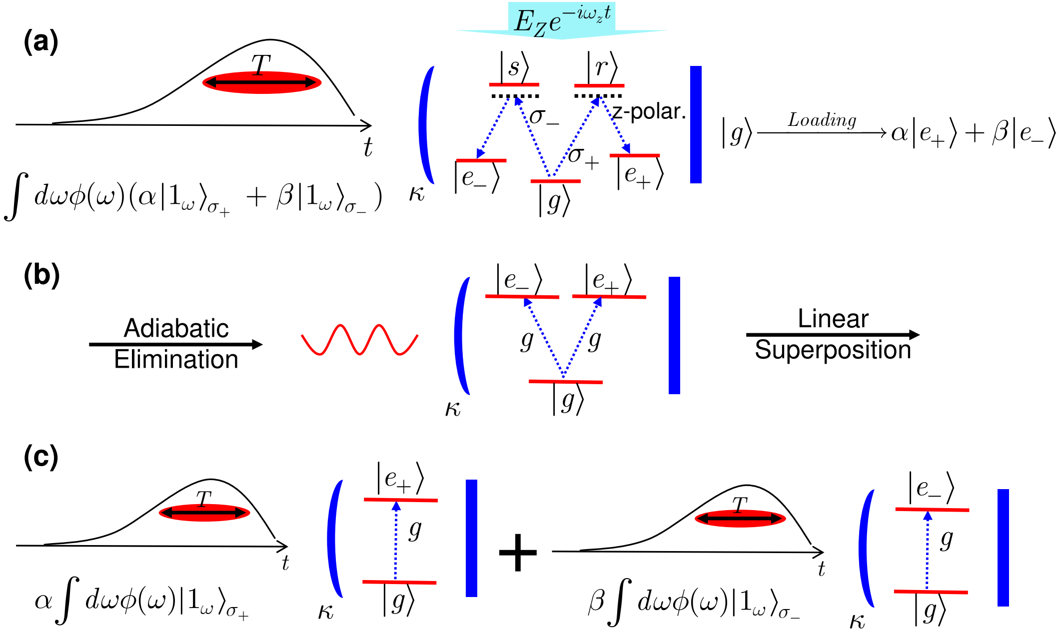

Figure 2-12: (a) Loading a double-$\Lambda$ atom driven by a polarization-state single photon. Along the lines of Fig. 2-8, this system is equivalent to the $V$-level system shown in (b). (c) Reduction of the $V$-level loading problem to two two-level loading problems by means of linear superposition.

$z$-polarized control fields, and store its polarization information in the metastable levels $|e_+\rangle$ and $|e_-\rangle$ corresponding to the $\sigma_+$ and $\sigma_-$ polarizations, respectively. The loading probability is therefore determined by the probability of ending up in $|e\rangle \equiv \alpha|e_+\rangle + \beta|e_-\rangle$. In order to calculate this probability, we can use the results of the previous subsection to reduce each $\Lambda$-configuration leg of the atom to an equivalent two-level system, as shown in Fig. 2-12(b). The resulting configuration is a $V$-level atom illuminated by a polarization-state single photon. This latter problem can be solved by again noting that the full Schrödinger equations—for the state of reservoirs, cavity modes, and the atom—that model the evolution of this system are in the linear form $\dot{\mathbf{X}} = -i\mathbf{A}\mathbf{X}$, where $\mathbf{X}$ is a column matrix representing all amplitude variables (such as $\alpha_\omega(t)$, $\beta(t)$, etc.), and $\mathbf{A}$ is a square matrix representing the mutual coupling rates between $|g\rangle$, $|e_\pm\rangle$, and $|1_\omega\rangle_{\sigma_\pm}$. These equations are linear in response to the superposition state in (2.51), and therefore, each leg of the $V$-level atom is only driven by the corresponding part in the initial state, as shown in Fig. 2-12(c). In fact, for $\alpha\int d\omega\phi(\omega)|1_\omega\rangle_{\sigma_+}$ as the input, the amplitude probability of being in the state $|e_-\rangle$, $c_-(t)$, will be zero. $c_-(t)$ is nonzero only for $\beta\int d\omega\phi(\omega)|1_\omega\rangle_{\sigma_-}$ as the input. In the latter case, the evolution of $c_-(t)$ is the same as that of a two-level system. For instance, if we are using the non-adiabatic loading mechanism, $c_-(t)$ is given by $\beta c_e(t)$, with $c_e(t)$ is given by (2.27). The same argument holds for $c_+(t)$, so that the overall probability of ending up in $|e\rangle$ is given by $(|\alpha|^2 + |\beta|^2)|c_e(t)|^2 = |c_e(t)|^2$. This proves the equivalence of loading a $V$-level atom to the loading of a two-level atom when both are driven by single photons. This result also extends to cases in which the two legs of the atomic system are nonlocal—e.g., when a pair of two-level trapped-atom memories driven by a photon-number entangled state; see Fig. A-2. Such a system is an example of the to-the-memory configuration for entanglement distribution and can be used in teleportation systems. In Appendix A, we prove the above equivalence using a change of basis in the Hamiltonian in conjunction with the HL equations.

# Chapter 3

# MIT-NU Hot-cavity Loading

With the results that we have developed for trapped-atom quantum memories in the previous chapter, we can home in on quantum communication systems that use this type of storage. Our focus on this chapter will be on the architecture proposed by a group of researchers from the Massachusetts Institute of Technology and Northwestern University (termed MIT-NU hereafter) [30] for quantum communication. The MIT-NU construct uses the to-the-memory configuration in Fig. 1-4 to distribute and share polarization entanglement between two rubidium atoms. Because the rubidium atoms can be treated as double-$\Lambda$ quantum memories (see Figs. 1-2 and 1-3), MIT-NU entanglement distribution is essentially a loading problem, in which we are interested in transferring an entangled state to two trapped atoms. All previous analyses of the MIT-NU architecture [43, 30, 44], however, have employed a cold-cavity approach in which each optical cavity—that would hold an $^{87}$Rb atom in the actual implementation—is regarded as empty, and the loading probability is calculated by determining the probability that the state of the intracavity photon fields at the end of a loading interval is the desired singlet state. In this chapter, we provide a hot-cavity loading analysis for the MIT-NU system. This is an extension of what we obtained for single atoms in the previous chapter, and we will use similar ideas and techniques here. As a general convention, we will continue to employ the notation and abbreviations that we used in Chapter 2. In what follows, we first describe the MIT-NU architecture in more detail and summarize its fidelity analysis. Then, we will describe the MIT-NU loading problem and study its corresponding adiabatic and non-adiabatic loading mechanisms. We conclude with some numerical results for the loading probability. This constitutes the first performance

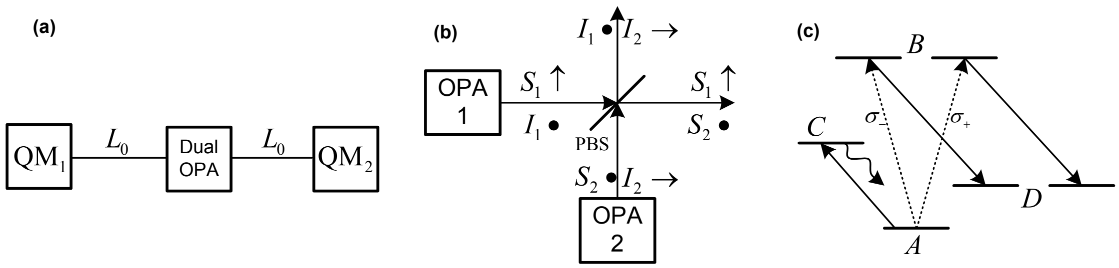

Figure 3-1: (a) MIT-NU architecture for long-distance quantum communications consisting of a dual-OPA source that produces polarization-entangled photons, and two quantum memories, $\mathrm{QM}_1$ and $\mathrm{QM}_2$, separated by $2L_0$ km. (b) Dual-OPA source of polarization-entangled photons. OPAs 1 and 2 are coherently-pumped ($\pi$-rad out of phase), continuous-wave, type-II phase matched, doubly-resonant amplifiers operated at frequency degeneracy whose orthogonally-polarized signal ($\{S_k\}$) and idler ($\{I_k\}$) outputs are combined, as shown, on the polarizing beam splitter (PBS). (c) Notional schematic for the relevant hyperfine levels of $^{87}$Rb. Each quantum memory consists of a single trapped rubidium atom that can absorb arbitrarily polarized photons, storing their coherence in the long-lived $D$ levels. A non-destructive load verification is effected by means of the $A$-to-$C$ cycling transition.

analysis for the MIT-NU architecture that includes the presence of atoms within the quantum memory units, and is a major new result from this thesis.

## 3.1 MIT-NU architecture

The MIT-NU architecture is a singlet-based system for qubit teleportation that uses a novel ultrabright source of polarization-entangled photon pairs [41], and trapped rubidium atom quantum memories [45] whose loading can be nondestructively verified [30, 44]. Figure 3-1(a) shows a schematic of this system: $\mathrm{QM}_1$ and $\mathrm{QM}_2$ are trapped rubidium atom quantum memories, each $L_0$ km away—in opposite directions—from a dual optical parametric amplifier (OPA) source. As the overall structure of this architecture and its preliminary performance analysis have been described in considerable detail elsewhere [43, 30, 44], in this section, we shall provide only a brief description sufficient to enable comparison with other schemes that will be addressed in the thesis. The results presented in this section are all based on the cold-cavity approach to modeling quantum memories.

Each optical parametric amplifier in the dual-OPA source is a continuous-wave, type-II phase matched, doubly-resonant amplifier operating at frequency degeneracy $\omega_S = \omega_I$. Its signal ($S$) and idler ($I$) outputs comprise a stream of orthogonally-polarized photon pairs that are in a joint Gaussian state [30]. By coherently pumping two of these OPAs, $\pi$-rad out of phase, and combining their outputs on a polarizing beam splitter, as shown in Fig. 3-1(b), we obtain signal and idler beams that are polarization entangled [41]. These beams are routed down separate optical fibers to the trapped-atom quantum memories.

A schematic of the relevant hyperfine levels of $^{87}$Rb is shown in Fig. 3-1(c). The memory atoms are initially in the ground state $A$. From this state they can absorb a photon in an arbitrary polarization transferring that photon's coherence to the $B$ levels. By means of a Raman transition, this coherence is shelved in the long-lived $D$ levels for subsequent use. However, because propagation and fixed losses may destroy photons before they can be stored, and because both memories must be loaded with a singlet state prior to performing qubit teleportation, the MIT-NU architecture employs a clocked loading protocol in which the absence of fluorescence on the $A$-to-$C$ cycling transition provides a non-destructive indication that a memory atom has absorbed a photon. If no fluorescence is seen from either the $\mathrm{QM}_1$ or $\mathrm{QM}_2$ atoms in a particular loading interval, then we assume that both memories have stored photon coherences and so are ready for the rest of the teleportation protocol, i.e., Bell-state measurement (BSM), classical communication of the result, and single-qubit rotation [45].

A variety of error sources associated with the MIT-NU entanglement-distribution scheme have been identified and their effects analyzed [44]. Some are due to imperfections in the dual-OPA source, e.g., pump-power imbalance or pump-phase offsets between the two OPAs. Others are due to the time-division multiplexed scheme—omitted from our brief description of the MIT-NU architecture—needed to compensate for the slowly-varying birefringence encountered in fiber propagation. The most fundamental error source, however, is the emission of more than one pair of polarization-entangled photons, in conjunction with propagation and fixed losses. Multiple-pair emissions may lead to loading events (both memory atoms have absorbed photons) that do *not* leave the memories in the desired singlet state. This error mechanism is the primary one we shall consider here, in this summary, although pump-phase offsets will also be included.

For a single trial of the MIT-NU loading protocol, let $P_{\text{herald}}$ denote the probability that both memories are loaded, and let $P_{\text{success}}$ denote the probability that these memories have loaded the desired singlet state. Then, the fidelity associated with the entanglement distribution can be defined as $F_E = P_{\text{success}}/P_{\text{herald}}$ . From the work of Yen and Shapiro

[44], we can obtain

$$P_{\text{success}} = \frac{N^2 + \tilde{n}^2[1+\cos(\theta_1-\theta_2)]}{[(1+\bar{n})^2-\tilde{n}^2]^4}, \tag{3.1}$$

and

$$F_E = \frac{N^2 + \tilde{n}^2[1+\cos(\theta_1-\theta_2)]}{4N^2+2\tilde{n}^2}, \tag{3.2}$$

where

$$N = \bar{n}(1+\bar{n}) - \tilde{n}^2, \quad \bar{n} = I_- - I_+, \quad \text{and} \quad \tilde{n} = I_- + I_+, \tag{3.3}$$

with

$$I_\pm = \frac{\eta_f \gamma\gamma_c}{\Gamma\Gamma_c}\frac{|G|}{(1\pm|G|)(1\pm|G|+\Gamma_c/\Gamma)}. \tag{3.4}$$

In these expressions: the $\{\theta_i\}$ are the pump-phase offsets for the two OPAs; $|G|^2$ is the normalized OPA pump gain ($|G|^2 = 1$ at oscillation threshold); $\Gamma$ and $\gamma$ are the OPA cavity's linewidth and its output coupling rate; $\Gamma_c$ and $\gamma_c$ are the memory cavity's linewidth and its input coupling rate; and $\eta_f$ is the transmissivity of the $L_0$-km-long source-to-memory fiber propagation path.

The processing stage of the MIT-NU teleportation protocol is done via optically off-resonant Raman transitions (ORTs) and sequential fluorescence detection; for details see [45]. The MIT-NU architecture is capable of performing a full BSM on the joint Alice-Charlie system. The latter two share an optical cavity to hold their respective trapped atoms. Via a series of ORT pulses the joint state of Alice and Charlie can be transferred to Alice's atom, and then, using a method of *sequential elimination*, she can perform a full BSM. By sending the measurement results to Bob, he can retrieve Charlie's state by using at most two additional ORTs [45]. The performance analysis in [44] assumes all these atomic transitions and measurements can be done free of error. In that circumstance, the teleportation fidelity, $F_T$, is as follows [44]

$$F_T = [2 - 2a + (1-4a)\cos(\theta_1-\theta_2)]/3\,, \tag{3.5}$$

where $a = N^2/(4N^2+2\tilde{n}^2)$. This teleportation fidelity measures how closely Bob's state—after the teleportation protocol is completed—will replicate Charlie's qubit. In particular, $F_T = \overline{{}_B\langle\psi|\hat{\rho}_B|\psi\rangle_B}$, where $|\psi\rangle_B$ is the Bob's desired final state, $\hat{\rho}_B$ is Bob's density operator at the end of the protocol, and the overbar denotes averaging uniformly over the Bloch

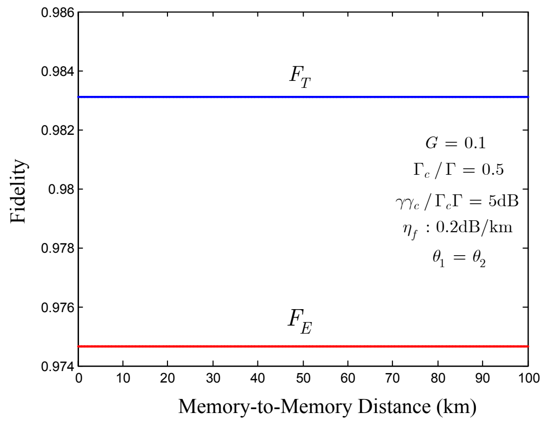

Figure 3-2: Entanglement and teleportation fidelities for the MIT-NU architecture versus distance $2L_0$ in km.

sphere.

Figure 3-2 shows the entanglement and teleportation fidelities for the MIT-NU architecture versus the total distance $2L_0$. It can be seen that under normal operating conditions, as given by the parameters shown on the figure, the MIT-NU system achieves a high fidelity both in teleportation and entanglement distribution, regardless of the distance separating Alice and Bob. Throughput, however, which is the number of entangled pairs per second that could be loaded if Alice and Bob each possessed lattices of trapped atoms, is not independent of the distance that separates Alice and Bob [44]. We note from Fig. 3-2, that $F_T$ is a little bit higher than $F_E$. This is because even when we have not loaded the cavities with the singlet state, there is still a nonzero chance of getting the right state back at the end of the teleportation protocol.

## 3.2 MIT-NU loading problem

The cold-cavity approach used in the previous section might suffice for determining the deteriorating effect of multiple-pair emission. It, however, cannot help us determine the actual atomic and optical parameters that we must employ to successfully load the memories. As we realized in the previous chapter, two of these parameters are of practical importance: source bandwidth and atom-light coupling rate, where the former affects the system throughput while the latter determines the cavity length. This section is devoted to finding analytical results for the MIT-NU loading probability when we consider a double-$\Lambda$-level atom in each memory. To this end, we make several simplifying assumptions. First, we replace the OPA devices in the entanglement source with simple spontaneous parametric downconverters (SPDCs). This is actually how most realizations of this system work [19, 20], and, except for their flux and their output bandwidths, SPDC systems have the same physical characteristics as OPA sources. The second assumption is the *biphoton* approximation to the SPDC output. The latter is mostly a vacuum state, plus a small biphoton component, and a much smaller multi-pair contribution [30]. The vacuum term can be easily recognized by our non-destructive loading verification technique, and can therefore be ignored. The multi-pair case is of minor concern in the context of loading, because its degrading effect has been accounted for in the previous analyses. So, in this section, we only consider the case in which the type-II phase-matched SPDC output, operating at frequency degeneracy, is a biphoton state in the following general form [46]

$$|\psi\rangle = \int d\omega_S \int d\omega_I \phi(\omega_S, \omega_I) |1_{\omega_S}\rangle_{S,\diamond} |1_{\omega_I}\rangle_{I,\bar{\diamond}}, \tag{3.6}$$

where $\int d\omega_S \int d\omega_I |\phi(\omega_S, \omega_I)|^2 = 1$, and $\diamond$ and $\bar{\diamond}$ represent two orthogonal polarizations. For the particular configuration in Fig. 3-1(b), the desired output state will then be

$$\begin{aligned} |\psi_{out}\rangle &= \frac{1}{\sqrt{2}} \int d\omega_S \int d\omega_I \phi(\omega_S, \omega_I) [|1_{\omega_S}\rangle_{S,\uparrow} |1_{\omega_I}\rangle_{I,\bullet} - |1_{\omega_S}\rangle_{S,\bullet} |1_{\omega_I}\rangle_{I,\uparrow}] \\ &= \frac{1}{\sqrt{2}} \int d\omega_S \int d\omega_I \phi(\omega_S, \omega_I) [|1_{\omega_S}\rangle_{S,\sigma_+} |1_{\omega_I}\rangle_{I,\sigma_-} - |1_{\omega_S}\rangle_{S,\sigma_-} |1_{\omega_I}\rangle_{I,\sigma_+}], \end{aligned} \tag{3.7}$$

where the last equality is due to the invariance of the singlet state with respect to the polarization basis. Finally, we assume that there is no loss and no delay in the channel, and therefore, the above state is the input state to the quantum memories.

Figure 3-3(a) shows a schematic of the MIT-NU loading problem with the above considerations taken into account. Here, similar to the previous chapter, we assume that the signal and idler photons are spatially matched to one of the cavity's spatial modes. Their center frequency, $\omega_0$, is also matched to the resonance frequency of this cavity mode. Depending on their polarizations, they can drive one of the transitions $|g\rangle \longrightarrow |s\rangle$ (for $\sigma_+$-polarization) and $|g\rangle \longrightarrow |r\rangle$ (for $\sigma_-$-polarization) with time-independent coupling rate $g_c$ and detuning $\Delta_1$. The second transition is facilitated by a $z$-polarized classical field, which induces a Rabi frequency $\Omega$ with detuning $\Delta_2$. The goal of memory loading is to absorb the entangled photons and store their coherence in the metastable levels of each memory, i.e., to end up in

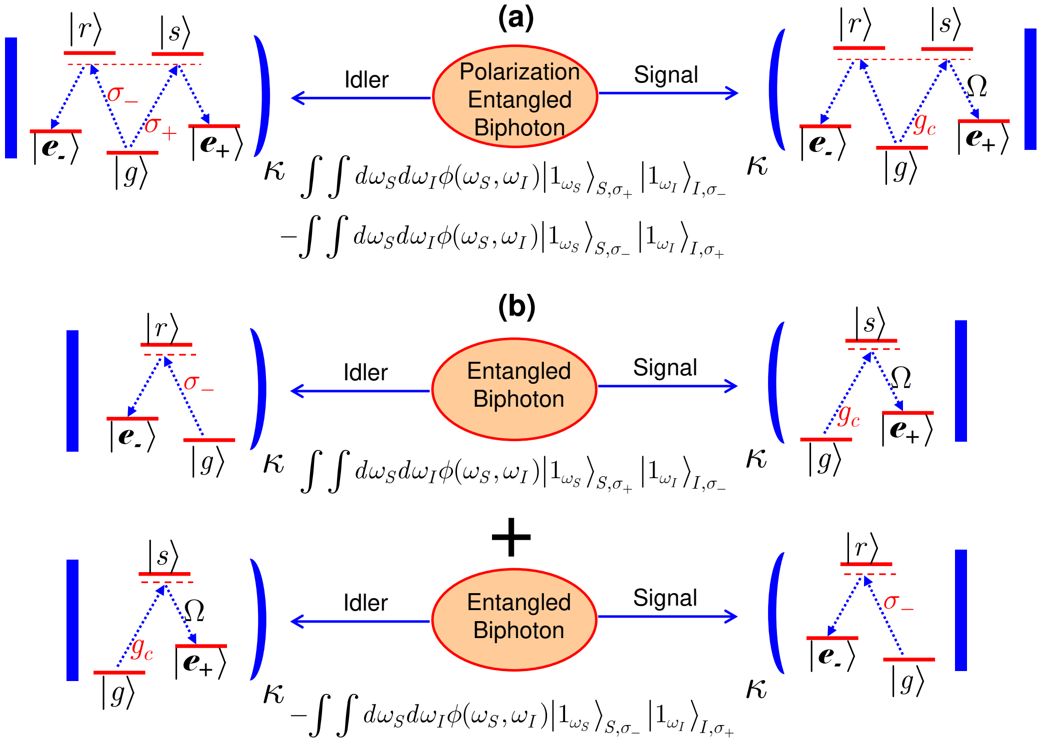

Figure 3-3: (a) Loading a pair of double-$\Lambda$ atoms illuminated by a polarization-entangled biphoton. This is a fair approximation to the MIT-NU loading problem. (b) Breaking the loading problem in part (a) into two simpler loading problems for a pair of $\Lambda$-level atoms, now, each illuminated by a biphoton state.

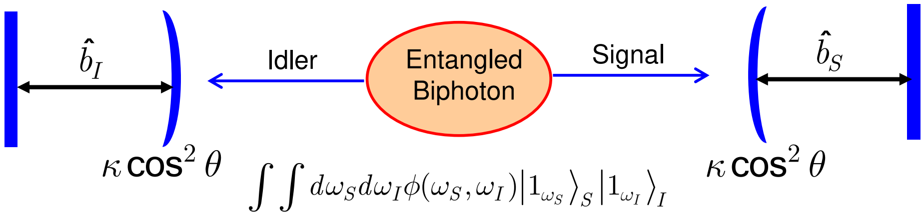

Figure 3-4: A cold-cavity model for the systems shown in Fig. 3-3(b) using the adiabatic-passage loading mechanism. Here, we have assumed that the only levels that can be populated are the dark states in each memory, which in this figure correspond to the cavity mode operators $\hat{b}_S$ and $\hat{b}_I$. Each cavity has a time-dependent decay rate governed by the Rabi frequency associated with the control field.

the state $|e_+\rangle_S|e_-\rangle_I - |e_-\rangle_S|e_+\rangle_I$, where the subscript $S/I$ refers to the atom that is driven by the signal/idler photon.

The above problem can be reduced to the two simpler problems shown in Fig. 3-3(b) by using the linearity in the input superposition state. This is the same technique that we used in Section 2.4 to reduce a $V$-level atom to a pair of two-level atoms. Now that our problem has reduced to the loading problem for two $\Lambda$-level atoms, we can employ the adiabatic and non-adiabatic loading mechanisms introduced in Section 2.3 to solve the MIT-NU loading problem. The following two subsections provide analytical results for the loading probability associated with either of the systems shown in Fig. 3-3(b), which can be directly applied to the case shown in Fig. 3-3(a), or equivalently, to our approximation to the MIT-NU loading problem. Because the two subsystems in Fig. 3-3(b) have essentially the same loading behavior—independent of the polarization of the incoming photons—we simplify our notation in the forthcoming sections by omitting the polarization information.

### 3.2.1 MIT-NU adiabatic loading

In this section, we assume that all the conditions required for adiabatic passage are satisfied so that we can neglect the probability of populating the bright state. In this case, as we showed in Section 2.3.1, each quantum memory can be modeled by a cold cavity with a time-dependent coupling rate $\kappa\cos^2\theta(t)$, where $\cos\theta(t) = \Omega(t)/\sqrt{g_c^2+\Omega^2(t)}$. Then, our loading problem reduces to the case of two empty cavities illuminated by a biphoton state, schematically shown in Fig. 3-4. The driving state in this case is as follows

$$|\psi_0\rangle = \int d\omega_S \int d\omega_I \phi(\omega_S,\omega_I)|1_{\omega_S}\rangle_S|1_{\omega_I}\rangle_I, \tag{3.8}$$

where $\int d\omega_S \int d\omega_I |\phi(\omega_S,\omega_I)|^2 = 1$, and the subscripts $S$ and $I$ refer to the two independent reservoirs that interact with our memory cells. The above state is a superposition of its infinitesimal two-photon elements $\phi(\omega_S,\omega_I)|1_{\omega_S}\rangle_S|1_{\omega_I}\rangle_I d\omega_S d\omega_I$. As was noted in the previous chapter, the governing Schrödinger equations that model the evolution of the reservoirs and cavities are linear, hence the system behaves linearly in response to its initial state. In particular, if we denote the probability amplitude of having one excitation in the signal cavity and one excitation in the idler cavity, both at time $t$, by $\beta_{cc}(t)$, then we have $\beta_{cc}(t) = \int d\omega_S \int d\omega_I \beta_{\omega_S,\omega_I}(t)$, where $\beta_{\omega_S,\omega_I}(t)$ is the probability amplitude for having one excitation in each cavity associated with the input state $\phi(\omega_S,\omega_I)|1_{\omega_S}\rangle_S|1_{\omega_I}\rangle_I$. This input state is a product state of two single photons each illuminating a separate cavity. As a result, we have reduced the two-photon loading problem of Fig. 3-4 to two single-photon single-cavity loading problems of the type studied in Section 2.1. In particular, from (2.10), we obtain

$$\begin{aligned} e^{2i\omega_0 t}\beta_{\omega_S,\omega_I}(t)d\omega_S d\omega_I = -\frac{\kappa}{\pi}\int_0^t d\tau \int_0^t d\tau' \cos\theta(\tau)\cos\theta(\tau')e^{-2K(t)+K(\tau)+K(\tau')} \\ \times \phi(\omega_S,\omega_I)d\omega_S d\omega_I e^{-i(\omega_S-\omega_0)\tau}e^{-i(\omega_I-\omega_0)\tau'}. \end{aligned} \tag{3.9}$$

The loading probability is then calculated as follows:

$$\begin{aligned} P_{loading}(t) &\equiv |\beta_{cc}(t)|^2 \\ &= \left|\int d\omega_S \int d\omega_I \beta_{\omega_S,\omega_I}(t)\right|^2 \\ &= \left|\frac{\kappa}{\pi}\int_0^t d\tau \int_0^t d\tau' \cos\theta(\tau)\cos\theta(\tau')e^{-2K(t)+K(\tau)+K(\tau')}\Phi_b(\tau,\tau')\right|^2, \end{aligned} \tag{3.10}$$

where $\Phi_b(\tau,\tau') = \int d\omega_S \int d\omega_I e^{-i(\omega_S-\omega_0)\tau}e^{-i(\omega_I-\omega_0)\tau'}\phi(\omega_S,\omega_I)$.

Similar to what we found in the single-atom case for $\Omega(t)$, as given by (2.48), $\cos\theta(t)$ is independent of $g_c$, and therefore, our cold-cavity model for adiabatic passage, so long as it prevails, does not reveal any information about the required value of $g_c$. We can again employ a numerical approach to finding the loading probability. This time, however, the number of equations that model the system evolution is much larger than in the single-atom case, which makes their numerical evaluation much more challenging. In the following subsection, we will provide analytical results for the loading probability in the case of a time-

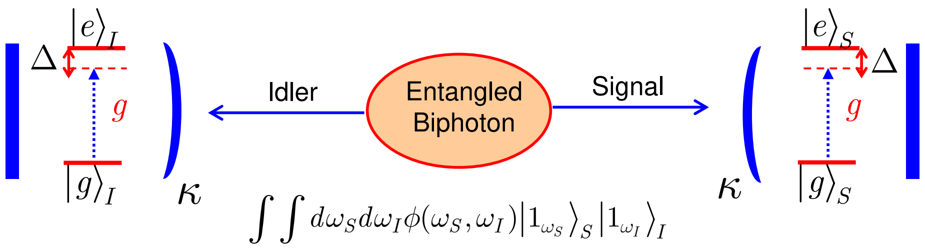

Figure 3-5: A two-level-atom model for the systems shown in Fig. 3-3(b). Here, we have assumed that the Rabi frequency $\Omega$ is a constant and we have adiabatically eliminated the upper state in the $\Lambda$-level atoms. The effective coupling rate is $g = g_c\Omega/\Delta_1$. The effective detuning $\Delta$ can be made zero by a proper choice of other parameters, as described in Fig. 2-8.

independent $\Omega$, and we will demonstrate how the loading probability changes as a function of system parameters.

### 3.2.2 MIT-NU non-adiabatic loading

As we showed in Section 2.3.2, for a time-independent $\Omega$, each $\Lambda$-level atom can be approximated by a two-level atom with an effective coupling rate $g = g_c\Omega/\Delta_1$ and a detuning $\Delta$ that can be made zero by a proper choice of parameters. This reduces the loading problem in Fig. 3-3(b) to the one shown in Fig. 3-5, in which a pair of trapped two-level atoms are illuminated by a biphoton state $|\psi_0\rangle$ as given by (3.8). Here, the loading event corresponds to populating both atomic excited states, i.e., to ending up in the state $|e\rangle_S|e\rangle_I$.

To analyze this loading problem, we can again use the superposition trick that we used in the previous subsection to find $\beta_{ee}(t)$, the slowly-varying probability amplitude at time $t$ associated with $|e\rangle_S|e\rangle_I$. Denoting the slowly-varying probability amplitude at time $t$ associated with $|e\rangle_S|e\rangle_I$ in response to the two-photon state $\phi(\omega_S,\omega_I)|1_{\omega_S}\rangle_S|1_{\omega_I}\rangle_I$ by $\beta_{\omega_S,\omega_I}(t)$, we have

$$\beta_{ee}(t) = \int d\omega_S \int d\omega_I \beta_{\omega_S,\omega_I}(t), \tag{3.11}$$

where, from (2.29),

$$\begin{aligned}\beta_{\omega_S,\omega_I}(t)d\omega_S d\omega_I = \frac{\kappa g^2}{\pi\xi^2}\int_0^t d\tau \int_0^t d\tau' d\omega_S d\omega_I \phi(\omega_S,\omega_I) e^{-i(\omega_S-\omega_0)\tau} e^{-i(\omega_I-\omega_0)\tau'} \\ \times(e^{-\kappa_+(t-\tau)} - e^{-\kappa_-(t-\tau)})(e^{-\kappa_+(t-\tau')} - e^{-\kappa_-(t-\tau')}).\end{aligned} \tag{3.12}$$

The above equation results in the following expression for the time-dependent probability amplitude for being in the state $|e\rangle_S|e\rangle_I$:

$$\beta_{ee}(t) = \frac{\kappa g^2}{\pi\xi^2}\int_0^t d\tau \int_0^t d\tau' \Phi_b(\tau,\tau')(e^{-\kappa_+(t-\tau)} - e^{-\kappa_-(t-\tau)})(e^{-\kappa_+(t-\tau')} - e^{-\kappa_-(t-\tau')}). \quad (3.13)$$

Note that in the above integral only the symmetric part of the pulse shape, $[\Phi_b(\tau,\tau') + \Phi_b(\tau',\tau)]/2$, results in a nonzero value for $\beta_{ee}(t)$. Also, it has been implicitly assumed that the pulse shape $\Phi_b(\tau,\tau')$ is nonzero only for $\tau,\tau' > 0$, otherwise we have to change the lower limits of the above double integral.

### 3.2.3 Numerical results

In this section, we present some numerical results for the performance of MIT-NU non-adiabatic loading mechanism. Our goal is to find the dependence of the loading probability on the bandwidth of the input pulse shape as well as on the atom-light coupling rate. This loading probability is given by $|\beta_{ee}(t)|^2$ as obtained in (3.13). The input pulse shape that we consider here corresponds to the output of an SPDC, which is given by [46]

$$\phi(\omega_S,\omega_I) = A\phi_+(\omega_S,\omega_I)\phi_-(\omega_S,\omega_I). \quad (3.14)$$

In this expression, $A$ is a normalization factor, and

$$\begin{aligned}\phi_+(\omega_S,\omega_I) &= \frac{\sqrt{\omega_S\omega_I}}{n_S(\omega_S)n_I(\omega_I)}\phi_P(\omega_S+\omega_I) \\ &\cong \frac{\omega_0}{n_S(\omega_0)n_I(\omega_0)}\phi_P(\omega_S+\omega_I),\end{aligned} \quad (3.15)$$

where $n_{S/I}$ is the downconversion crystal's refractive index for the signal/idler beam and $\phi_P(\omega)$ is the pump spectral pulse shape. The other term in (3.14) is the phase-matching function,

$$\phi_-(\omega_S,\omega_I) = \frac{\sin[\Delta k(\omega_S,\omega_I)\,L/2]}{\Delta k(\omega_S,\omega_I)/2}, \quad (3.16)$$

where $L$ is the crystal length, and $\Delta k(\omega_S,\omega_I) \equiv k_P(\omega_S+\omega_I) - k_S(\omega_S) - k_I(\omega_I)$, with $k_{S/I/P}$ being the wave number of the signal/idler/pump beam. We assume that the crystal is phase matched at degeneracy, i.e., $k_P(2\omega_0) = k_S(\omega_0) + k_I(\omega_0)$, and that it also satisfies the extended phase-matching condition, $k'_P(2\omega_0) - k'_S(\omega_0) = k'_I(\omega_0) - k'_P(2\omega_0) \equiv \delta k$, where $k'_X(\omega)$, $X = S, I, P$, is the derivative of $k_X$ with respect to $\omega$. We then get the following

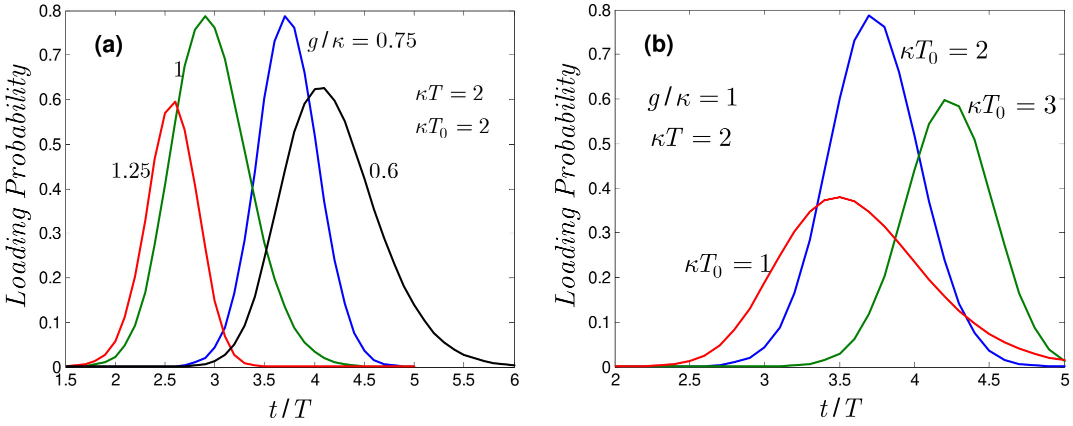

Figure 3-6: (a) MIT-NU loading probability for different values of $g/\kappa$ at $\kappa T = \kappa T_0 = 2$. The maximum probability in each graph is a function of $g/\kappa$, which implies the existence of an optimum value for $g/\kappa$. (b) MIT-NU loading probability for different values of $\kappa T_0$ at $g/\kappa = 1$ and $\kappa T = 2$. In all graphs, we have used a secant hyperbolic pulse shape for the pump beam with $\gamma' = 0$.

linear approximation to $\Delta k(\omega_S, \omega_I)$, for $\delta\omega \equiv \omega_S - \omega_0$ and $\delta\omega' \equiv \omega_I - \omega_0$:

$$\begin{aligned}
\Delta k(\omega_S, \omega_I) &= \Delta k(\omega_0 + \delta\omega, \omega_0 + \delta\omega') \\
&= k_P(2\omega_0 + \delta\omega + \delta\omega') - k_S(\omega_0 + \delta\omega) - k_I(\omega_0 + \delta\omega') \\
&\cong k_P(2\omega_0) + (\delta\omega + \delta\omega')k'_P(2\omega_0) - k_S(\omega_0) - \delta\omega k'_S(\omega_0) - k_I(\omega_0) - \delta\omega' k'_I(\omega_0) \\
&= (\delta\omega - \delta\omega')\delta k = (\omega_S - \omega_I)\delta k. \qquad (3.17)
\end{aligned}$$

Consequently, $\phi_\pm(\omega_S, \omega_I)$ is only a function of the sum/difference frequency $\omega_S \pm \omega_I$. Denoting $\phi_\pm(\omega_S, \omega_I)$ by $\phi_\pm(\omega_S \pm \omega_I)$, the temporal baseband pulse shape needed for our loading probability calculation is therefore

$$\begin{aligned}
\Phi_b(t, u) &= A \int d\delta\omega \int d\delta\omega' \phi_+(\delta\omega + \delta\omega' + 2\omega_0)\phi_-(\delta\omega - \delta\omega')e^{-i\delta\omega t}e^{-i\delta\omega' u} \\
&= \frac{A'}{2}\Phi_b\left(\frac{t+u}{2}\right)\Phi_-\left(\frac{t-u}{2}\right), \qquad (3.18)
\end{aligned}$$

where $A' = A\omega_0/[n_S(\omega_0)n_I(\omega_0)]$, $\Phi_b(t) \equiv e^{2i\omega_0 t}\int d\omega \phi_P(\omega)e^{-i\omega t}$ is the baseband pump pulse shape, and $\Phi_-(t) \equiv \int d\omega \phi_-(\omega)e^{-i\omega t} = (2\pi/\delta k)[u(t + T_0/2) - u(t - T_0/2)]$, for $T_0 = \delta k\, L$.

Figure 3-6 shows the loading probability for the architecture in Fig. 3-5 using a secant hyperbolic pulse shape[1] $\Phi_b(t) = \sqrt{2/T}\mathrm{sech}[4(t - T_0 - 2T)/T]$. We have shifted the pump

---

[1] As we noticed in Fig. 2-5, the choice of pulse shape has a minor effect on the loading probability so long as different pulse shapes have similar bandwidths.

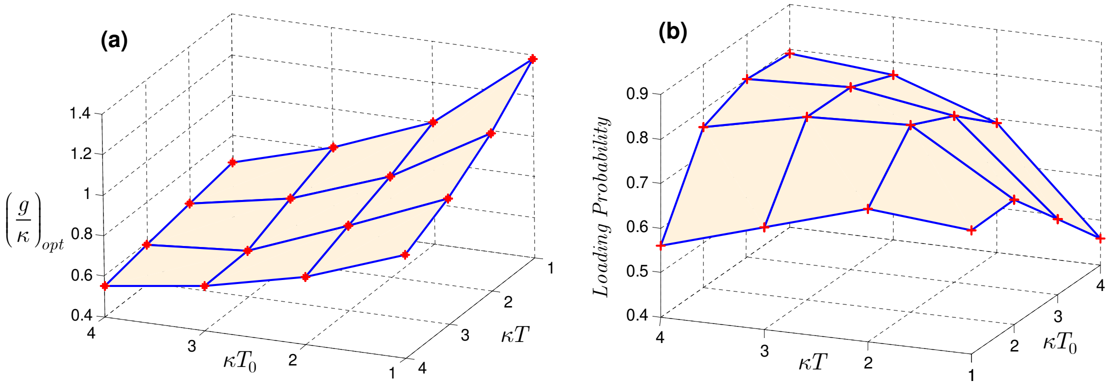

Figure 3-7: (a) The optimum value of $g/\kappa$ versus $\kappa T$ and $\kappa T_0$ for the MIT-NU non-adiabatic loading problem. (b) The corresponding maximum loading probability at $(g/\kappa)_{opt}$. In all graphs, we have used a secant hyperbolic pulse shape for the pump beam with $\gamma' = 0$.

pulse shape by $2T + T_0$ so that, effectively, $\Phi_b(t, u) = 0$ for $t < 0$ or $u < 0$. Now, in addition to its dependence on $g/\kappa$ and $\kappa T$, the loading probability also depends on $\kappa T_0$, which represents the bandwidth of our downconversion process. In Fig. 3-6(a), we have plotted the loading probability for different values of $g/\kappa$ for fixed values of $\kappa T$ and $\kappa T_0$ at $\gamma' = 0$. Similar to what we found in the single-atom case, this figure shows that there exists an optimum value of $g/\kappa$ whose corresponding peak loading probability is maximum. Hence, if we turn the control field off at this particular time, the chance of finding both atoms in their excited states is maximum. Figure 3-6(b) shows the same property from a different perspective. It plots the loading probability with $\kappa T$ and $g/\kappa$ fixed for several values of $\kappa T_0$. Here, we see that there is an optimum value of $\kappa T_0$ for which the loading probability is maximum.

Figure 3-7 shows the optimum value of $g/\kappa$ and its corresponding loading probability as a function of $\kappa T$ and $\kappa T_0$ at $\gamma' = 0$. From Fig. 3-7(a), we observe that higher values of $\kappa T$ or $\kappa T_0$, lead to lower values of $g/\kappa$. This is another manifestation of the trade-off between the input pulse bandwidth and the required coupling rate. The lower the bandwidth is the lower the optimum coupling rate will be. Note that this regime of operation is not applicable to the adiabatic-passage approach on the two-photon resonance, in which the higher the coupling rate is the higher the loading probability will be; see Fig. 2-9. As a result, the non-adiabatic loading mechanism has an advantage in that it allows us to use larger cavities with higher input bandwidth. The price is, however, in the value of loading probability that can be achieved, which as shown in Fig. 3-7(b), is typically on the order of 70%–80%—rather than

100%. From this figure, we achieve higher loading probabilities for $\kappa T_0, \kappa T \geq 2$, where the cavity linewidth is wider than the bandwidths associated with the input pulse.

The initial plan for the MIT-NU architecture calls for cavities with $\kappa \approx 5$ MHz and $g_c \approx 10$ MHz. That leaves a lot of room for choosing $\Omega$ and $\Delta_1$ to operate at the optimum coupling rate $g = g_c\Omega/\Delta_1$. On the other hand, in order to have a high-throughput system it is required to have optical sources with narrow bandwidths comparable to $\kappa$. This can be achieved with the recent progress in building cavity-enhanced SPDCs [47]. Overall, although the loading probabilities that we have obtained in this chapter are under somewhat idealized conditions, their values are high enough to make the 5 dB fixed loss used in Fig. 3-2, not an unduly optimistic, but a conceivably conservative assumption.

# Chapter 4

# Quantum Communication with Atomic Ensembles

As we mentioned earlier in Chapter 1, a key challenge of trapped-atom quantum memories is the loading problem, which is due to the weak coupling between a single atom and a single photon. On the photon's side, this interaction can be enhanced by confining the photon's energy in the small volume of an optical cavity. On the atom's side, this coupling can be enhanced by employing a many-atom system, i.e., an *atomic ensemble*. In the last two chapters, we considered quantum communication systems that employed trapped atoms in optical cavities as quantum memories. In this chapter, we switch gears and describe one of the systems that uses atomic ensembles as quantum memories and study its mechanism for entanglement distribution, as well as its repeater and teleportation schemes. This system, first proposed by Duan, Lukin, Cirac, and Zoller (termed DLCZ, hereafter) [29], uses the from-the-memory configuration in Fig. 1-4 to accomplish entanglement distribution. It is based on weak coherent pumping of a Raman transition in each ensemble followed by path-erasing photodetection. More specifically, collective excitation of an ensemble will radiate a single photon in a well-defined spatial mode. The output modes from the two ensembles are then routed to a common location, e.g., via optical fiber, combined on a 50/50 beam splitter, and detected by a pair of single-photon counters. Because the ensembles are coherently pumped, because the probability that *both* will emit Raman photons will be very low compared to the single-ensemble emission probability, and because the beam splitter combining erases any which-way information, observation of a photocount on one—and only one—detector heralds the entanglement of the two ensembles.

In the following sections we provide a detailed performance analysis for the DLCZ system, and compare it to that of the MIT-NU architecture. We consider the fundamental limitation on the entanglement-distribution performance—throughput and fidelity— that exists for both the DLCZ and MIT-NU architectures: multi-excitation Gaussian input states. For the DLCZ architecture, the input states in question are the joint state of each atomic ensemble and its Stokes-light output. For the MIT-NU architecture, the entangled-Gaussian input states are those for the signal and idler beams of its dual optical parametric amplifier photon source. We also examine the fidelity achieved by the DLCZ teleportation and repeater protocols, under the assumption that successful entanglement distribution has occurred. These results, which are original to this thesis, constitute the first complete performance analysis of the DLCZ system.

## 4.1 DLCZ entanglement distribution

The DLCZ protocol for entangling two nonlocal atomic ensembles is shown schematically in Fig. 4-1(a). The two ensembles—each consisting of $N_a$ identical atoms with $\Lambda$-level configurations, as shown in Fig. 4-1(b)—are coherently pumped using a weak, off-resonant laser such that the probability of occurrence of a Raman transition from the ground level $|g\rangle$ to the metastable level $|s\rangle$, is very low. Because each atom in the left ($L$) or right ($R$) ensemble is equally likely to undergo a Raman transition, the resulting Raman photon is matched to the symmetric collective atomic mode represented by the operator

$$\hat{S}_A = \frac{1}{\sqrt{N_a}} \sum_{n=1}^{N_a} |g\rangle_{A_n\,A_n}\langle s|, \tag{4.1}$$

where the sum is over the atoms in ensemble $A$, for $A \in \{L, R\}$. The forward-scattered Stokes light from such a Raman transition in each ensemble is routed over an $L_0$-km-long path to the midpoint between the locations of the two ensembles. There, the outputs from these optical channels are combined on a 50/50 beam splitter (BS) prior to measurement by a pair of single-photon detectors, $D_1$ and $D_2$, whose dark-count rates will be assumed to be negligible. Assume that the setups for the generation, distribution, and detection of Raman photons are completely symmetric. Furthermore, suppose that only one ensemble

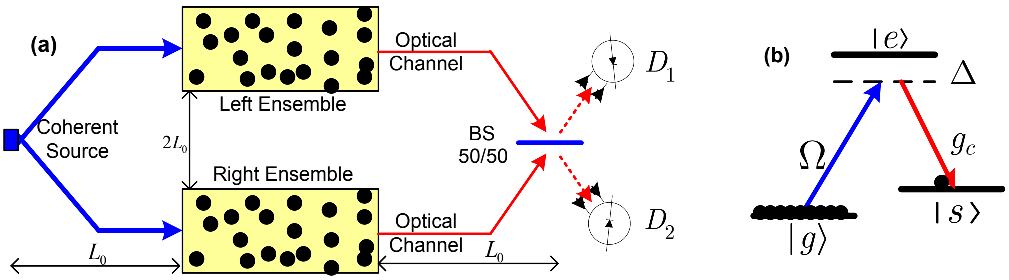

Figure 4-1: (a) DLCZ architecture for entanglement distribution. A coherent laser source, located at the midpoint between two atomic ensembles, induces Raman transitions in these ensembles. Occurrence of a single click on one—and only one—detector heralds the protocol's success, i.e., the atomic ensembles are then expected to be entangled. (b) $\Lambda$-level structure for the atoms in the ensembles: $\Omega$ is the Rabi frequency associated with the off-resonant (detuning $\Delta$) pumping of the $|g\rangle \to |e\rangle$ transition; and $g_c$ is the coupling coefficient for the $|e\rangle \to |s\rangle$ transition.

undergoes a Raman transition, and this transition is detected by detector $D_j$ registering a count. Then, because the pumping is coherent and the beam splitter erases which-path information the two ensembles will be left in the entangled state

$$|\psi_j\rangle \equiv (|0\rangle_L|1\rangle_R + (-1)^j|1\rangle_L|0\rangle_R)/\sqrt{2}, \quad \text{for } j = 1, 2, \tag{4.2}$$

where

$$|0\rangle_A \equiv \bigotimes_{n=1}^{N_a} |g\rangle_{A_n} \text{ and } \ |1\rangle_A \equiv S_A^\dagger|0\rangle_A \quad \text{for } A = L, R, \tag{4.3}$$

are the atomic ground state and symmetric collective excited state of ensemble $A$.

There are a variety of ways by which DLCZ entanglement distribution can err. First, there is the possibility that more than one Raman transition has occurred, e.g. two transitions in one ensemble or one transition in each. A single detector click might still occur in this case. For example, all but one of these multiple Raman photons might be lost en route to the detection setup, or all but one might fail to be detected because of sub-unity detector quantum efficiency. Alternatively, if the single photon detectors in Fig. 4-1(a) are Geiger-mode avalanche photodiodes (APDs)—which are incapable of distinguishing multiple-photon pulses from single-photon pulses—then the clicking of one and only one of the two detectors would not guarantee that only one Raman photon had been seen. In all of these circumstances the DLCZ protocol would announce that the ensembles were now entangled, according to (4.2), when in fact the joint state of these two ensembles would not be given by this expression. Hence any reliance on (4.2), say for the performance of qubit teleportation, would be unwarranted.

Another reason that the DLCZ ensembles might not be left in one of the maximally entangled states from (4.2) is due to asymmetries in the system. For example, an imbalance between the total loss seen by each Raman photon and/or different pump power at each ensemble will strengthen the $|1\rangle_L|0\rangle_R$ component of (4.2) relative to its $|0\rangle_L|1\rangle_R$ component or *vice versa*. Phase mismatch, arising from different pump phases and/or unequal accumulated phases en route to the detectors, can also severely degrade the fidelity of entanglement distribution. We will assume that any systematic (deterministic) phase mismatch has been compensated by means of additional phase shifters, but we will include a random phase offset to account for possible errors in this process.

Other error mechanisms for DLCZ entanglement distribution include detector dark counts, which can masquerade as Raman photon detections, and the spatial-mode mismatch, which arises in a 3D treatment of the atomic ensembles [48]. The dark-count rates of silicon Geiger-mode APDs are sufficiently low, at wavelengths of interest for several atomic species, that we shall neglect dark counts in our analysis. Moreover, we neglect the subtleties that arise in a 3D treatment of the problem by assuming a pencil-shaped ensemble with almost unity Fresnel number (ensemble cross-sectional area divided by the product of its length and the pump-laser's wavelength) [49]. We also neglect the effects of spontaneous emission, whose significance is reduced by the off-resonant pumping and the signal-to-noise ratio enhancement afforded by the collective atomic behavior [29]. Finally, we assume that the coherence time of the ensembles is long enough to allow for a few runs of each protocol in a long-distance scenario [50, 51].

In what follows, we will derive the performance of DLCZ entanglement distribution when it is limited by the possibility of multiple Raman-transition events. We start from the Gaussian entangled-state characterization of the atomic ensembles and their associated Stokes light, allowing for pump phase/amplitude errors. The Stokes light is then propagated through to the detection system, considering propagation losses as well as sub-unity quantum efficiencies. The resulting transformed Gaussian state is then used to evaluate the fidelity and throughput of the DLCZ protocol when we employ either non-resolving photon detectors (NRPDs), i.e., detectors that are incapable of distinguishing single-photon from multiple-photon events, or photon-number resolving detectors (PNRDs) that can draw such distinctions.

### 4.1.1 Atomic-photonic initial joint state

Neglecting spontaneous emission, the joint state of a $\Lambda$-level atomic ensemble—held within a ring cavity of decay rate $\kappa$ and pumped for $t_\Delta$ sec at Rabi frequency $\Omega$ and detuning $\Delta$—and its associated Stokes light is the entangled (two-mode squeezed) state [29]:

$$|\psi\rangle = \frac{1}{\cosh r} \sum_{n=0}^{N_a} \frac{(\hat{S}_a^\dagger \hat{a}_p^\dagger \, e^{i\theta} \tanh r)^n \, |0_a\rangle \, |0_p\rangle}{n!}. \tag{4.4}$$

In (4.4), $\hat{S}_a$ and $\hat{a}_p$ are the annihilation operators for the symmetric collective atomic mode and the effective mode for the Stokes light, respectively, $\theta$ is the pump-phase offset, and

$$\cosh r = \exp(2N_a \, |\Omega g_c|^2 \, t_\Delta / \Delta^2 \kappa), \tag{4.5}$$

specifies the squeeze parameter, $r$, for this state. Our calculations below will rely on an equivalent specification for this joint state, i.e., its antinormally-ordered characteristic function [52]:

$$\begin{aligned} \chi_A^{\nu\mu}(\zeta_a, \zeta_p) &\equiv \left\langle \hat{D}_A(\hat{S}_a, \zeta_a) \hat{D}_A(\hat{a}_p, \zeta_p) \right\rangle \\ &= \exp\left[ - |\mu|^2 \left( |\zeta_a|^2 + |\zeta_p|^2 \right) - 2\mathrm{Re}(\mu\nu\zeta_a^* \zeta_p^*) \right], \end{aligned} \tag{4.6}$$

where $\nu = -\sinh r \exp(i\theta)$, $\mu = \cosh r$, and $\hat{D}_A(\hat{a}, \zeta) \equiv e^{-\zeta^* \hat{a}} e^{\zeta \hat{a}^\dagger}$ is the antinormally-ordered displacement operator. Because $\chi_A^{\nu\mu}$ is a Gaussian form, we say that $|\psi\rangle$ is a Gaussian state.

Using (4.6), we have that the joint state, $\hat{\rho}_{\text{in}}$, of the two atomic ensembles and their Stokes light at the optical channel inputs in Fig. 4-1(a) has the following antinormally-ordered characteristic function:

$$\chi_A^{\hat{\rho}_{\text{in}}}(\zeta_a^L, \zeta_a^R, \zeta_p^L, \zeta_p^R) = \chi_A^{\nu_L \mu_L}(\zeta_a^L, \zeta_p^L) \chi_A^{\nu_R \mu_R}(\zeta_a^R, \zeta_p^R), \tag{4.7}$$

where $\nu_A / \mu_A = \sqrt{p_{c_A}} \exp(i\theta_A)$ and $A \in \{L, R\}$. Here, $\theta_L$ and $\theta_R$ model the phase offsets for the left and right ensembles, respectively. They include the pump-phase jitter as well as the residual phase shifts accumulated by the Stokes photons along the optical channel. We will ultimately treat these phase shifts as zero-mean random variables by assuming that a

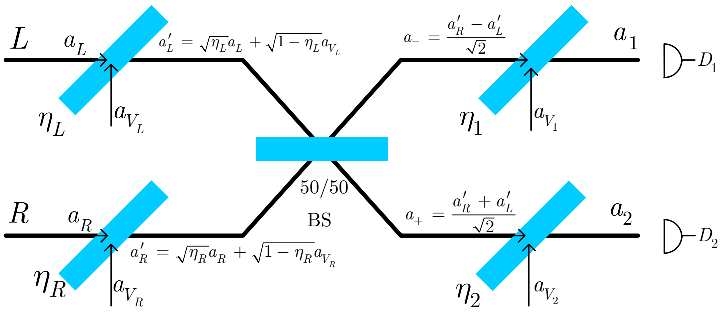

Figure 4-2: Notional model for the optical channels shown in Fig. 4-1(a). Fictitious beam splitters are used to account for the loss of Raman photons and the quantum noise introduced by propagation from the atomic ensembles to the 50/50 beam splitter in Fig. 4-1(a), and by the sub-unity quantum efficiencies of the detectors appearing in that figure. The detectors in Fig. 4-2 have unity quantum efficiencies.

phase-compensating mechanism is being employed. For now, however, we will regard them as known constants for a single round of entanglement distribution. From (4.4), the probability of exciting a single Raman transition in ensemble $A$ is $p_{c_A}(1-p_{c_A})$, which becomes $p_{c_A} \ll 1$ under weak pumping conditions.

### 4.1.2 Optical channel output

Figure 4-2 depicts our model for the optical channels shown in Fig. 4-1(a). Here, propagation losses between the atomic ensembles and the 50/50 coupling beam splitter from Fig. 4-1(a) are represented by fictitious beam splitters whose free input ports inject vacuum-state quantum noise. Additional fictitious beam splitters are placed after the 50/50 coupling beam splitter—again with vacuum-state quantum noise injected through their free input ports—to account for the sub-unity quantum efficiencies of the detectors shown in Fig. 4-1(a). Thus, detectors $D_1$ and $D_2$ in Fig. 4-2 are taken to have unity quantum efficiencies. The transmissivity, vacuum field, and output field associated with each beam splitter have been shown in the figure. We assume that any phase offsets accumulated in propagation for the left and right arms have been incorporated into $\theta_L$ and $\theta_R$ in (4.7). The optical channel consists of linear optical elements for which we can write input-output operator relations. Doing that, we then have that the annihilation operators for the fields reaching the Fig. 4-2 detectors are [53]

$$\begin{aligned}\hat{a}_1 &= \sqrt{\frac{\eta_1}{2}}(\sqrt{\eta_R}\hat{a}_R + \sqrt{1-\eta_R}\hat{a}_{V_R}) \\ &\quad -\sqrt{\frac{\eta_1}{2}}(\sqrt{\eta_L}\hat{a}_L + \sqrt{1-\eta_L}\hat{a}_{V_L}) + \sqrt{1-\eta_1}\hat{a}_{V_1} \qquad (4.8a)\\ \hat{a}_2 &= \sqrt{\frac{\eta_2}{2}}(\sqrt{\eta_R}\hat{a}_R + \sqrt{1-\eta_R}\hat{a}_{V_R}) \\ &\quad +\sqrt{\frac{\eta_2}{2}}(\sqrt{\eta_L}\hat{a}_L + \sqrt{1-\eta_L}\hat{a}_{V_L}) + \sqrt{1-\eta_2}\hat{a}_{V_2}, \qquad (4.8b)\end{aligned}$$

where $\hat{a}_{V_{L,R}}$ and $\hat{a}_{V_{1,2}}$ are in their vacuum states, and $\hat{a}_L$ and $\hat{a}_R$ are, respectively, the associated field operators for the Raman photons originating from the left and right ensembles. These linear transformations preserve the Gaussian-state nature of their inputs. In particular, using (4.8), we have that the joint state, $\hat{\rho}_{\text{out}}$, of the two atomic ensembles and their Stokes light arriving at the Fig. 4-2 detectors has an antinormally-ordered characteristic function given by

$$\begin{aligned}\chi_A^{\hat{\rho}_{\text{out}}}(\zeta_a^L, \zeta_a^R, \zeta_{p1}, \zeta_{p2}) &\equiv \left\langle \hat{D}_A(\hat{S}_L, \zeta_a^L)\hat{D}_A(\hat{S}_R, \zeta_a^R)\hat{D}_A(\hat{a}_1, \zeta_{p1})\hat{D}_A(\hat{a}_2, \zeta_{p2})\right\rangle \\ &= \chi_A^{\hat{\rho}_{\text{in}}}(\zeta_a^L, \zeta_a^R, \sqrt{\eta_L}\zeta_p^-, \sqrt{\eta_R}\zeta_p^+) \\ &\quad \times \exp\left[-(1-\eta_1)\left|\zeta_{p1}\right|^2 - (1-\eta_2)\left|\zeta_{p2}\right|^2\right] \\ &\quad \times \exp\left[-(1-\eta_L)\left|\zeta_p^-\right|^2 - (1-\eta_R)\left|\zeta_p^+\right|^2\right], \qquad (4.9)\end{aligned}$$

where

$$\zeta_p^{\pm} = \sqrt{\frac{\eta_2}{2}}\zeta_{p2} \pm \sqrt{\frac{\eta_1}{2}}\zeta_{p1}\,. \qquad (4.10)$$

Then, by employing (4.6) and (4.7) in (4.9), we get

$$\begin{aligned}\chi_A^{\hat{\rho}_{\text{out}}}(\zeta_a^L, \zeta_a^R, \zeta_{p1}, \zeta_{p2}) &= \exp\left[-\frac{\alpha_L}{2}\left|\zeta_a^L\right|^2 - \frac{\beta_L}{2}\left|\zeta_p^-\right|^2\right. \\ &\quad -\gamma_L \text{Re}\{e^{i\theta_L}\zeta_a^{L*}\zeta_p^{-*}\} - \delta\text{Re}\{\zeta_p^+\zeta_p^{-*}\} \\ &\quad \left.-\gamma_R \text{Re}\{e^{i\theta_R}\zeta_a^{R*}\zeta_p^{+*}\} - \frac{\alpha_R}{2}\left|\zeta_a^R\right|^2 - \frac{\beta_R}{2}\left|\zeta_p^+\right|^2\right], \qquad (4.11)\end{aligned}$$

where

$$\alpha_A = 2|\mu_A|^2 = 2/(1 - p_{c_A})\,, \tag{4.12a}$$

$$\beta_A = \eta_A p_{c_A}\alpha_A + (\eta_1 + \eta_2)/(\eta_1\eta_2)\,, \tag{4.12b}$$

$$\gamma_A = \sqrt{\eta_A p_{c_A}}\alpha_A\,, \tag{4.12c}$$

$$\delta = (\eta_1 - \eta_2)/(\eta_1\eta_2)\,, \tag{4.12d}$$

for $A = L, R$. Therefore, we can think of the complex vector $[\zeta_a^L, \zeta_p^-, \zeta_p^+, \zeta_a^R]$ as a zero-mean Gaussian random vector whose covariance matrix can be determined from (4.11), see Appendix B for details. In our subsequent analysis we will use this fact to evaluate probabilities of interest via Gaussian moment relations.

The output density operator can be written in terms of its respective antinormally-ordered characteristic function via the following operator-valued inverse Fourier transform relation:

$$\begin{aligned}\hat{\rho}_{\rm out} &= \int \frac{{\rm d}^2\zeta_a^L}{\pi} \int \frac{{\rm d}^2\zeta_a^R}{\pi} \hat{D}_N(\hat{S}_L, \zeta_a^L)\hat{D}_N(\hat{S}_R, \zeta_a^R) \\ &\times \int \frac{{\rm d}^2\zeta_{p1}}{\pi} \int \frac{{\rm d}^2\zeta_{p2}}{\pi}\, \chi_A^{\hat{\rho}_{\rm out}}(\zeta_a^L, \zeta_a^R, \zeta_{p1}, \zeta_{p2})\hat{D}_N(\hat{a}_1, \zeta_{p1})\hat{D}_N(\hat{a}_2, \zeta_{p2})\,,\end{aligned} \tag{4.13}$$

where $\hat{D}_N(\hat{a}, \zeta) \equiv e^{-\zeta\hat{a}^\dagger}e^{\zeta^*\hat{a}}$ is the normally-ordered displacement operator, and $\int {\rm d}^2\zeta \equiv \int\int {\rm d}\zeta_r {\rm d}\zeta_i$, where $\zeta_r$ and $\zeta_i$ are, respectively, the real and imaginary parts of $\zeta$. We use this convention throughout the paper.

### 4.1.3 Measurement modules

The occurrence of a detection click on one, and only one, of the photodetectors $D_1$ and $D_2$ is used to herald entanglement distribution in the DLCZ protocol. We shall consider both non-resolving single-photon detectors (NRPDs), which are incapable of distinguishing multiple-photon pulses from single-photon pulses, as well as photon-number resolving detectors (PNRDs), which are capable of making such distinctions. The latter, which were not considered in the original DLCZ protocol, allow suppression of error events that were undetectable with NRPDs, i.e., the PNRD version of the entanglement-distribution protocol heralds entanglement distribution when exactly one photon is detected by the $\{D_1, D_2\}$ pair.

Let $\hat{M}_1$ and $\hat{M}_2$ be measurement projectors on the joint state space of the $\hat{a}_1$ and $\hat{a}_2$ modes that represent DLCZ heralding events in which detections occur on $D_1$ and $D_2$, respectively. For example, $\hat{M}_1$, in the NRPD case, implies the detection of a single click (one or more photons) on detector $D_1$ and none on detector $D_2$; in the PNRD case this operator implies the detection of exactly one photon on $D_1$ and none on $D_2$. From these descriptions we get the following explicit forms for $\hat{M}_1$ and $\hat{M}_2$:

$$\hat{M}_1 = \begin{cases} |1\rangle_{1\,1}\langle 1| \otimes |0\rangle_{2\,2}\langle 0|\,, & \text{PNRD} \\ (\hat{I}_1 - |0\rangle_{1\,1}\langle 0|) \otimes |0\rangle_{2\,2}\langle 0|\,, & \text{NRPD,} \end{cases} \tag{4.14}$$

$$\hat{M}_2 = \begin{cases} |0\rangle_{1\,1}\langle 0| \otimes |1\rangle_{2\,2}\langle 1|\,, & \text{PNRD} \\ |0\rangle_{1\,1}\langle 0| \otimes (\hat{I}_2 - |0\rangle_{2\,2}\langle 0|), & \text{NRPD,} \end{cases} \tag{4.15}$$

where $\hat{I}_1$ and $\hat{I}_2$ denote the identity operators for the $\hat{a}_1$ and $\hat{a}_2$ modes, respectively.

Suppose that the DLCZ protocol (with either NRPDs or PNRDs) has heralded entanglement distribution, based on observing a click from $D_j$ and no click from $D_i$, where $i, j = 1, 2$ and $i \neq j$. The post-measurement joint density operator for the two atomic ensembles, $\hat{\rho}_{\text{pm}_j}$, can be found by projecting with $\hat{M}_j$, tracing out the photonic variables, and renormalizing, viz.

$$\hat{\rho}_{\text{pm}_j} = \frac{\text{tr}_{1,2}(\hat{\rho}_{\text{out}} \hat{M}_j)}{P_j}, \tag{4.16}$$

where

$$P_j = \text{tr}(\hat{\rho}_{\text{out}} \hat{M}_j) \tag{4.17}$$

is the probability that the conditioning event $\hat{M}_j$ has occurred. The total probability that the DLCZ protocol heralds an entanglement distribution is then $P_{\text{herald}} = P_1 + P_2$. Note that $P_{\text{herald}}$ is *not* the probability that the atomic ensembles have been placed into the entangled state $|\psi_j\rangle$ if $\hat{M}_j$ has occurred. The success probability, $P_{\text{success}}$, for creating this entanglement is

$$P_{\text{success}} = P_1 \langle \psi_1 | \hat{\rho}_{\text{pm}_1} | \psi_1 \rangle + P_2 \langle \psi_2 | \hat{\rho}_{\text{pm}_2} | \psi_2 \rangle, \tag{4.18}$$

i.e., the heralding probabilities, $P_j$, must be multiplied by their associated fidelities, $F_j \equiv \langle \psi_j | \hat{\rho}_{\text{pm}_j} | \psi_j \rangle$, for successful entanglement distribution. These fidelities will be less than unity, because of higher-order (multiple-photon) components in the input state $\hat{\rho}_{\text{in}}$.

In the remainder of this section, we shall find the post-measurement states, $\{\hat{\rho}_{\mathrm{pm}_j}\}$, the heralding probabilities, $\{P_j\}$, and the fidelities of entanglement, $\{F_j\}$, for DLCZ entanglement distribution. Both PNRD and NRPD systems will be considered.

### Photon-number resolving detectors

It can be easily verified that for any single-mode annihilation operator $a$ and complex variable $\zeta$, we have

$$\langle 0|\hat{D}_N(\hat{a},\zeta)|0\rangle = 1 \text{ and } \langle 1|\hat{D}_N(\hat{a},\zeta)|1\rangle = 1-|\zeta|^2\,. \tag{4.19}$$

Using these results, together with (4.13) and (4.16) plus the PNRD cases from (4.14) and (4.15), we get

$$\begin{aligned}\hat{\rho}_{\mathrm{pm}_j} = \frac{1}{P_j}\int\frac{\mathrm{d}^2\zeta_a^L}{\pi}\int\frac{\mathrm{d}^2\zeta_a^R}{\pi}\hat{D}_N(\hat{S}_L,\zeta_a^L)\hat{D}_N(\hat{S}_R,\zeta_a^R)\\ \times\int\frac{\mathrm{d}^2\zeta_{p1}}{\pi}\int\frac{\mathrm{d}^2\zeta_{p2}}{\pi}\,\chi_A^{\hat{\rho}_{\mathrm{out}}}(\zeta_a^L,\zeta_a^R,\zeta_{p1},\zeta_{p2})\left(1-|\zeta_{pj}|^2\right),\end{aligned} \tag{4.20}$$

whence, by means of (4.17) and the identity $\mathrm{tr}(\hat{D}_N(\hat{a},\zeta)) = \pi\delta(\zeta)$,

$$P_j = \int\frac{\mathrm{d}^2\zeta_{p1}}{\pi}\int\frac{\mathrm{d}^2\zeta_{p2}}{\pi}\,\chi_A^{\hat{\rho}_{\mathrm{out}}}(0,0,\zeta_{p1},\zeta_{p2})\left(1-|\zeta_{pj}|^2\right). \tag{4.21}$$

The above integral can be evaluated from moments that are directly identifiable from the Gaussian characteristic function in (4.11), and we obtain (see Appendix B for details)

$$P_j = \frac{4}{\eta_1\eta_2(\beta_L\beta_R-\delta^2)}\left(1-\frac{\beta_L+\beta_R-2(-1)^j\delta}{\eta_j(\beta_L\beta_R-\delta^2)}\right), \quad \text{for } j=1,2. \tag{4.22}$$

In the special case of a symmetric setup, in which $\eta_L = \eta_R$, $\eta_1 = \eta_2$, $\theta_L = \theta_R$, and $p_{c_L} = p_{c_R} \equiv p_c$, the preceding expression reduces to

$$P_j = \frac{(1-p_c)^2\eta_s p_c}{(\eta_s p_c + 1 - p_c)^3}, \quad \text{for } j=1,2, \tag{4.23}$$

where $\eta_s = \eta_L\eta_1$ is the system efficiency. In this case $P_1 = P_2$ holds, owing to the symmetry of the optical channels and the measurement modules. More generally, $\eta_1 = \eta_2$ implies $P_1 = P_2$, because this condition suffices to make $D_1$ and $D_2$ photon detections equally likely.

**Non-resolving photon detectors**

Similar to the PNRD case, we start from

$$\operatorname{tr}\Big[\hat{D}_N(\hat{a},\zeta)\,(I-|0\rangle\,\langle 0|)\Big]=\pi\delta(\zeta)-1 \tag{4.24}$$

along with (4.19), (4.13), (4.16) plus the NRPD cases from (4.14) and (4.15), and obtain

$$\begin{aligned}\hat{\rho}_{\mathrm{pm}_j} &= \frac{1}{P_j}\int\frac{\mathrm{d}^2\zeta_a^L}{\pi}\int\frac{\mathrm{d}^2\zeta_a^R}{\pi}\,\hat{D}_N(\hat{S}_L,\zeta_a^L)\hat{D}_N(\hat{S}_R,\zeta_a^R)\\ &\quad\times\int\frac{\mathrm{d}^2\zeta_{p1}}{\pi}\int\frac{\mathrm{d}^2\zeta_{p2}}{\pi}\,\chi_A^{\hat{\rho}_{\mathrm{out}}}(\zeta_a^L,\zeta_a^R,\zeta_{p1},\zeta_{p2})\,(\pi\delta(\zeta_{pj})-1), \end{aligned}\tag{4.25}$$

where

$$\begin{aligned}P_j &= \int\frac{\mathrm{d}^2\zeta_{p1}}{\pi}\int\frac{\mathrm{d}^2\zeta_{p2}}{\pi}\,\chi_A^{\hat{\rho}_{\mathrm{out}}}(0,0,\zeta_{p1},\zeta_{p2})\,(\pi\delta(\zeta_{pj})-1)\\ &= \frac{4}{\eta_i(\beta_L+\beta_R-2(-1)^j\delta)}-\frac{4}{\eta_1\eta_2(\beta_L\beta_R-\delta^2)},\qquad \text{for } i,j=1,2,\ i\neq j. \end{aligned}\tag{4.26}$$

For the symmetric setup, the above probability simplifies to

$$P_j=\frac{(1-p_c)\eta_s p_c}{(\eta_s p_c+1-p_c)^2},\quad \text{for } j=1,2. \tag{4.27}$$

As was the case for PNRDs, $\eta_1=\eta_2$ is again enough to ensure that $P_1=P_2$. Comparison of (4.23) and (4.27) reveals that $P_j$ for the NRPD case is higher than $P_j$ for the PNRD case. This is to be expected, because the heralding events included in the latter probability are a proper subset of those included in the former. None of the heralding probabilities depends on the phase offset, because our measurement modules are only sensitive to the photon number. The impact of phase offset will appear when we calculate the fidelity of entanglement.

### 4.1.4 Fidelity of DLCZ entanglement distribution

The DLCZ fidelities of entanglement realized with PNRD and NRPD systems are

$$\begin{aligned}
F_j &\equiv \langle\psi_j|\hat{\rho}_{\mathrm{pm}_j}|\psi_j\rangle \\
&= \frac{1}{P_j}\int\frac{\mathrm{d}^2\zeta_a^L}{\pi}\int\frac{\mathrm{d}^2\zeta_a^R}{\pi}\left(1-\left|\zeta_a^L+(-1)^j\zeta_a^R\right|^2/2\right) \\
&\quad\times\int\frac{\mathrm{d}^2\zeta_{p1}}{\pi}\int\frac{\mathrm{d}^2\zeta_{p2}}{\pi}\,\chi_A^{\hat{\rho}_{\mathrm{out}}}(\zeta_a^L,\zeta_a^R,\zeta_{p1},\zeta_{p2})\left(1-|\zeta_{pj}|^2\right), \qquad (4.28)
\end{aligned}$$

for $j=1,2$ in the PNRD case, and

$$\begin{aligned}
F_j &= \frac{1}{P_j}\int\frac{\mathrm{d}^2\zeta_a^L}{\pi}\int\frac{\mathrm{d}^2\zeta_a^R}{\pi}\left(1-\left|\zeta_a^L+(-1)^j\zeta_a^R\right|^2/2\right) \\
&\quad\times\int\frac{\mathrm{d}^2\zeta_{p1}}{\pi}\int\frac{\mathrm{d}^2\zeta_{p2}}{\pi}\,\chi_A^{\hat{\rho}_{\mathrm{out}}}(\zeta_a^L,\zeta_a^R,\zeta_{p1},\zeta_{p2})\left(\pi\delta(\zeta_{pj})-1\right), \qquad (4.29)
\end{aligned}$$

for $j=1,2$ in the NRPD case, where we have used

$$\langle\psi_j|\hat{D}_N(\hat{S}_L,\zeta_a^L)\hat{D}_N(\hat{S}_R,\zeta_a^R)|\psi_j\rangle = 1-\frac{\left|\zeta_a^L+(-1)^j\zeta_a^R\right|^2}{2}. \qquad (4.30)$$

Both (4.28) and (4.29) can be evaluated via moment analysis from the Gaussian nature of (4.11), yielding

$$\begin{aligned}
F_j &= [\eta_j(1-p_{c_L})(1-p_{c_R})/(4P_j)] \\
&\quad\times(\eta_L p_{c_L}+\eta_R p_{c_R}+2\sqrt{\eta_L p_{c_L}\eta_R p_{c_R}}\cos(\theta_L-\theta_R)), \quad \text{for } j=1,2, \qquad (4.31)
\end{aligned}$$

where for each detection scheme we use its corresponding heralding probability $P_j$. Note that $F_jP_j$ is identical for both PNRD and NRPD systems. This can be qualitatively justified as follows. $F_j$ is the conditional probability of a successful entanglement creation given that a heralding event has occurred. Hence, $F_jP_j$ is the joint probability of successfully loading the ensembles in state $|\psi_j\rangle$ and the occurrence of the $\hat{M}_j$ event. This joint event occurs when one—and only one—of the ensembles undergoes a single Raman transition to produce exactly one photon, and this photon is detected by photodetector $D_j$. Photon-number resolution is not required for detecting a single photon, therefore both PNRD and NRPD systems have the same likelihood of a loading success. It follows that the success probability, $P_{\text{success}}$, is the same for the PNRD and NRPD systems, so in Appendix B we will only present a derivation of (4.31) for the PNRD case.

The fidelity in (4.31) is independent of which detector has clicked, provided that the detectors have the same efficiency, viz. $\eta_1 = \eta_2$. In this case, we have $P_{\text{success}} = F_E P_{\text{herald}}$, where $F_E \equiv F_1 = F_2$. (Here, the subscript $E$ emphasizes that we are concerned with the fidelity of entanglement.) This means that the lower heralding probability of the PNRD system, relative to that of its NRPD counterpart, is exactly compensated by its higher fidelity of entanglement.

It is interesting to compare the behavior of the NRPD and PNRD fidelities of entanglement as we vary key system parameters. For this purpose, it is easier to consider what happens in the symmetric case, when everything is identical for both ensembles and their corresponding Raman photons. We then have

$$P_{\text{success}} = 2\eta_s p_c (1-p_c)^2, \quad \text{symmetric setup} \tag{4.32}$$

and

$$F_{E,\text{sym}} = \begin{cases} (\eta_s p_c + 1 - p_c)^3, & \text{PNRD} \\ \\ (1-p_c)(\eta_s p_c + 1 - p_c)^2, & \text{NRPD.} \end{cases} \tag{4.33}$$

The success probability of a symmetric setup, given by (4.32), can also be obtained by the following simple argument. A success occurs whenever one—and only one—of the ensembles produces a Raman photon and this photon is detected. In (4.32), $P_{\text{success}}$ is the product of $p_c(1-p_c)$ (the probability of one excitation) times $1-p_c$ (the probability of no excitations) times $\eta_s/2$ (the survival probability for one photon) times 4 (the number of possibilities, all equiprobable, for emitting a single photon and getting a detector click).

From (4.33), we see that both the PNRD and NRPD $F_E$ expressions approach $(1-p_c)^3 \simeq 1-3p_c$ for $p_c \ll 1$ as the system efficiency $\eta_s$ approaches zero; this limit is in accord with preliminary results reported in the DLCZ paper [29]. In Fig. 4-3(a), we have plotted $F_E$ versus $\eta_s$ for the PNRD and NRPD systems. From this figure we see that the PNRD system realizes perfect fidelity in the absence of loss ($\eta_s = 1$), whereas $F_E = 1 - p_c$ for lossless operation of the NRPD system. Figure 4-3(b) shows that the NRPD system is more sensitive to excitation probability ($p_c$) variations than is the PNRD system. For $p_c \ll 1$, both systems approach perfect fidelity, but significant fidelity degradations occur for larger values of $p_c$.

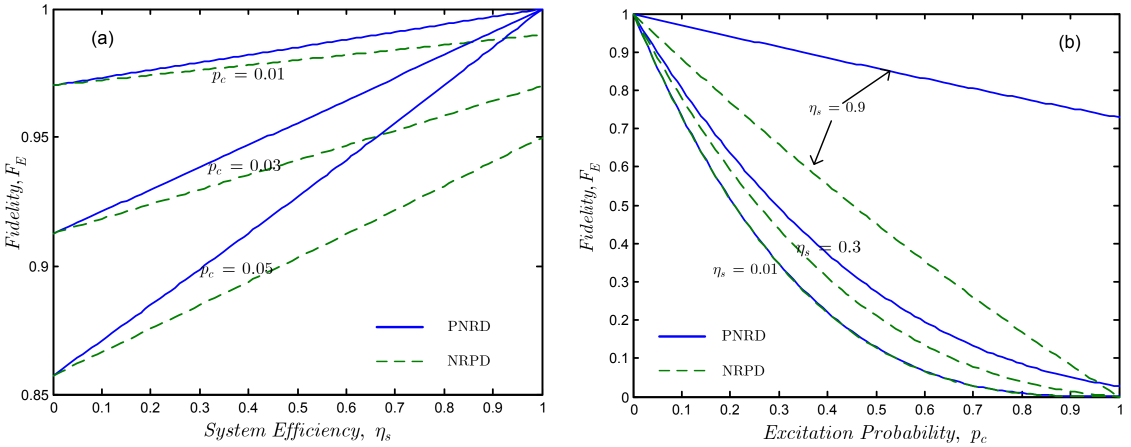

Figure 4-3: Fidelity of entanglement, $F_E$, versus (a) system efficiency, $\eta_s$, and (b) excitation probability, $p_c$, for DLCZ entanglement distribution. In both (a) and (b), we assume that the system setup is symmetric.

Indeed, from (4.33), we find that the NRPD system has zero fidelity at $p_c = 1$, whereas the PNRD system achieves $F_E = \eta_s^3$. Overall, in a practical operating regime in which $p_c \approx 0.01$ and $\eta_s \approx 0.01 - 0.1$ prevail, the PNRD and NRPD systems have very similar entanglement-distribution performance. This is important because NRPD technology is more advanced than PNRD technology.

### 4.1.5 Asymmetric setup and state preparation

DLCZ entanglement distribution in an asymmetric configuration can be looked at in two different, but interrelated, ways. The first, which is the approach we have taken in deriving (4.31), is to quantify the asymmetry-induced fidelity loss with respect to the maximally-entangled (singlet or triplet) states. Deviations from complete symmetry, however, will make one path more probable than the other, and/or introduce relative phase terms. Hence, the pure state for the two ensembles that is the best fit to their post-heralding joint density operator is, in general, a partially-entangled state of the form $d_L|1\rangle_L|0\rangle_R + d_R|0\rangle_L|1\rangle_R$, where $d_L$ and $d_R$ are functions of system parameters. This leads us to the second point of view, i.e., finding the most-likely (maximum-fidelity) pure state for the asymmetric setup. The answer to this question provides us with a prescription for preparing the two ensembles in an arbitrary partially-entangled state. In Appendix B we show that the fidelity-maximizing state is

$$\begin{aligned}|\psi_j\rangle_{\rm max} &= \frac{\sqrt{\eta_L p_{c_L}}}{\sqrt{\eta_L p_{c_L}+\eta_R p_{c_R}}}|1\rangle_L|0\rangle_R + (-1)^j e^{i(\theta_R-\theta_L)} \\ &\times \frac{\sqrt{\eta_R p_{c_R}}}{\sqrt{\eta_L p_{c_L}+\eta_R p_{c_R}}}|0\rangle_L|1\rangle_R, \text{ for } j=1,2, \end{aligned} \tag{4.34}$$

and the fidelity maximum that it achieves is

$$\begin{aligned}F_{j,\rm max} &\equiv {}_{\rm max}\langle\psi_j|\hat{\rho}_{{\rm pm}_j}|\psi_j\rangle_{\rm max} \\ &= \frac{\eta_j(1-p_{c_L})(1-p_{c_R})(\eta_L p_{c_L}+\eta_R p_{c_R})}{2P_j}, \end{aligned} \tag{4.35}$$

for $j = 1, 2$. This is an intuitive result. The joint probability that $D_j$ clicks and that this click heralds successful loading of the state $|\psi_j\rangle_{\rm max}$ is $P_j F_{j,\rm max}$, which is given by the probability, $p_{c_{L/R}}(1-p_{c_L})(1-p_{c_R})$, of having exactly one excitation in only the left/right ensemble times the probability, $\eta_j\eta_{L/R}/2$, that the associated Raman photon is detected by $D_j$.

A similar argument holds for the maximum-fidelity state in (4.34). Here, the ratio between the probability of being in state $|1\rangle_L|0\rangle_R$ rather than in state $|0\rangle_L|1\rangle_R$ is $\eta_L p_{c_L}/(\eta_R p_{c_R})$, as expected. This ratio does not depend on the detector efficiencies, because the 50/50 beam splitter gives Raman photons an equal chance to be directed to $D_1$ or $D_2$. On the other hand, the coherence between states $|1\rangle_L|0\rangle_R$ and $|0\rangle_L|1\rangle_R$ is impacted by the phase offset difference between the two ensembles, as accounted for by the term $\exp[i(\theta_R - \theta_L)]$.

Figure 4-4(a) plots the maximum fidelity versus $\eta_L$ and $\eta_R$ for the PNRD case. Here, we assume all other parameters are the same for both ensembles. We see that the maximum fidelity degrades in response to decreasing either $\eta_L$ or $\eta_R$. Path loss affects fidelity in a PNRD system when multiple-excitation events are possible because loss allows multiple-photons events to masquerade as single-photon events, which can erroneously herald for success. Therefore, when there is no path loss in a PNRD system its fidelity is unity.

The degradation in the fidelity of entanglement arising from path-loss asymmetry, from (4.31), is shown in Fig. 4-4(b) to be increasingly severe as either $\eta_L$ or $\eta_R$ tends to zero. In this extreme case, we have almost complete which-path information on a photon detection; hence, noting that $F_j = |\langle\psi_j|\psi_j\rangle_{\rm max}|^2 F_{j,\rm max}$, the fidelity becomes approximately 1/2. The asymptote is slightly less than 1/2, owing to multiple-excitation errors. Greater tolerance

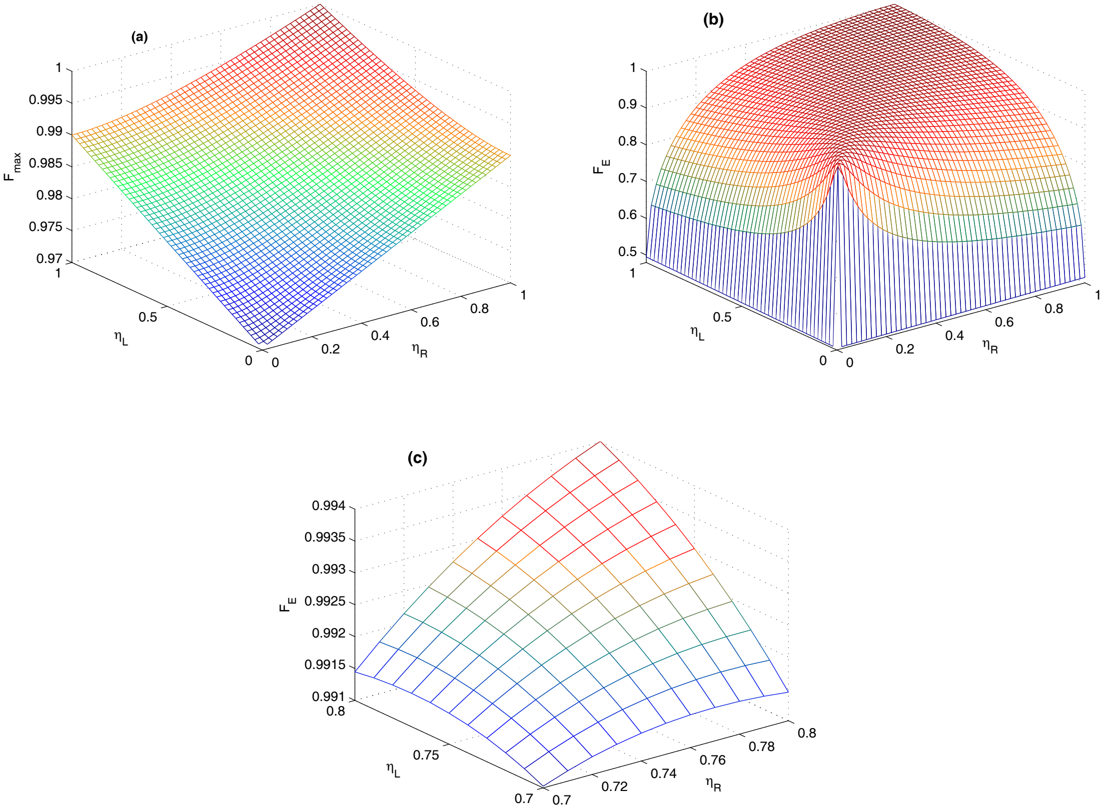

Figure 4-4: (a) Maximum fidelity, $F_{\max} \equiv F_{1,\max} = F_{2,\max}$, for a DLCZ system with asymmetric path loss. In this case, the fidelity-maximizing state is partially entangled. (b) and (c) Fidelity of entanglement (for a singlet/triplet state) versus left-path and right-path efficiencies, for DLCZ entanglement distribution. In all plots the only system asymmetry is $\eta_L \neq \eta_R$, and $p_c = 0.01$, $\eta_1 = \eta_2 = 1$ are assumed.

for path-loss asymmetry occurs at high values of $\eta_L$ and $\eta_R$, with asymmetry sometimes increasing the fidelity. Figure 4-4(c) shows this effect in the vicinity of $\eta_L = \eta_R = 0.7$: for $\eta_R = 0.7$ the peak fidelity occurs at $\eta_L \approx 0.78$. This is due to the fact that the projection $|\langle\psi_j|\psi_j\rangle_{\text{max}}|$ is still very close to one for $\{\eta_L = 0.78, \eta_R = 0.7\}$, and that the value of $F_{j,\text{max}}$ evaluated at $\{\eta_L = 0.78, \eta_R = 0.7\}$ is higher than its value for $\eta_L = \eta_R = 0.7$. On the other hand, fidelity always decreases if we degrade the system efficiency in either path.

Now let us examine the effect of phase asymmetry in the absence of any other sources of asymmetry. Equation (4.31) assumes that $\theta_L$ and $\theta_R$ are deterministic phase shifts. Although systematic (deterministic) phase shifts may be present in a real system, it is more important to study the effects of random phase errors. Presuming $\theta_L$ and $\theta_R$ to be independent, identically distributed, zero-mean, Gaussian random variables with common variance $\sigma_\theta^2$, we obtain

$$F_E = F_{E,\text{sym}}[1 + \exp(-\sigma_\theta^2)]/2\,, \tag{4.36}$$

by averaging (4.31) over these phase-offset statistics. It follows that $\sigma_\theta^2 \ll 1$ is a necessary condition for achieving high fidelity of entanglement in the DLCZ protocol.

## 4.2 MIT-NU versus DLCZ entanglement distribution

Using (4.32) and (4.33) for the DLCZ protocol, and (3.1) and (3.2) for the MIT-NU architecture, let us compare the behaviors of the fidelities and throughputs of entanglement for these two systems. The latter, defined to be $RP_{\text{success}}$, where $R$ is the rate at which either protocol is run, presumes that there are arrays of atomic ensembles (for DLCZ entanglement distribution) or trapped-atom quantum memories (for the MIT-NU architecture) that are loaded in succession. In Fig. 4-5(a) we have plotted the fidelities of entanglement versus the total distance $2L_0$ (in km) between the two atomic ensembles (DLCZ) or the two quantum memories (MIT-NU), and in Fig. 4-5(b) we have plotted the associated throughputs. The DLCZ curves assume the following parameter values: zero phase offsets; $p_c = 0.01$ excitation probability; $\eta_L = \eta_R$ corresponding to 0.2 dB/km fiber loss; $\eta_1 = \eta_2 = 0.5$, and $R = 500\,\text{kHz}$. The MIT-NU curves assume: zero pump-phase offsets; $|G|^2 = 0.01$; $\eta_f$ corresponding to 0.2 dB/km fiber loss; $\gamma\gamma_c/\Gamma\Gamma_c = 10^{-0.5}$ (5 dB fixed loss per source-to-memory path); $\Gamma_c/\Gamma = 0.5$; and $R = 500\,\text{kHz}$. [Note that $p_c = 0.01$ for the DLCZ protocol is an equivalent source rate to $|G|^2 = 0.01$ for the MIT-NU architecture.]

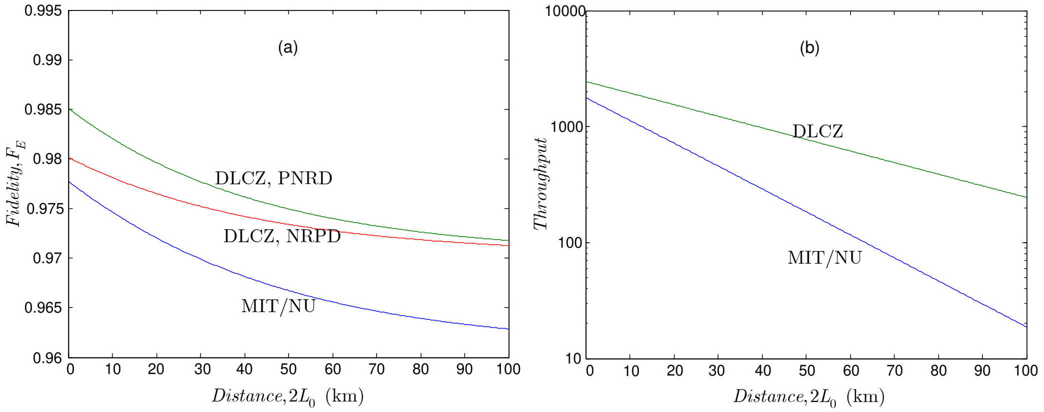

Figure 4-5: Performance comparison of the MIT-NU and DLCZ entanglement-distribution architectures. (a) Fidelity of entanglement versus total distance between quantum memories in km. (b) Throughput (entangled pairs/sec) versus total distance between quantum memories in km. The parameter values assumed in these plots are given in the text.

Figure 4-5(a) shows that the DLCZ protocol has a slight advantage in fidelity of entanglement as compared to the MIT-NU architecture. This advantage, however, may well disappear due to random phase offsets. In particular, if we let $\theta_1$ and $\theta_2$, in the MIT-NU architecture, be independent, identically-distributed, zero-mean Gaussian random variables with common variance $\sigma_\theta^2$, then averaged over this randomness the fidelity of entanglement from (3.2) reduces to

$$F_E = \frac{N^2 + \tilde{n}^2[1 + \exp(-\sigma_\theta^2)]}{4N^2 + 2\tilde{n}^2}, \tag{4.37}$$

which should be compared with (4.36). Superficially, it would seem that both the DLCZ and MIT-NU systems suffer similar phase-offset degradations. However, the MIT-NU architecture needs to stabilize the pump phases for two co-located OPAs, whereas the DLCZ protocol must stabilize the phases at a pair of atomic ensembles that are separated by a long distance ($2L_0$). The latter task will surely be far more difficult than the former.

Figure 4-5(b) shows that the DLCZ protocol has better throughput-versus-distance scaling than does the MIT-NU architecture. This behavior has a simple physical explanation. The DLCZ protocol relies on one Raman photon successfully traversing a distance $L_0$ and being detected, whereas the MIT-NU architecture requires two photons—a signal photon *and* an idler photon—to successfully traverse a distance $L_0$ and be stored. It should be noted, however, that all applications of the DLCZ scheme require two pairs of entangled ensembles [29]. That reduces the effective throughput of the system by a multiplicative factor of 1/2.

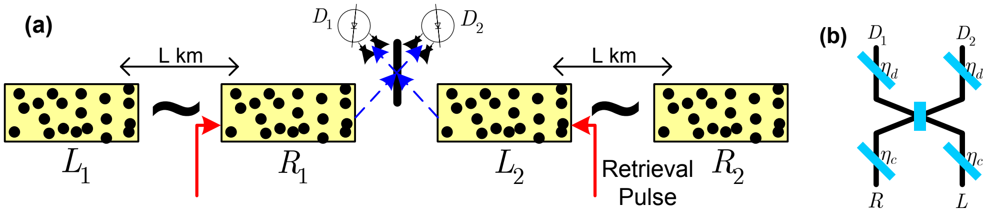

Figure 4-6: (a) DLCZ quantum repeater protocol. $\{L_1, R_1\}$ and $\{L_2, R_2\}$ are singlet states. By pumping $R_1$ and $L_2$ with strong retrieval pulses, we interfere any resulting anti-Stokes photons at a 50/50 beam splitter. Observing one—and only one—photon at one of detectors heralds protocol success, viz. $L_1$ and $R_2$ are now entangled. (b) Notional model for the measurement modules in (a): beam splitters with vacuum-state quantum noise injected through their free input ports account for all loss and inefficiency effects; the single-photon detectors are assumed to have unity quantum efficiencies.

## 4.3 Quantum communication with atomic ensembles

In this section, we study some quantum communication applications of entangled atomic ensembles, as proposed in [29]. Given that the prescription described in Sec. 4.1 provides high fidelity of entanglement ensembles, we will assume that ideal, maximum entanglement has been established between any two ensembles of interest in the quantum communication analyses that follow. We could, instead, start our quantum communication studies from the joint density operator for the post-heralded state—found by accounting for multiple-excitation events by means of Gaussian-state analysis—for each pair of ensembles that has undergone DLCZ entanglement distribution. It can be shown, however, that such an approach is unnecessary so long as the overall quantum communication performance is dominated by other parameters, such as loss in the measurement modules.

### 4.3.1 Quantum repeaters and entanglement swapping

Truly long-distance quantum communication, e.g. for transcontinental applications, will require quantum repeaters to enable entanglement distribution over such extraordinary distances. This can be done by performing entanglement swapping [31] on two pairs of entangled ensembles in the cascade configuration shown in Fig. 4-6(a). Here, ensembles $L_1$ and $R_1$ are entangled and $L$ km away from each other, as are $L_2$ and $R_2$, with $R_1$ and $L_2$ being co-located. Entanglement swapping can be done by performing a Bell-state measurement (BSM) on ensembles $R_1$ and $L_2$. This measurement entangles the $L_1$ and $R_2$ ensembles—separated by $2L$ km—in a Bell state that is determined by the result of the BSM.

To perform a BSM on two atomic ensembles, we use detection of the anti-Stokes photons that can be produced by pumping the $|s\rangle \to |e\rangle$ transitions in the $\{R_1, L_2\}$ ensembles. With strong retrieval pulses we can guarantee the emission of anti-Stokes ($|e\rangle \to |g\rangle$ transition) photons from every ensemble that was in its symmetric collective atomic state. Because these photons will be emitted in well-defined spatial modes, they can be routed to a 50/50 beam splitter—as shown in Fig. 4-6(a)—which is followed by two single-photon detectors (either NRPDs or PNRDs). Full BSM is not possible using only linear optics [21], so the Fig. 4-6(a) measurement scheme can only provide a partial BSM determining only two—out of four—Bell states. Observation of a single click on one, and only one, of the detectors $\{D_1, D_2\}$, heralds completion of the DLCZ quantum-repeater protocol. It is therefore a conditional protocol, whose fidelity and probability of success will be derived in this section.

Without loss of generality, we shall assume that $\{L_1, R_1\}$ and $\{L_2, R_2\}$ have been placed in singlet states, and focus our attention on the losses and detector inefficiencies in the measurement module shown in Fig. 4-6(a). As we did in our treatment of DLCZ entanglement distribution, we shall model the losses and detector inefficiencies by beam splitters, of transmissivities $\eta_c$ and $\eta_d$, that inject vacuum-state quantum noise through their free input ports, and take the detectors to have unity quantum efficiencies, see Fig. 4-6(b). The initial state of all four ensembles is thus

$$|\psi_{in}\rangle = \frac{|1\rangle_{L_1}|0\rangle_{R_1} - |0\rangle_{L_1}|1\rangle_{R_1}}{\sqrt{2}} \otimes \frac{|1\rangle_{L_2}|0\rangle_{R_2} - |0\rangle_{L_2}|1\rangle_{R_2}}{\sqrt{2}}. \tag{4.38}$$

The above state consists of four orthogonal-state terms, each producing an orthogonal state after passing through the linear module of Fig. 4-6(b). To find the heralding and success probabilities of the repeater it therefore suffices to find the corresponding figures of merit for each of these terms. Then, because of symmetry in the measurement module, the repeater fidelity, $F_R$, is just the ratio $P_{\text{success}}/P_{\text{herald}}$. We will use $P_{ij}$ to denote the heralding probability—i.e., having a click on either $D_1$ or $D_2$ but not both—that is due to state $|i\rangle_{R_1}|j\rangle_{L_2}$. Then, defining $\eta_m \equiv \eta_c\eta_d$ to be the measurement efficiency, we have

$$\begin{aligned} P_{\text{herald}} &= (P_{00} + P_{10} + P_{01} + P_{11})/4 \\ &= \begin{cases} \eta_m(2-\eta_m)/2, & \text{PNRD} \\ \eta_m(2-\eta_m/2)/2, & \text{NRPD} \end{cases} \end{aligned} \tag{4.39}$$

and

$$\begin{aligned} P_{\text{success}} &= (P_{01} + P_{10})/4 \\ &= \eta_m/2, \end{aligned} \tag{4.40}$$

where we used

$$P_{00} = 0, \tag{4.41a}$$

$$P_{01} = P_{10} = \eta_m, \tag{4.41b}$$

$$P_{11} = \begin{cases} 2\eta_m(1 - \eta_m), & \text{PNRD} \\ 2\eta_m(1 - \eta_m/2), & \text{NRPD.} \end{cases} \tag{4.41c}$$

The preceding results show that the main source of error in the system is due to $P_{11}$, i.e., when we have two indistinguishable photons at the input of the 50/50 beam splitter. In this case, the $L_1$ and $R_2$ ensembles are in their ground states after the herald occurs, and thus the heralding event does *not* imply a successful entanglement swap. That such an erroneous heralding can occur is due to quantum interference. When a pair of indistinguishable photons enter a 50/50 beam splitter—one through each input port—they undergo quantum interference that makes both exit from the same output port [54]. Now, if we are using NRPDs, these two photons will reach one of the detectors with probability $\eta_m^2$ and erroneously herald for success. Note that a PNRD system can identify this type of error. However, if one—and only one—of the two photons is absorbed en route to the PNRDs, then they too can be fooled into heralding an entanglement swap when no such swap has occurred. This loss event occurs with probability $2(1-\eta_c)\eta_m + 2\eta_c^2\eta_d(1-\eta_d)$ for both NRPD and PNRD systems. The sum of these probabilities results in (4.41c). It follows that the maximum fidelity, achieved at $\eta_m = 1$, of a PNRD-based repeater is unity, whereas for an NRPD-based system it is only 2/3. In general, from (4.39) and (4.40), we obtain

$$\begin{aligned} F_R &= P_{\text{success}}/P_{\text{herald}} \\ &= \begin{cases} 1/(2 - \eta_m), & \text{PNRD} \\ 1/(2 - \eta_m/2), & \text{NRPD.} \end{cases} \end{aligned} \tag{4.42}$$

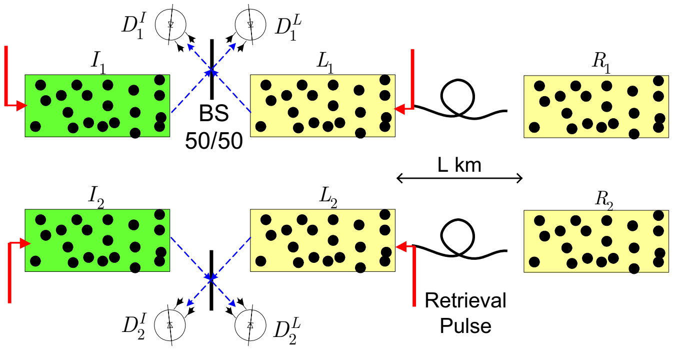

Figure 4-7: DLCZ scheme for conditional teleportation. Two pairs of entangled atomic ensembles $\{L_1, R_1\}$ and $\{L_2, R_2\}$ are used to teleport the quantum state of ensembles $\{I_1, I_2\}$ to ensembles $\{R_1, R_2\}$. Strong retrieval pulses, which are near-resonant with the $|s\rangle \to |e\rangle$ transition, are used to pump ensembles $\{L_1, L_2, I_1, I_2\}$, recovering anti-Stokes photons from every ensemble that was in its symmetric collective atomic state. Detection of a photon by one, and only one, of the single-photon detectors in each measurement module heralds completion of the protocol.

### 4.3.2 DLCZ teleportation

The DLCZ teleportation scheme is a conditional protocol for teleporting a qubit from one pair of atomic ensembles to another, see Fig. 4-7, [29]. It assumes that ensembles $\{L_1, R_1\}$ and $\{L_2, R_2\}$ have each been entangled in singlet states by means of the entanglement distribution protocol described in Sec. 4.1—perhaps augmented by quantum repeaters to achieve even longer distances than can be realized by entanglement distribution alone—where ensembles $\{L_1, L_2\}$ are co-located, as are ensembles $\{R_1, R_2\}$, with the latter pair being a distance $L$ away from the former. The qubit to be teleported is the state

$$|\psi_{\text{in}}\rangle_{I_1 I_2} \equiv d_0|1\rangle_{I_1}|0\rangle_{I_2} + d_1|0\rangle_{I_1}|1\rangle_{I_2}, \quad \text{where } |d_0|^2 + |d_1|^2 = 1, \tag{4.43}$$

stored in two other ensembles, $\{I_1, I_2\}$, which are co-located with $\{L_1, L_2\}$. Such a state can be prepared by using the asymmetric setup as discussed in Sec. 4.1.5. Our objective is to make a measurement that transfers the $\{d_0, d_1\}$ coherence to the remote ensembles $\{R_1, R_2\}$.

To accomplish this teleportation, we need two simultaneous entanglement swaps: a BSM on $L_1$ and $I_1$, and a BSM on $L_2$ and $I_2$. As depicted in Fig. 4-7, the required BSM is performed by the same measurement module used in the DLCZ quantum repeater. Thus, DLCZ teleportation is conditional, hence it can only be used if $\{I_1, I_2\}$ can be restored to the state $|\psi_{\text{in}}\rangle$ when the heralding event fails to occur. In what follows we will sketch a derivation of the fidelity of DLCZ teleportation,

$$F_T \equiv P_+ \ {}_{R_1R_2}\langle\psi^+_{\text{out}}|\hat{\rho}^+_{\text{out}}|\psi^+_{\text{out}}\rangle_{R_1R_2} + P_- \ {}_{R_1R_2}\langle\psi^-_{\text{out}}|\hat{\rho}^-_{\text{out}}|\psi^-_{\text{out}}\rangle_{R_1R_2}, \tag{4.44}$$

where $P_+$ is the probability of heralding on $\{D_1^L, D_2^L\}$ or $\{D_1^I, D_2^I\}$, $P_-$ is the probability of heralding on $\{D_1^L, D_2^I\}$ or $\{D_1^I, D_2^L\}$,

$$|\psi^\pm_{\text{out}}\rangle_{R_1R_2} \equiv d_0|1\rangle_{R_1}|0\rangle_{R_2} \pm d_1|0\rangle_{R_1}|1\rangle_{R_2}, \tag{4.45}$$

are the desired output states for the $\{R_1, R_2\}$ ensembles, and $\hat{\rho}^\pm_{\text{out}}$ are their actual output states, conditioned on there being a $P_\pm$ heralding event.

The initial state of all six ensembles is

$$\begin{aligned} |\psi_{\text{in}}\rangle \equiv \left(d_0\,|1\rangle_{I_1}|0\rangle_{I_2} + d_1\,|0\rangle_{I_1}|1\rangle_{I_2}\right) \quad &\otimes \quad \left(|0\rangle_{L_1}|1\rangle_{R_1} - |1\rangle_{L_1}|0\rangle_{R_1}\right)/\sqrt{2} \\ &\otimes \quad \left(|0\rangle_{L_2}|1\rangle_{R_2} - |1\rangle_{L_2}|0\rangle_{R_2}\right)/\sqrt{2}\,. \end{aligned} \tag{4.46}$$

We can quickly home in on the output state $\hat{\rho}_{\text{out}}$ by multiplying out in (4.46), throwing away all terms that cannot lead to heralding, and then renormalizing. The resulting "short-form" input state is

$$\begin{aligned} |\psi_{\text{in}}\rangle_{\text{short}} \ = \ & -\frac{d_0}{\sqrt{2}}|0\rangle_{L_1}|1\rangle_{I_1}|1\rangle_{L_2}|0\rangle_{I_2}|1\rangle_{R_1}|0\rangle_{R_2} \\ & -\frac{d_1}{\sqrt{2}}|1\rangle_{L_1}|0\rangle_{I_1}|0\rangle_{L_2}|1\rangle_{I_2}|0\rangle_{R_1}|1\rangle_{R_2} \\ & +\frac{d_0}{\sqrt{2}}|1\rangle_{L_1}|1\rangle_{I_1}|1\rangle_{L_2}|0\rangle_{I_2}|0\rangle_{R_1}|0\rangle_{R_2} \\ & +\frac{d_1}{\sqrt{2}}|1\rangle_{L_1}|0\rangle_{I_1}|1\rangle_{L_2}|1\rangle_{I_2}|0\rangle_{R_1}|0\rangle_{R_2}\,. \end{aligned} \tag{4.47}$$

The success or failure of DLCZ teleportation—given that a heralding event has occurred—can be understood by scrutinizing $|\psi_{\text{in}}\rangle_{\text{short}}$. A heralding event generated by the first two terms (the *good* terms) on the right-hand side of (4.47) yields the desired teleportation result, but a heralding event that is due to the last two terms (the *bad* terms) in this equation leaves the $\{R_1, R_2\}$ ensembles in their ground states. Physically, it is easy to see what leads to this behavior. Heralding that is due to the good terms results from exactly two photons being detected: one from ensemble $L_1$ (or $I_1$) in the upper measurement module of Fig. 4-7(a), and one from ensemble $I_2$ (or $L_2$) in the lower measurement module in that figure. The measurement-module beam splitters erase which-way information, and thus teleportation is completed. Now, suppose that we have perfect measurement efficiency ($\eta_m \equiv \eta_c\eta_d = 1$) and consider what happens when the heralding is due to one of the bad terms. In this case three photons enter the measurement modules: either one each from $L_1$ and $I_1$ plus one from $L_2$, or one from $L_1$ and one each from $L_2$ and $I_2$. In either case the $\{R_1, R_2\}$ ensembles are left in their ground states, hence the resulting $\hat{\rho}_{\text{out}}$ will be outside the Hilbert space spanned by $|\psi^{\pm}_{\text{out}}\rangle_{R_1R_2}$. So, whether or not the bad terms degrade DLCZ teleportation fidelity depends on whether the measurement modules can distinguish the good terms in (4.47) from the bad ones.

To evaluate the teleportation fidelity, we can use the heralding probabilities we obtained in Sec. 4.3.1 along with the distinction we have drawn between good and bad terms to obtain

$$F_T = \begin{cases} 1/(3-2\eta_m), & \text{PNRD} \\ 1/(3-\eta_m), & \text{NRPD}, \end{cases} \tag{4.48}$$

where we used

$$P_{\text{success}} = P_{01}P_{10}/4 = \eta_m^2/4 \tag{4.49}$$

and

$$\begin{aligned} P_{\text{herald}} &= (P_{01}P_{10} + P_{11}P_{01})/4 \\ &= \begin{cases} \eta_m^2(3-2\eta_m)/4, & \text{PNRD} \\ \eta_m^2(3-\eta_m)/4, & \text{NRPD}. \end{cases} \end{aligned} \tag{4.50}$$

It follows that with perfect measurement efficiencies, the teleportation fidelity of the PNRD-based system is $F_T = 1$ and that of the NRPD-based system is $F_T = 1/2$. In Fig. 4-8 we have plotted $F_T$ versus $\eta_m$ for the PNRD and NRPD cases. The NRPD system never attains high fidelity because of its inability to suppress heralding from the bad terms in $|\psi_{\text{in}}\rangle_{\text{short}}$. The PNRD does realize high teleportation fidelity, but only when its measurement efficiency is similarly high.

DLCZ teleportation is rather different from MIT-NU teleportation. The DLCZ approach

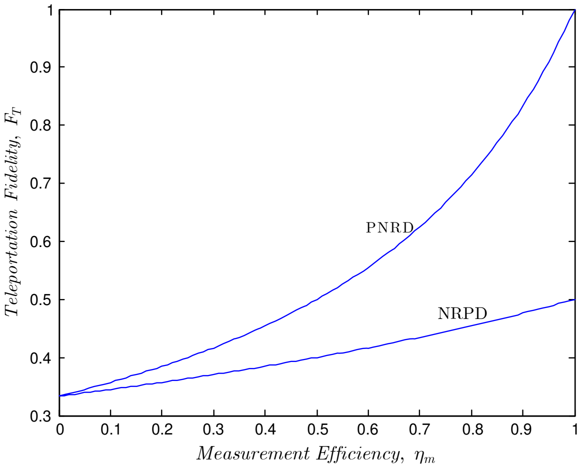

Figure 4-8: Fidelity of DLCZ teleportation, $F_T$, versus measurement efficiency, $\eta_m$.

is conditional, hence it can only be used if the $\{I_1, I_2\}$ ensembles in Fig. 4-7(a) can be restored to the state $|\psi_{\text{in}}\rangle$ when the heralding event fails to occur. The MIT-NU approach is unconditional, and there seems to be no fundamental problems in achieving a close-to-unity fidelity. On the other hand, the measurements required by the DLCZ scheme—high measurement-efficiency PNRD modules—seem significantly less challenging, given the current state of technology, than what is needed by the MIT-NU system, viz. BSMs on trapped atoms.

# Chapter 5

# Continuous-time Cross-phase Modulation and Quantum Computation

Despite all the interest in developing an atomic quantum memory suitable for quantum computation [30, 29, 8, 9], none has succeeded in providing such a basic computational unit. The trapped-atom approach is far more demanding than can be implemented on a large scale. Atomic-ensemble memories are still plagued with short coherence times, and they are not the best candidates for two-qubit operations. Trapped ions are the most promising atomic-memory technology, but it has been difficult to couple a single photon to a single ion in free space. These challenges keep the optics-based approaches to quantum computation, which enjoy the well-developed technology of photonics, still promising and attractive. Photons can carry quantum information either in the form of polarization or number of excitations. Using beam splitters, phase shifters, and wave plates it is possible to generate entangled states, to perform interferometric measurements, and to apply single-qubit rotations. To complete a universal gate set for quantum computation, all that is then needed is an appropriate two-qubit quantum gate such as a controlled-NOT (CNOT) gate. For quantum communication purposes, it is also crucial to build a full Bell-state measurement (BSM) device. These are major obstacles facing optics-based solutions to quantum computing, because the interaction between two single photons is generally quite weak.

There are several proposals for realizing an optical CNOT gate. In one approach, we postpone the interaction between two photons until the very end, when a measurement provides us with the required coupling [55, 56]. To achieve high fidelities, these approaches either require highly efficient (number-resolving) photodetectors, and/or their desired operations are conditional on observing certain measurement outcomes. It is also possible to use hyperentangled photons—where each single photon is entangled in two degrees of freedom—to implement a CNOT gate [57]. The hyperentanglement approach, however, is not scalable, hence it is only useful for few-qubit applications. There is another method, proposed by Chuang and Yamamoto [58], which relies on a strong nonlinear interaction between two single photons via a Kerr medium. They proposed to use this Kerr interaction to construct a quantum phase gate from which a CNOT gate can be realized. With recent advances in cavity QED [59], photonic crystals [60], as well as hollow fibers [61], it may be possible to provide the very strong nonlinearity demanded by these gates, however, their fidelity of operation needs to be scrutinized. A recent work by J. H. Shapiro [35], which employs a continuous-time field-operator approach to modeling the input-output relationship of a Kerr medium, shows that the phase-gate fidelity is at most 2/3.

One last idea for implementing an optics-based CNOT gate, which will be the focus of this chapter, is to use a distributed gate in which a single photon interacts with a bus, which is carrying a strong coherent beam, via a *weak* nonlinear Kerr medium. The bus can interact with other qubits along its way to accomplish a multi-qubit gate. Using this idea, a group of researchers from HP Labs have described a distributed parity gate, and shown how it can be used to implement a deterministic CNOT gate [33]. This parity gate can also be used to realize a full BSM device. Ideal performance of this gate is achieved under a single-mode treatment of cross-phase modulation (XPM). It has been shown, however, that to properly account for the quantum behavior of self-phase modulation (SPM), a continuous-time multimode theory must be employed [62]. In this chapter, we introduce a similar theory for the XPM case [35], assuming that there is no SPM, and we use our new theory to find the fidelity of the parity gate proposed in [33]. The main features of our theory are a non-instantaneous, causal response function for the medium, and a corresponding phase noise that accompanies the output fields. This phase noise is responsible for the degradation of fidelity because its mean-squared strength is proportional to the response function's amplitude.

The rest of this chapter is organized as follows. Section 5.1 describes our model for the Kerr nonlinearity, in which we discuss different regimes of operation. It turns out that in order to observe a significant nonlinearity imparted by a single photon, we need to operate in the slow-response regime, i.e., the temporal pulse shape of the photon should be much shorter than that of the response function. In Section 5.2, we consider a simple gate in which a single-photon pulse induces some phase shift on a coherent-state probe beam. We then describe the parity gate operation and find, for the first time, its fidelity in the ideal case of no loss, no dispersion, and no SPM using our continuous-time multi-mode model.

## 5.1 Continuous-time cross-phase modulation

In this section, we describe the continuous-mode model for XPM, first introduced in [35]. This model applies to the Kerr interactions that occur in a length of a macroscopic material, e.g. an optical fiber. Hence, input and output fields are best modeled by traveling waves. Whereas discrete modes are used to model the light confined in a cavity, for a traveling beam, or, equivalently, when the length of the cavity tends to infinity, it is more appropriate to employ a continuous-time formalism [38]. In this formalism, we associate with each frequency $\omega$ an annihilation operator $\hat{a}(\omega)$ for which we have

$$[\hat{a}(\omega), \hat{a}^\dagger(\omega')] = \delta(\omega - \omega'). \tag{5.1}$$

The positive-frequency field operator associated with a $+z$-going plane-wave electric field, in a well-defined polarization, can then be written as follows [38]

$$\hat{E}(z,t) = i \int d\omega \sqrt{\frac{\hbar\omega}{4\pi\epsilon_0 c A}} \hat{a}(\omega) e^{-i\omega(t - z/c)}, \tag{5.2}$$

where $A$ is a finite cross-sectional area of interest. The limits of integration in (5.2) are from 0 to $\infty$. However, assuming that our optical source is narrowband, with central frequency $\omega_0$, we can extend the integral's limits to run from $-\infty$ to $+\infty$. Moreover, we can normalize $\hat{E}(z,t)$ by $i\sqrt{\hbar\omega_0/(2\epsilon_0 c A)}$ to obtain a photon-units positive-frequency field operator

$$\hat{E}(t) = \int \frac{d\omega}{\sqrt{2\pi}} \hat{a}(\omega) e^{-i\omega t}, \tag{5.3}$$

where we have replaced $t - z/c$ with $t$. For any constant value of $z$, using the narrowband-source assumption, there exist an extra phase factor $\exp(i\omega_0 z/c)$, which will be taken into

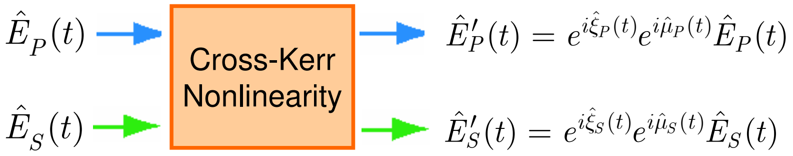

Figure 5-1: Modeling the cross-Kerr nonlinearity using input-output field operators. Here, $\hat{\xi}_S$ and $\hat{\xi}_P$ represent phase noise operators, and $\hat{\mu}_{S/P}$ is a function of the probe/signal beam's flux operator as well as the medium's response function.

account when needed. $\hat{E}(t)$ is the inverse Fourier transform of $\hat{a}(\omega)$, and therefore, using (5.1), it can be seen that it has the following commutator with its adjoint

$$[\hat{E}(t), \hat{E}^\dagger(t')] = \delta(t - t'). \tag{5.4}$$

For our later calculations it will be useful to write our field operators in terms of a discrete set of basis functions:

$$\hat{E}(t) = \sum_i \phi_i(t) \hat{a}_i, \tag{5.5}$$

where $\{\phi_i\}$ is a complete orthonormal set of functions satisfying

$$\int dt \phi_i(t) \phi_j^*(t) = \delta_{ij}, \tag{5.6}$$

$$\sum_i \phi_i^*(t) \phi_i(t') = \delta(t - t'), \tag{5.7}$$

and $\hat{a}_i = \int dt \phi_i^*(t) \hat{E}(t)$ is a discrete-mode annihilation operator, which satisfies $[\hat{a}_i, \hat{a}_j^\dagger] = \delta_{ij}$. Equation (5.5) provides us with a prescription for converting a continuous-time field operator to a sum of discrete-mode operators, where each mode has a pulse shape orthogonal to that of the other modes. We will use this formalism frequently in forthcoming sections.

Now, let us begin consideration of the Kerr medium. We will assume that there is no loss, no dispersion, and no SPM in this medium. Furthermore, we denote the input field operators by $\hat{E}_S(t)$ for the signal beam and $\hat{E}_P(t)$ for the probe beam, whose respective output field operators are $\hat{E}'_S(t)$ and $\hat{E}'_P(t)$; see Fig. 5-1. Then, the input-output relationship for this material is as follows [35]:

$$\hat{E}'_K(t) = e^{i\hat{\xi}_K(t)} e^{i\hat{\mu}_K(t)} \hat{E}_K(t), \quad K = S, P, \tag{5.8}$$

where we have suppressed the group delay, and

$$\begin{aligned}\hat{\mu}_S(t) &\equiv \kappa \textstyle\int d\tau h(t-\tau)\hat{E}_P^\dagger(\tau)\hat{E}_P(\tau)\\ \hat{\mu}_P(t) &\equiv \kappa \textstyle\int d\tau h(t-\tau)\hat{E}_S^\dagger(\tau)\hat{E}_S(\tau)\end{aligned} \tag{5.9}$$

give the XPM phase shifts on the signal and the probe beams, respectively. $\kappa$ is the XPM coupling coefficient, and $h(t)$ is a causal response function, which has been normalized to satisfy $\int dth(t) = 1$. Equation (5.9) is in accord with our semiclassical understanding of the Kerr effect, in which we assume that the nonlinear operators responsible for the Kerr effect are proportional to the photon-flux operators. However, in order to make the theory self-consistent and to preserve the following output commutation relations

$$\begin{gathered}[\hat{E}'_J(t), \hat{E}'_K(t')] = 0, \quad J, K = S, P,\\ [\hat{E}'_S(t), \hat{E}'^\dagger_P(t')] = 0,\\ [\hat{E}'_K(t), \hat{E}'^\dagger_K(t')] = \delta(t-t'), \quad K = S, P,\end{gathered} \tag{5.10}$$

we need to consider two Langevin noise operators. These noise operators stand for the coupling of the traveling light to the localized oscillators that typically represent the molecular vibrations in the medium, and result in Hermitian phase-noise operators $\hat{\xi}_S(t)$ and $\hat{\xi}_P(t)$. The coupling coefficient between the light and the corresponding reservoir mode at frequency $\omega$ turns out to be proportional to $\sqrt{H_i(\omega)}$, where

$$H_i(\omega) = \int dt\, h(t)\sin(\omega t) \tag{5.11}$$

should be non-negative for $\omega \geq 0$, so that all the damping coefficients are positive. Furthermore, (5.10) requires that [35]

$$[\hat{\xi}_S(t), \hat{\xi}_P(u)] = i\kappa[h(u-t) - h(t-u)]. \tag{5.12}$$

In thermal equilibrium, $\hat{\xi}_S(t)$ and $\hat{\xi}_P(t)$ can be taken to be in zero-mean joint Gaussian states with the following symmetrized correlation function

$$\langle \hat{\xi}_K(t)\hat{\xi}_K(u) + \hat{\xi}_K(u)\hat{\xi}_K(t)\rangle = \kappa \int \frac{d\omega}{\pi} H_i(\omega)\coth[\hbar\omega/(2k_B T)]\cos[\omega(t-u)], \quad K = S, P, \tag{5.13}$$

where $T$ is the absolute temperature in Kelvin.

The above model for XPM raises several questions. First of all, why do we need a non-instantaneous response function? What happens if we assume $h(t) \to \delta(t)$? Secondly, why is the phase-noise variance nonzero even if $T \to 0$? Finally, how strong is the nonlinearity imparted by a single photon? In the next subsections, we provide answers to the above questions.

### 5.1.1 Instantaneous response function

When two classical fields co-propagate through a cross-Kerr effect medium, each induces a nonzero phase shift on the other that is proportional to the inducing field's strength. To understand this classical behavior in the context of the quantum theory for XPM suppose that

$$h(t) = \begin{cases} 1/\Delta, & 0 < t < \Delta, \\ 0, & otherwise, \end{cases} \tag{5.14}$$

and assume that the input fields are in coherent states $|E_S(t)\rangle$ and $|E_P(t)\rangle$, for which $\hat{E}_K(t)|E_K(t)\rangle \equiv E_K(t)|E_K(t)\rangle$ and $|E_K(t)|^2 < \infty$, for $K = S, P$. The phase noise term in (5.8) is not affected by the input pulses, but we expect that an XPM signature from the input signal beam should appear in the $\langle e^{i\hat{\mu}_P(t)}\rangle$ term of the average output probe beam. However, this is not the case for an instantaneous response function as shown below

$$\begin{aligned} \langle e^{i\hat{\mu}_P(t)}\rangle &= \exp\left[\int d\tau |E_S(\tau)|^2 (e^{i\kappa h(t-\tau)} - 1)\right] \\ &= \exp\left[\int_{t-\Delta}^{t} d\tau |E_S(\tau)|^2 (e^{i\kappa/\Delta} - 1)\right] \\ &\to 1, \quad \text{as } \Delta \to 0, \end{aligned} \tag{5.15}$$

where we have used the following formula [38]

$$\exp\left[\int dt g(t)\hat{E}^\dagger(t)\hat{E}(t)\right] = \aleph\left\{\exp\left[\int dt (e^{g(t)} - 1)\hat{E}^\dagger(t)\hat{E}(t)\right]\right\}, \tag{5.16}$$

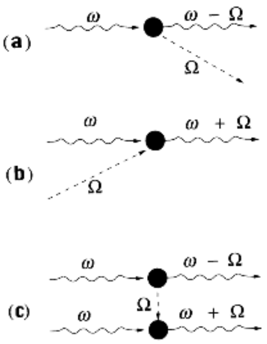

Figure 5-2: Photon-number preserving Feynman diagrams contributing to the phase noise in a Kerr medium. In these figures, dashed lines represent matter excitations with frequencies $\Omega$ close to a resonance of the medium.

where $\aleph\{f(\hat{E}^\dagger, \hat{E})\}$ is the normally-ordered form of operator $f$ in which all creation operators stand to the left of all the annihilation operators. This result is in conflict with experimentally observed data for XPM, and therefore, an instantaneous XPM is not possible. The expected delay for XPM in optical fibers is on the order of 1–10 fs [62].

### 5.1.2 Phase noise at $T = 0\,\mathrm{K}$

If the phase noise is due to molecular vibrations, we may expect that at $T = 0\,K$, there should not be any noise. However, from (5.13), we can see that in this limit we have

$$\langle \hat{\xi}_K^2(t) \rangle = (\kappa/\pi) \int_0^\infty d\omega H_i(\omega) > 0, \quad K = S, P, \tag{5.17}$$

where the inequality follows because the frequency response associated with a real-valued causal impulse response cannot be purely real, and $H_i(\omega) \geq 0$ for $\omega > 0$ is intrinsic to our quantum model for XPM.

The reason for this behavior can better be understood by considering the three photon-number preserving Feynman diagrams, shown in Fig. 5-2, that are responsible for molecular vibrations in our Kerr medium [62]. At high temperatures, all these processes contribute evenly to the phase noise term. At low temperatures, however, the first process is the most significant scattering process, and it gives nonzero noise variances for $\hat{\xi}_S(t)$ and $\hat{\xi}_P(t)$ even at $T = 0\,K$. Nevertheless, we expect that the optimum performance of any XPM-based system will be achieved in this low-temperature limit.

### 5.1.3 Slow versus fast response regimes

An essential figure of merit for the application of Kerr-effect XPM to optics-based quantum computation is the amount of phase shift induced by a single photon. In the field-operator formalism, a single photon in the signal pulse can be represented by the following state

$$|1\rangle_S = \int dt \phi(t) |1_t\rangle_S. \tag{5.18}$$

Here, $|1_t\rangle_S$ is a multi-mode state that represents a single photon at time $t$; it satisfies $\hat{E}_S(t')|1_t\rangle_S = \delta(t-t')|\mathbf{0}\rangle_S$, where $|\mathbf{0}\rangle_S$ is the multi-mode vacuum state for the signal beam. $|\phi(t)|^2$ is the probability of observing this photon at time $t$, and therefore $\int dt|\phi(t)|^2 = 1$. Equivalently, we can use the non-continuous formalism introduced in (5.5). We just need to build up a complete orthonormal basis, for which $\phi_1(t) = \phi(t)$, using well known methods from linear algebra. Given that we have such a basis, $|1\rangle_S$ represents a state for which $\hat{a}_1$ is in the number state $|1\rangle_{a_1}$, and all other operators in (5.5) are in their vacuum states. Now, the average phase shift introduced by this single photon on the probe beam is given by

$$\langle e^{i\hat{\mu}_P(t)} \rangle = \int d\tau |\phi(\tau)|^2 e^{i\kappa h(t-\tau)}, \tag{5.19}$$

where we have again used (5.16).

It is interesting to study the phase-shift behavior in two extreme cases. The first regime, which we call the *fast-response* regime, is for photon pulse shapes whose full-width at half maximum (FWHM), $\tau_0$, is much longer than that of the response function, $\Delta$. In this case, the response function, $h(t)$, behaves like an impulse function that picks a small portion of the pulse shape and produces a phase shift proportional to that part. To clarify this point let's consider an example. Suppose $h(t)$ is given by (5.14) and $\tau_0 \gg \Delta$. Then, from (5.19) and Fig. 5-3(a), we have

$$\begin{aligned} \langle e^{i\hat{\mu}_P(t)} \rangle &\approx 1 - \Delta|\phi(t)|^2 + \Delta e^{i\kappa/\Delta}|\phi(t)|^2 \\ &= 1 - \Delta|\phi(t)|^2(1 - e^{i\kappa/\Delta}) \\ &\approx 1 - i\kappa|\phi(t)|^2, \quad \kappa/\Delta \ll 1 \\ &\approx e^{-i\kappa|\phi(t)|^2}, \quad \kappa|\phi(t)|^2 \ll 1. \end{aligned} \tag{5.20}$$

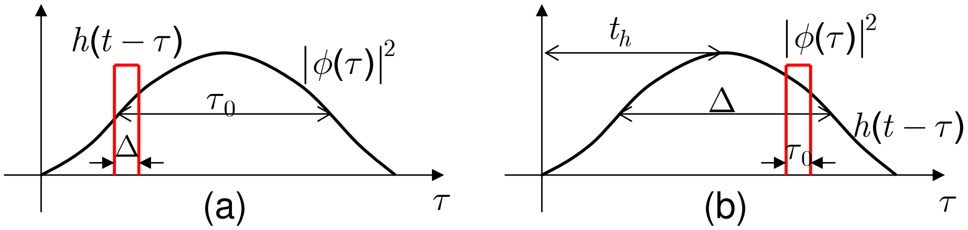

Figure 5-3: A schematic of (a) fast ($\Delta \ll \tau_0$) versus (b) slow ($\Delta \gg \tau_0$) response regimes. In the slow-response regime, we can impose a time separation $t_h$ between the signal and the probe pulses in order to maximize the nonlinear effect.

Now, if the probe pulse has the same duration, $\tau_0$, as the signal pulse, the above result implies that the average phase shift would not be uniformly present over the pulse shape. Even worse, if we consider the point-process picture introduced in [35], we realize that the point in time on the probe pulse that receives the nonzero phase shift is randomly distributed with probability density function $|\phi(t)|^2$. This property of the fast-response regime precludes its being used for any computational purposes.

Let's see how things change when we operate in the *slow-response* regime, i.e., when $\tau_0 \ll \Delta$. In this case, $|\phi(t)|^2$ behaves like $\delta(t-t_0)$, where $t_0$ is the time around which the pulse shape is centered. From (5.19), we then obtain

$$\langle e^{i\hat{\mu}_P(t)} \rangle = e^{i\kappa h(t-t_0)}, \tag{5.21}$$

where we have assumed that $h(t)$ does not change appreciably over a time scale $\tau_0$ [see Fig. 5-3(b)]. Now, if the probe pulse shape is $\phi(t-t')$, then the phase shift induced by our single photon on the probe's pulse is $\kappa h(t')$. We can maximize this phase shift by choosing $t' = t_h$, where $h(t_h) = \max_t[h(t)]$.

Given that $\Delta \approx 1 - 10$ fs for optical fiber, it may seem impractical to work in the slow-response regime in such a medium. However, this is the only regime in which a useful quantum interaction may be seen. Therefore, in our subsequent sections this regime of operation is presumed. If promising results are obtained, it will then behoove us to find a Kerr medium with a more useful response time[1].

---

[1] In the above analysis, we have assumed that there is no SPM in our nonlinear material. It turns out that even if the SPM effect is present in the medium, it can be suppressed by operating in the slow-response regime. This SPM suppression occurs when $h(t_h) \gg h_{\mathrm{SPM}}(0)$, where $h_{\mathrm{SPM}}(t)$ is the SPM response function for the probe beam.

## 5.2 Kerr nonlinearity between a single-photon pulse and a coherent-state pulse

Suppose we have a Kerr medium with XPM coupling constant $\kappa$ and a response function $h(t)$. Moreover, suppose that there is no loss, dispersion, or SPM in this material. We illuminate this medium by two pulses, a signal pulse in a superposition of a vacuum state and a single-photon state with pulse shape $\phi(t+t_h)$, as given below

$$|\psi_{in}\rangle_S = \alpha|\mathbf{0}\rangle_S + \beta\int dt\phi(t+t_h)|1_t\rangle_S, \tag{5.22}$$

where $|\alpha|^2+|\beta|^2=1$, and a probe beam in a coherent field state $|\alpha_P\phi(t)\rangle$. In the mode-decomposition formalism, we can think of the signal pulse as being in the superposition state $|\psi_S\rangle = \alpha|0\rangle_{a_S} + \beta|1\rangle_{a_S}$, where $|n\rangle_{a_S}$ is the Fock state associated with the discrete operator $\hat{a}_S \equiv \int dt\phi^*(t+t_h)\hat{E}_S(t)$. Similarly, the probe beam can be taken to be in a coherent state $|\psi_P\rangle = |\alpha_P\rangle_{a_P}$ associated with the discrete operator $\hat{a}_P \equiv \int dt\phi^*(t)\hat{E}_P(t)$. All other input modes are in their vacuum states. The time shift between the signal and probe pulses results in the signal's inducing the maximum nonlinear phase shift on the probe pulse in the slow-response regime. The goal of this section is to determine the output density operator for this simple gate, which is a building block for the parity gate that will be introduced in the next section.

In order to find the density operator, we pursue the same procedure that we used in the previous chapter by first finding the normally-ordered characteristic function for the output fields. Here, however, the situation is more complicated because we are dealing with continuous-mode operators, and therefore, the parameter $\zeta$ should in general be a continuous function of time. However, for operation within the slow-response regime, it is sufficient to employ the non-continuous picture, characterized by the $\hat{a}_S$ and $\hat{a}_P$ modes, for the input field operators, i.e.,

$$\hat{E}_S(t) = \phi(t+t_h)\hat{a}_S + \text{vacuum-state modes} \tag{5.23}$$

$$\hat{E}_P(t) = \phi(t)\hat{a}_P + \text{vacuum-state modes} \tag{5.24}$$

because the slow-response condition ensures that the output field operators will then obey

$$\hat{E}'_S(t) = \phi(t+t_h)e^{i\hat{\xi}_S(-t_h)}e^{i\hat{\mu}_S(-t_h)}\hat{a}_S + \text{vacuum-state modes} \tag{5.25}$$

$$\hat{E}'_P(t) = \phi(t)e^{i\hat{\xi}_P(0)}e^{i\hat{\mu}_P(0)}\hat{a}_P + \text{vacuum-state modes.} \tag{5.26}$$

The joint normally-ordered characteristic functional for the output field operators $\hat{E}'_S(t)$ and $\hat{E}'_P(t)$ is

$$\chi_N(\zeta_S(t),\zeta_P(t)) \equiv \left\langle e^{\int dt\zeta_S(t)\hat{E}'^{\dagger}_S(t)}e^{\int dt\zeta_P(t)\hat{E}'^{\dagger}_P(t)}e^{-\int dt\zeta^*_P(t)\hat{E}'_P(t)}e^{-\int dt\zeta^*_S(t)\hat{E}'_S(t)}\right\rangle. \tag{5.27}$$

However, if $\int dt\zeta^*_S(t)\phi(t+t_h) = 0$ or $\int dt\zeta^*_P(t)\phi(t) = 0$, then we are averaging over the vacuum modes, whose normally-ordered characteristic function is unity. Hence, the only parameters for which the value of $\chi_N(\zeta_S(t),\zeta_P(t))$ is nontrivial are $\zeta_S(t) = \zeta_S\phi(t+t_h)$ and $\zeta_P(t) = \zeta_P\phi(t)$. An equivalent characteristic function to (5.27) can then be obtained using discrete-mode operators

$$\hat{a}'_S \equiv e^{i\hat{\xi}_S(-t_h)}e^{i\hat{\mu}_S(-t_h)}\hat{a}_S \tag{5.28}$$

$$\hat{a}'_P \equiv e^{i\hat{\xi}_P(0)}e^{i\hat{\mu}_P(0)}\hat{a}_P, \tag{5.29}$$

where

$$\begin{aligned}\hat{\mu}_S(-t_h) &= \kappa\int d\tau h(-t_h-\tau)\hat{E}^{\dagger}_P(\tau)\hat{E}_P(\tau)\\ &\approx \kappa h(-t_h)\int d\tau\hat{E}^{\dagger}_P(\tau)\hat{E}_P(\tau)\\ &= \kappa h(-t_h)\hat{a}^{\dagger}_P\hat{a}_P = 0,\end{aligned} \tag{5.30}$$

and similarly,

$$\hat{\mu}_P(0) \approx \theta\hat{a}^{\dagger}_S\hat{a}_S, \quad \text{where } \theta \equiv \kappa h(t_h), \tag{5.31}$$

where, in both (5.30) and (5.31), we have omitted number-operator terms for modes that are in their vacuum states. Equation (5.30) reflects the fact that the probe beam does not phase shift the signal pulse, because it lags the signal pulse in time and the cross-Kerr effect is causal. On the other hand, the signal pulse induces a phase shift $\theta$ on the probe beam, as shown in (5.31). Our new characteristic function will then read

$$\chi_N(\zeta_S, \zeta_P) \equiv \langle \hat{L}'_S \hat{L}'_P \hat{L}_P \hat{L}_S \rangle, \tag{5.32}$$

where

$$\hat{L}_S \equiv e^{-\zeta_S^* \hat{a}'_S} = e^{-\zeta_S^* \exp[i\hat{\xi}_S(-t_h)]\hat{a}_S}, \tag{5.33}$$

$$\hat{L}'_S \equiv e^{\zeta_S \hat{a}'^{\dagger}_S} = e^{\zeta_S \hat{a}^{\dagger}_S \exp[-i\hat{\xi}_S(-t_h)]}, \tag{5.34}$$

$$\hat{L}_P \equiv e^{-\zeta_P^* \hat{a}'_P} = e^{-\zeta_P^* \exp[i\hat{\xi}_P(0)]\exp[i\theta \hat{a}^{\dagger}_S \hat{a}_S]\hat{a}_P}, \tag{5.35}$$

$$\hat{L}'_P \equiv e^{\zeta_P \hat{a}'^{\dagger}_P} = e^{\zeta_P \hat{a}^{\dagger}_P \exp[-i\hat{\xi}_P(0)]\exp[-i\theta \hat{a}^{\dagger}_S \hat{a}_S]}. \tag{5.36}$$

Our strategy for calculating $\chi_N(\zeta_S, \zeta_P)$ is as follows. We first take the average over the initial signal and probe states by finding $\hat{L}_P \hat{L}_S |\psi_S\rangle|\psi_P\rangle$. Then we convert the phase noise operators into classical random variables, which remain intact until we average over them in the next section, when we calculate the fidelity. Finally the output density matrix is obtained by finding the inverse Fourier transform of the characteristic function. Given that $|\psi_S\rangle$ has at most one photon, we have

$$\begin{aligned} \hat{L}_S|\psi_S\rangle &= \left(1 - \zeta_S^* e^{i\hat{\xi}_S(-t_h)}\hat{a}_S\right)\left(\alpha|0\rangle_{a_S} + \beta|1\rangle_{a_S}\right) \\ &= \left(\alpha - \zeta_S^* \beta e^{i\hat{\xi}_S(-t_h)}\right)|0\rangle_{a_S} + \beta|1\rangle_{a_S}, \end{aligned} \tag{5.37}$$

which results in

$$\begin{aligned} \hat{L}_P \hat{L}_S |\psi_P\rangle|\psi_S\rangle &= e^{-\zeta_P^* \exp[i\hat{\xi}_P(0)]\exp[i\theta \hat{a}^{\dagger}_S \hat{a}_S]\hat{a}_P}|\alpha_P\rangle_{a_P} \hat{L}_S|\psi_S\rangle \\ &= e^{-\zeta_P^* \exp[i\hat{\xi}_P(0)]\exp[i\theta \hat{a}^{\dagger}_S \hat{a}_S]\alpha_P}\left[\left(\alpha - \zeta_S^* \beta e^{i\hat{\xi}_S(-t_h)}\right)|0\rangle_{a_S} + \beta|1\rangle_{a_S}\right]|\psi_P\rangle \\ &= e^{-\zeta_P^* \alpha_P \exp[i\hat{\xi}_P(0)]}\left(\alpha - \zeta_S^* \beta e^{i\hat{\xi}_S(-t_h)}\right)|0\rangle_{a_S}|\psi_P\rangle \\ &+ \beta e^{-\zeta_P^* \alpha_P \exp[i\hat{\xi}_P(0)]\exp[i\theta]}|1\rangle_{a_S}|\psi_P\rangle. \end{aligned} \tag{5.38}$$

Similarly, by finding the Hermitian adjoint of the above equation and replacing $\zeta_K$ with

$-\zeta_K$, $K = S, P$, we find

$$\begin{aligned} \langle\psi_P|\langle\psi_S|\hat{L}'_S\hat{L}'_P &= {}_{a_S}\langle 0|\langle\psi_P|\left(\alpha^* + \zeta_S\beta^* e^{-i\hat{\xi}_S(-t_h)}\right) e^{\zeta_P\alpha_P^*\exp[-i\hat{\xi}_P(0)]} \\ &+ {}_{a_S}\langle 1|\langle\psi_P|\beta^* e^{\zeta_P\alpha_P^*\exp[-i\hat{\xi}_P(0)]\exp[-i\theta]}. \end{aligned} \tag{5.39}$$

From the preceding equations, we obtain

$$\begin{aligned} \langle\psi_P|\langle\psi_S|\hat{L}'_S\hat{L}'_P\hat{L}_P\hat{L}_S|\psi_P\rangle|\psi_S\rangle &= |\alpha|^2 e^{-2i\mathrm{Im}\{\alpha_P\zeta_P^*\exp[i\hat{\xi}_P(0)]\}} \\ &- |\zeta_S|^2|\beta|^2 e^{-i\hat{\xi}_S(-t_h)} e^{-2i\mathrm{Im}\{\alpha_P\zeta_P^*\exp[i\hat{\xi}_P(0)]\}} e^{i\hat{\xi}_S(-t_h)} \\ &+ |\beta|^2 e^{-2i\mathrm{Im}\{\alpha_P\zeta_P^*\exp[i\hat{\xi}_P(0)]\exp[i\theta]\}} \\ &+ \alpha\beta^*\zeta_S e^{-i\hat{\xi}_S(-t_h)} e^{-2i\mathrm{Im}\{\alpha_P\zeta_P^*\exp[i\hat{\xi}_P(0)]\}} \\ &- \alpha^*\beta\zeta_S^* e^{-2i\mathrm{Im}\{\alpha_P\zeta_P^*\exp[i\hat{\xi}_P(0)]\}} e^{i\hat{\xi}_S(-t_h)}. \end{aligned} \tag{5.40}$$

Now, using $\hat{A}e^{\hat{B}}\hat{A}^{-1} = \exp(\hat{A}\hat{B}\hat{A}^{-1})$ (see (3.13) in [63]), we have

$$\begin{aligned} e^{-i\hat{\xi}_S(-t_h)} e^{-2i\mathrm{Im}\{\alpha_P\zeta_P^*\exp[i\hat{\xi}_P(0)]\}} e^{i\hat{\xi}_S(-t_h)} &= \exp\left[e^{-i\hat{\xi}_S(-t_h)}(-2i\mathrm{Im}\{\alpha_P\zeta_P^* e^{i\hat{\xi}_P(0)}\}) e^{i\hat{\xi}_S(-t_h)}\right] \\ &= e^{-2i\mathrm{Im}\{\alpha_P\zeta_P^*\exp[i\hat{\xi}_P(0)]\exp[i\theta]\}}, \end{aligned} \tag{5.41}$$

where in the last equality, we used the following well-known formula (see (3.20) in [63])

$$e^{\hat{A}+\hat{B}} = e^{\hat{A}}e^{\hat{B}}e^{-1/2[\hat{A},\hat{B}]} = e^{\hat{B}}e^{\hat{A}}e^{1/2[\hat{A},\hat{B}]}, \quad \text{if } [\hat{A},[\hat{A},\hat{B}]] = [\hat{B},[\hat{A},\hat{B}]] = 0, \tag{5.42}$$

to interchange the order of $e^{-i\hat{\xi}_S(-t_h)}$ and $e^{i\hat{\xi}_P(0)}$. Plugging (5.41) into (5.40), we find

$$\begin{aligned} \chi_N(\zeta_S, \zeta_P) &= |\alpha|^2\langle e^{-2i\mathrm{Im}\{\alpha_P\zeta_P^*\exp[i\hat{\xi}_P(0)]\}}\rangle \\ &+ |\beta|^2(1 - |\zeta_S|^2)\langle e^{-2i\mathrm{Im}\{\alpha_P\zeta_P^*\exp[i\hat{\xi}_P(0)]\exp[i\theta]\}}\rangle \\ &+ \alpha\beta^*\zeta_S\langle e^{-i\hat{\xi}_S(-t_h)} e^{-2i\mathrm{Im}\{\alpha_P\zeta_P^*\exp[i\hat{\xi}_P(0)]\}}\rangle \\ &- \alpha^*\beta\zeta_S^*\langle e^{-2i\mathrm{Im}\{\alpha_P\zeta_P^*\exp[i\hat{\xi}_P(0)]\}} e^{i\hat{\xi}_S(-t_h)}\rangle, \end{aligned} \tag{5.43}$$

where the averaging is taken over the phase-noise terms $\hat{\xi}_S(-t_h)$ and $\hat{\xi}_P(0)$. In order to perform the averaging in (5.43), we will rewrite the phase-noise terms in a normally-ordered form by introducing an annihilation operator $\hat{b}$, whose quadrature components are the Hermitian operators $\hat{b}_1 \equiv \mathrm{Re}\{\hat{b}\} = \hat{\xi}_S(-t_h)/\sqrt{2\theta}$ and $\hat{b}_2 \equiv \mathrm{Im}\{\hat{b}\} = \hat{\xi}_P(0)/\sqrt{2\theta}$. Because $[\hat{\xi}_S(-t_h), \hat{\xi}_P(0)] = i\theta$, we see that $\hat{b}$ satisfies $[\hat{b}, \hat{b}^\dagger] = 1$. Moreover, because $\hat{\xi}_S$ and $\hat{\xi}_P$ are in a thermal state, that will be the case for $\hat{b}$ as well. As a consequence, if $N \equiv \langle \hat{b}^\dagger \hat{b} \rangle$, then

$$\begin{aligned} \sigma^2 &\equiv \langle \hat{\xi}_S^2(-t_h) \rangle = \langle \hat{\xi}_P^2(0) \rangle \\ &= (2N+1)\theta/2 \qquad (5.44) \\ &= \kappa \int \frac{d\omega}{2\pi} H_i(\omega) \coth[\hbar\omega/(2k_B T)]. \qquad (5.45) \end{aligned}$$

In our new formalism, we can replace $\langle f(\hat{b}^\dagger) g(\hat{b}) \rangle$ with $\langle f(\beta^*) g(\beta) \rangle_\beta$, where $\langle \bullet \rangle_\beta$ denotes statistical averaging over $\beta \equiv \beta_1 + i\beta_2$, which is a classical, zero-mean, circular-complex Gaussian random variable with variance $N$. Using this fact along with (5.42), we obtain for arbitrary complex parameters $\lambda$ and $\eta$

$$\begin{aligned} \langle e^{\lambda i \hat{\xi}_S(-t_h)} e^{\eta i \hat{\xi}_P(0)} \rangle &= \langle e^{\lambda'(\hat{b}+\hat{b}^\dagger)} e^{\eta'(\hat{b}-\hat{b}^\dagger)} \rangle, \quad \text{where } \lambda' = \lambda i \sqrt{\theta/2}, \eta' = \eta\sqrt{\theta/2} \\ &= \langle e^{\lambda' \hat{b}^\dagger} e^{\lambda' \hat{b}} e^{\lambda'^2/2} e^{-\eta' \hat{b}^\dagger} e^{\eta' \hat{b}} e^{-\eta'^2/2} \rangle \\ &= \langle e^{(\lambda'-\eta')\hat{b}^\dagger} e^{(\lambda'+\eta')\hat{b}} e^{\lambda'^2/2 - \eta'^2/2 - \lambda'\eta'} \rangle \\ &= \langle e^{(\lambda'-\eta')\beta^*} e^{(\lambda'+\eta')\beta} e^{\lambda'^2/2 - \eta'^2/2 - \lambda'\eta'} \rangle_\beta \\ &= \langle e^{\lambda i \beta_S} e^{\eta i \beta_P} e^{-\lambda^2\theta/4 - \eta^2\theta/4 - \lambda\eta i\theta/2} \rangle_{\beta_S, \beta_P}, \quad \beta_S = \sqrt{2\theta}\beta_1 \, , \, \beta_P = \sqrt{2\theta}\beta_2 \\ &= \langle e^{\lambda i(\beta_S + \gamma_S)} e^{\eta i(\beta_P + \gamma_P)} e^{-\lambda\eta i\theta/2} \rangle_{\beta_S, \beta_P, \gamma_S, \gamma_P} \\ &= e^{-\lambda\eta i\theta/2} \langle e^{\lambda i \xi_S} e^{\eta i \xi_P} \rangle_{\xi_S, \xi_P}, \qquad (5.46) \end{aligned}$$

where $\gamma_S$ and $\gamma_P$ are independent, identically distributed, zero-mean Gaussian random variables with variance $\theta/2$, that are statistically independent of $\beta_S$ and $\beta_P$. In (5.46), $\xi_K \equiv \beta_K + \gamma_K$, for $K = S, P$, are independent, identically distributed, zero-mean Gaussian variables with variance $N\theta + \theta/2 = \sigma^2$. An interesting observation is that for nonzero values of $\lambda$ and $\eta$, there exists a nontrivial phase shift $e^{-\lambda\eta i\theta/2}$ even if the phase noise variance $\sigma^2$ approaches zero. This is a consequence of the non-commuting phase noise operators $\hat{\xi}_S(-t_h)$ and $\hat{\xi}_P(0)$.

The above formula makes it possible to handle the phase-noise averaging in (5.43). In particular, for the first two terms in (5.43) we have

$$
\begin{aligned}
\langle e^{-2i\,\mathrm{Im}\{\gamma\exp[i\hat{\xi}_P(0)]\}}\rangle &= \langle e^{-\gamma\exp[i\hat{\xi}_P(0)]} e^{\gamma^*\exp[-i\hat{\xi}_P(0)]}\rangle \\
&= \sum_{n=0}^{\infty}\frac{(-\gamma)^n}{n!}\sum_{m=0}^{\infty}\frac{(\gamma^*)^m}{m!}\langle e^{(n-m)i\hat{\xi}_P(0)}\rangle \\
&= \sum_{n=0}^{\infty}\frac{(-\gamma)^n}{n!}\sum_{m=0}^{\infty}\frac{(\gamma^*)^m}{m!}\langle e^{(n-m)i\xi_P}\rangle_{\xi_P} \\
&= \langle e^{-2i\,\mathrm{Im}\{\gamma\exp[i\xi_P]\}}\rangle_{\xi_P}, \qquad (5.47)
\end{aligned}
$$

where $\gamma = \alpha_P\zeta_P^*$ for the first term, and $\gamma = \alpha_P\zeta_P^*\exp(i\theta)$ for the second term. Similarly, for the third and the fourth terms in (5.43), we have

$$
\begin{aligned}
\langle e^{-i\hat{\xi}_S(-t_h)} e^{-2i\,\mathrm{Im}\{\gamma\exp[i\hat{\xi}_P(0)]\}}\rangle &= \sum_{n=0}^{\infty}\frac{(-\gamma)^n}{n!}\sum_{m=0}^{\infty}\frac{(\gamma^*)^m}{m!}\langle e^{-i\hat{\xi}_S(-t_h)} e^{(n-m)i\hat{\xi}_P(0)}\rangle \\
&= \sum_{n=0}^{\infty}\frac{(-\gamma)^n}{n!}\sum_{m=0}^{\infty}\frac{(\gamma^*)^m}{m!}\langle e^{-i\xi_S} e^{(n-m)i\xi_P} e^{(n-m)i\theta/2}\rangle_{\xi_S,\xi_P} \\
&= \langle e^{-i\xi_S} e^{-2i\,\mathrm{Im}\{\gamma\exp[i(\xi_P+\theta/2)]\}}\rangle_{\xi_S,\xi_P}, \qquad (5.48)
\end{aligned}
$$

and

$$
\begin{aligned}
\langle e^{-2i\,\mathrm{Im}\{\gamma\exp[i\hat{\xi}_P(0)]\}} e^{i\hat{\xi}_S(-t_h)}\rangle &= \langle e^{i\hat{\xi}_S(-t_h)} e^{-2i\,\mathrm{Im}\{\gamma\exp[i(\hat{\xi}_P(0)+\theta)]\}}\rangle \\
&= \langle e^{-2i\,\mathrm{Im}\{\gamma\exp[i(\xi_P+\theta/2)]\}} e^{i\xi_S}\rangle_{\xi_S,\xi_P}, \qquad (5.49)
\end{aligned}
$$

where $\gamma = \alpha_P\zeta_P^*$ in both cases. Then, it is easy to verify that the following density matrix corresponds to the characteristic function $\chi_N(\zeta_S,\zeta_P)$

$$
\begin{aligned}
\hat{\rho}_{SP}(\alpha,\beta) &= \langle\, |\alpha|^2 |0\rangle_{a'_S}\langle 0| \otimes |\alpha_P e^{i\xi_P}\rangle_{a'_P}\langle \alpha_P e^{i\xi_P}| \\
&+ |\beta|^2 |1\rangle_{a'_S}\langle 1| \otimes |\alpha_P e^{i(\xi_P+\theta)}\rangle_{a'_P}\langle \alpha_P e^{i(\xi_P+\theta)}| \\
&+ \alpha^*\beta e^{i\xi_S} |1\rangle_{a'_S}\langle 0| \otimes |\alpha_P e^{i(\xi_P+\theta/2)}\rangle_{a'_P}\langle \alpha_P e^{i(\xi_P+\theta/2)}| \\
&+ \alpha\beta^* e^{-i\xi_S} |0\rangle_{a'_S}\langle 1| \otimes |\alpha_P e^{i(\xi_P+\theta/2)}\rangle_{a'_P}\langle \alpha_P e^{i(\xi_P+\theta/2)}|\,\rangle_{\xi_S,\xi_P}. \qquad (5.50)
\end{aligned}
$$

The final averaging over the classical variables will be applied later, when we calculate the fidelity of the parity gate. It is interesting, however, to note that the density matrix predicted by a single-mode treatment of the XPM is not identical to the above density matrix

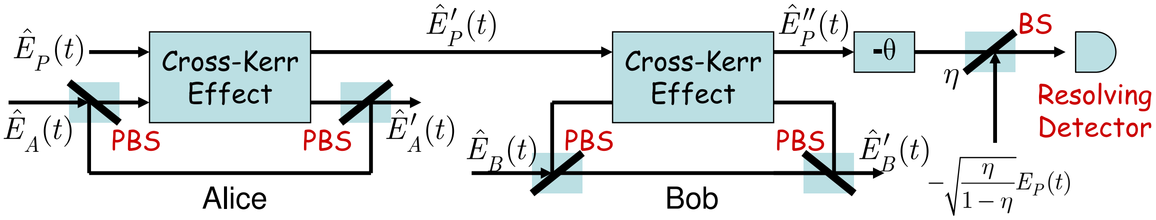

Figure 5-4: An optics-based distributed parity gate that uses a weak cross-Kerr nonlinearity. Alice and Bob encode their qubits (single photons) in horizontal and vertical polarization modes. The polarizing beam splitters (PBS) guide the Alice's horizontal beam and Bob's vertical beam to a Kerr medium in which they interact with a coherent-state probe beam. As a result of this interaction, they may induce a phase shift $\theta$ on the probe beam. The $-\theta$ phase shifter deterministically changes the probe's phase, and the final beam splitter (BS), with near-unity transmissivity $\eta$, models a displacement operator that we need before performing a photon-number resolving measurement.

calculated at $\xi_S = \xi_P = 0$, i.e., zero-variance phase noise terms. Whereas the first two terms in (5.50) also appear in the density matrix associated with a single-mode treatment, this is not the case for the last two terms. The reason for this difference is the extra phase term that appeared in (5.46) because of the non-commuting phase noise operators for the signal and the probe beam.

## 5.3 Parity-gate fidelity analysis

Using the interaction between a single-photon pulse and a coherent-state pulse, described in the previous section, a group of researchers in HP labs have devised a distributed parity gate, from which a CNOT gate can be realized [33]. A parity gate accepts two input qubits, let's say in the general form $|\psi_{in}\rangle = \beta_0|11\rangle_{AB} + \beta_1|10\rangle_{AB} + \beta_2|01\rangle_{AB} + \beta_3|00\rangle_{AB}$, and it gives us a classical outcome, which heralds whether the output state is the even-parity state $\beta_0|11\rangle_{AB} + \beta_3|00\rangle_{AB}$ or the odd-parity state $\beta_1|10\rangle_{AB} + \beta_2|01\rangle_{AB}$. Figure 5-4 shows the optics-based parity gate, proposed in [33], that uses a weak cross-Kerr nonlinearity. In this scheme, Alice ($A$) and Bob ($B$) encode their qubits in two orthogonal polarization modes of single photons, let's say horizontal ($H$) and vertical ($V$), but only Alice's $H$ mode and Bob's $V$ mode interact with a coherent-state bus mode. A single photon on Alice's $H$ mode will impart a phase shift $\theta$ to the probe beam, as will a single photon on Bob's $V$ mode. Because of the weak nonlinearity, $\theta \ll 1$. However, if we have a strong enough probe beam, it may be possible to distinguish between even and odd parity states.

To better understand how the parity gate operates, let's first consider a single-mode treatment of its operation, as presented in [33]. Suppose that the bus (probe) beam is in a coherent state $|\alpha_P\rangle_P$, and Alice and Bob are initially in the state $\beta_0|HH\rangle_{AB}+\beta_1|HV\rangle_{AB}+\beta_2|VH\rangle_{AB}+\beta_3|VV\rangle_{AB}$. Each of these terms induce a different phase shift on the coherent mode. For instance, if Alice and Bob are in the state $|HV\rangle_{AB}$, that imposes a phase shift $2\theta$ on the probe beam and takes it to $|\alpha_P e^{2i\theta}\rangle_P$. After the phase shift $-\theta$ and a $-\alpha_P$ field displacement provided by injecting an appropriate coherent state at the final (highly transmitting) beam splitter, we end up with the state $|\alpha_P(e^{i\theta}-1)\rangle_P$. Doing a similar calculation for all other input terms, we find that the following output state is present immediately before performing the photodetection:

$$\begin{aligned}
|\psi_{out}\rangle &= (\beta_0|HH\rangle_{AB}+\beta_3|VV\rangle_{AB})|0\rangle_P \\
&+ \beta_1|HV\rangle_{AB}|\alpha_P(e^{i\theta}-1)\rangle_P+\beta_2|VH\rangle_{AB}|\alpha_P(e^{-i\theta}-1)\rangle_P \\
&\approx (\beta_0|HH\rangle_{AB}+\beta_3|VV\rangle_{AB})|0\rangle_P \\
&+ \beta_1|HV\rangle_{AB}|i\theta\alpha_P\rangle_P+\beta_2|VH\rangle_{AB}|-i\theta\alpha_P\rangle_P, \quad \theta \ll 1. \qquad (5.51)
\end{aligned}$$

Suppose that the number-resolving detector has unity quantum efficiency, and that the coherent-state strength is such that $\exp(-\theta^2|\alpha_P|^2) \ll 1$. Then, if our detector's output is zero counts, we will assume that Alice and Bob are in the even-parity state

$$|\psi_0\rangle_{AB} = \frac{\beta_0|HH\rangle_{AB}+\beta_3|VV\rangle_{AB}}{\sqrt{|\beta_0|^2+|\beta_3|^2}} \qquad (5.52)$$

because $|\langle 0|\pm i\theta\alpha_P\rangle|^2 = \exp(-\theta^2|\alpha_P|^2) \ll 1$. If we detect $n \geq 1$ photons, the post-measurement joint state for Alice and Bob is as follows

$$\begin{aligned}
|\psi_n\rangle_{AB} &= \frac{{}_P\langle n|\psi_{out}\rangle}{\sqrt{\mathrm{tr}[{}_P\langle n|\psi_{out}\rangle\langle\psi_{out}|n\rangle_P]}} \\
&= \frac{\beta_1\,{}_P\langle n|i\theta\alpha_P\rangle_P|HV\rangle_{AB}+\beta_2\,{}_P\langle n|-i\theta\alpha_P\rangle_P|VH\rangle_{AB}}{\sqrt{\mathrm{tr}[{}_P\langle n|\psi_{out}\rangle\langle\psi_{out}|n\rangle_P]}}, \quad \theta \ll 1 \\
&= \frac{\beta_1|HV\rangle_{AB}+(-1)^n\beta_2|VH\rangle_{AB}}{\sqrt{|\beta_1|^2+|\beta_2|^2}}, \quad n \geq 1 \qquad (5.53)
\end{aligned}$$

where we have used ${}_P\langle n|\alpha\rangle_P = \alpha^n e^{-|\alpha|^2/2}/\sqrt{n!}$. When $n$ is an odd integer, we can apply a $\pi$-rad phase shift to make all the $n \geq 1$ observations result in the odd-parity output state

$(\beta_1|HV\rangle_{AB} + \beta_2|VH\rangle_{AB})/\sqrt{|\beta_1|^2 + |\beta_2|^2}$.

As a figure of merit for system performance, we calculate the success probability, i.e., the probability of being in the desired state $|\psi_n\rangle_{AB}$ upon detection of $n$ photons in the probe beam for $n \geq 0$. The total success probability is then given by

$$\begin{aligned} P_{success} &\equiv \sum_{n=0}^{\infty} \overline{|_P\langle n|_{AB}\langle\psi_n|\psi_{out}\rangle|^2} \\ &= P_{even} + P_{odd}, \end{aligned} \tag{5.54}$$

where $\overline{[\bullet]}$ denotes the Bloch-sphere averaging,

$$\begin{aligned} P_{even} &\equiv \overline{|_P\langle 0|_{AB}\langle\psi_0|\psi_{out}\rangle|^2} \\ &= \overline{|\beta_0|^2 + |\beta_3|^2} = 1/2 \end{aligned} \tag{5.55}$$

is the average success probability for the even-parity case, and

$$\begin{aligned} P_{odd} &\equiv \sum_{n=1}^{\infty} \overline{|_P\langle n|_{AB}\langle\psi_n|\psi_{out}\rangle|^2} \\ &= \sum_{n=1}^{\infty} \overline{\left|_{AB}\langle\psi_n|\left(\beta_1 \frac{(i\theta\alpha_P)^n e^{-\theta^2|\alpha_P|^2/2}}{\sqrt{n!}}|HV\rangle_{AB} + \beta_2 \frac{(-i\theta\alpha_P)^n e^{-\theta^2|\alpha_P|^2/2}}{\sqrt{n!}}|VH\rangle_{AB}\right)\right|^2} \\ &= \overline{(|\beta_1|^2 + |\beta_1|^2)} \sum_{n=1}^{\infty} |i\theta\alpha_P|^2 e^{-\theta^2|\alpha_P|^2}/n! \\ &= \frac{1 - e^{-\theta^2|\alpha_P|^2}}{2} \end{aligned} \tag{5.56}$$

is the average success probability for the odd-parity case.

The above single-mode treatment of the cross-Kerr effect implies that by forcing $\theta|\alpha_P| \gg 1$, we can achieve a near-unity success probability. In the opposite limit of $\theta|\alpha_P| \ll 1$, the success probability approaches 1/2, because, in this case, we have no chance of distinguishing between the odd- and even-parity states in $|\psi_{out}\rangle$. The single-mode model, however, does not account for the causality-induced phase noise that we described in our continuous-time theory. To evaluate the fidelity of the parity gate, for the slow-response regime continuous-time theory, we employ the formalism introduced in the previous section. For simplicity, we assume Alice and Bob are in a tensor-product state $|\psi_A\rangle|\psi_B\rangle$, where

$$|\psi_A\rangle = \alpha|0\rangle_A + \beta|1\rangle_A \quad \text{and} \quad |\psi_B\rangle = \alpha'|0\rangle_B + \beta'|1\rangle_B, \tag{5.57}$$

and

$$\begin{aligned} |0\rangle_K &= |\mathbf{0}\rangle_K, \quad K = A, B, \\ |1\rangle_K &= \int dt\phi(t+t_h)|1_t\rangle_K, \quad K = A, B. \end{aligned} \tag{5.58}$$

Here, $|1\rangle_K$, $K = A, B$, represents the qubit that has nonlinear interaction with the probe beam. Hence,

$$\begin{aligned} |0\rangle_A = |V\rangle_A \quad &\text{and} \quad |1\rangle_A = |H\rangle_A \\ |0\rangle_B = |H\rangle_B \quad &\text{and} \quad |1\rangle_B = |V\rangle_B. \end{aligned} \tag{5.59}$$

The probe beam is in the time-shifted coherent state $|\alpha_P\phi(t)\rangle_P$ that receives the maximum nonlinearity from Alice's and Bob's qubits. Then, the output density matrix for Alice, Bob, and the probe can be obtained using the density matrix in (5.50) twice; once for the Alice-probe interaction and once for the Bob-probe interaction. Note that the density matrix for the state associated with field operators $\hat{E}'_A(t)$ and $\hat{E}'_P(t)$ is given exactly by (5.50), by replacing the $S$ subscripts with $A$'s. From that point, the probe beam could possibly be in four different coherent states, given by (5.50), where for each case we can employ (5.50) again to obtain the output density matrix. The final step is to replace $\alpha_P e^{i\gamma}$ with $\alpha_P(e^{i(\gamma-\theta)}-1)$ to incorporate the effects of phase shifter and the displacement operation. The final density operator is then given by the following equation, in which all states correspond to one of the output operators $\hat{a}'_A = \int dt\phi^*(t+t_h)\hat{E}'_A(t)$, $\hat{a}'_B = \int dt\phi^*(t+t_h)\hat{E}'_B(t)$, or $\hat{a}''_P = \int dt\phi^*(t)\hat{E}''_P(t)$:

$$\begin{aligned} \hat{\rho}_{APB}(\alpha,\beta,\alpha',\beta') &= \Big\langle |\alpha|^2|0\rangle_{AA}\langle 0|\hat{\rho}_{PB}^{(00)} + |\beta|^2|1\rangle_{AA}\langle 1|\hat{\rho}_{PB}^{(11)} \\ &+ \alpha^*\beta e^{i\xi_A}|1\rangle_{AA}\langle 0|\hat{\rho}_{PB}^{(10)} + \alpha\beta^* e^{-i\xi_A}|0\rangle_{AA}\langle 1|\hat{\rho}_{PB}^{(01)}\Big\rangle_{\xi_A,\xi_B,\xi_P} \end{aligned} \tag{5.60}$$

where

$$\begin{aligned}
\hat{\rho}_{PB}^{(00)} &= |\alpha'|^2|0\rangle_{BB}\langle 0| \otimes \Big|\alpha_P(e^{i(\xi_P-\theta)}-1)\Big\rangle_{PP}\Big\langle\alpha_P(e^{i(\xi_P-\theta)}-1)\Big| \\
&+ |\beta'|^2|1\rangle_{BB}\langle 1| \otimes \Big|\alpha_P(e^{i\xi_P}-1)\Big\rangle_{PP}\Big\langle\alpha_P(e^{i\xi_P}-1)\Big| \\
&+ \alpha'^*\beta' e^{i\xi_B}|1\rangle_{BB}\langle 0| \otimes \Big|\alpha_P(e^{i(\xi_P-\theta/2)}-1)\Big\rangle_{PP}\Big\langle\alpha_P(e^{i(\xi_P-\theta/2)}-1)\Big| \\
&+ \alpha'\beta'^* e^{-i\xi_B}|0\rangle_{BB}\langle 1| \otimes \Big|\alpha_P(e^{i(\xi_P-\theta/2)}-1)\Big\rangle_{PP}\Big\langle\alpha_P(e^{i(\xi_P-\theta/2)}-1)\Big|, \qquad (5.61)
\end{aligned}$$

$$\begin{aligned}
\hat{\rho}_{PB}^{(11)} &= |\alpha'|^2|0\rangle_{BB}\langle 0| \otimes \Big|\alpha_P(e^{i\xi_P}-1)\Big\rangle_{PP}\Big\langle\alpha_P(e^{i\xi_P}-1)\Big| \\
&+ |\beta'|^2|1\rangle_{BB}\langle 1| \otimes \Big|\alpha_P(e^{i(\xi_P+\theta)}-1)\Big\rangle_{PP}\Big\langle\alpha_P(e^{i(\xi_P+\theta)}-1)\Big| \\
&+ \alpha'^*\beta' e^{i\xi_B}|1\rangle_{BB}\langle 0| \otimes \Big|\alpha_P(e^{i(\xi_P+\theta/2)}-1)\Big\rangle_{PP}\Big\langle\alpha_P(e^{i(\xi_P+\theta/2)}-1)\Big| \\
&+ \alpha'\beta'^* e^{-i\xi_B}|0\rangle_{BB}\langle 1| \otimes \Big|\alpha_P(e^{i(\xi_P+\theta/2)}-1)\Big\rangle_{PP}\Big\langle\alpha_P(e^{i(\xi_P+\theta/2)}-1)\Big|, \qquad (5.62)
\end{aligned}$$

$$\begin{aligned}
\hat{\rho}_{PB}^{(10)} = \hat{\rho}_{PB}^{(01)} &= |\alpha'|^2|0\rangle_{BB}\langle 0| \otimes \Big|\alpha_P(e^{i(\xi_P-\theta/2)}-1)\Big\rangle_{PP}\Big\langle\alpha_P(e^{i(\xi_P-\theta/2)}-1)\Big| \\
&+ |\beta'|^2|1\rangle_{BB}\langle 1| \otimes \Big|\alpha_P(e^{i(\xi_P+\theta/2)}-1)\Big\rangle_{PP}\Big\langle\alpha_P(e^{i(\xi_P+\theta/2)}-1)\Big| \\
&+ \alpha'^*\beta' e^{i\xi_B}|1\rangle_{BB}\langle 0| \otimes \Big|\alpha_P(e^{i\xi_P}-1)\Big\rangle_{PP}\Big\langle\alpha_P(e^{i\xi_P}-1)\Big| \\
&+ \alpha'\beta'^* e^{-i\xi_B}|0\rangle_{BB}\langle 1| \otimes \Big|\alpha_P(e^{i\xi_P}-1)\Big\rangle_{PP}\Big\langle\alpha_P(e^{i\xi_P}-1)\Big|, \qquad (5.63)
\end{aligned}$$

and the above average is taken over the phase noise terms $\xi_A$, $\xi_B$, and $\xi_P$, which are statistically independent zero-mean Gaussian random variables with respective variances $\sigma_A^2 = \sigma_B^2 = \sigma^2$ and $\sigma_P^2 = 2\sigma^2$.

Using the above density matrix we can easily find the heralding probability for detecting $n$ photons in the probe beam:

$$P_n = \mathrm{tr}({}_P\langle n|\hat{\rho}_{APB}|n\rangle_P), \qquad (5.64)$$

as well as the success probability upon detecting $n$ photons in the probe beam:

$$P_n F_n = {}_P\langle n|_{AB}\langle\psi_n|\hat{\rho}_{APB}|\psi_n\rangle_{AB}|n\rangle_P, \qquad (5.65)$$

where, from (5.52) and (5.53), the desired state $|\psi_n\rangle_{AB}$ upon detection of $n$ photons is as follows

$$|\psi_0\rangle_{AB} = \frac{\beta\alpha'|10\rangle_{AB} + \alpha\beta'|01\rangle_{AB}}{\sqrt{|\alpha\beta'|^2 + |\alpha'\beta|^2}} = \frac{\beta\alpha'|HH\rangle_{AB} + \alpha\beta'|VV\rangle_{AB}}{\sqrt{|\alpha\beta'|^2 + |\alpha'\beta|^2}} \tag{5.66}$$

and

$$|\psi_n\rangle_{AB} = \frac{\beta\beta'|11\rangle_{AB} + (-1)^n\alpha\alpha'|00\rangle_{AB}}{\sqrt{|\alpha\alpha'|^2 + |\beta\beta'|^2}} = \frac{\beta\beta'|HV\rangle_{AB} + (-1)^n\alpha\alpha'|VH\rangle_{AB}}{\sqrt{|\alpha\alpha'|^2 + |\beta\beta'|^2}}, \quad n \geq 1. \tag{5.67}$$

$F_n$ denotes the gate fidelity in the event of observing $n$ photons. Using (5.64), the heralding probability is given by

$$\begin{aligned} P_n &= (|\alpha\alpha'|^2 + |\beta\beta'|^2) f_n(\alpha_P, \theta) \\ &+ (|\alpha\beta'|^2 + |\alpha'\beta|^2) f_n(\alpha_P, 0), \end{aligned} \tag{5.68}$$

where

$$\begin{aligned} f_n(\alpha_P, \theta) = f_n(\alpha_P, -\theta) &\equiv \left\langle \left| {}_P\langle n|\alpha_P(e^{i(\xi_P+\theta)} - 1)\rangle_P \right|^2 \right\rangle_{\xi_P} \\ &= \left\langle \frac{|\alpha_P(e^{i(\xi_P+\theta)} - 1)|^{2n}}{n!} e^{-|\alpha_P(e^{i(\xi_P+\theta)}-1)|^2} \right\rangle_{\xi_P} \\ &\approx \left\langle \frac{|\alpha_P(\xi_P + \theta)|^{2n}}{n!} e^{-|\alpha_P(\xi_P+\theta)|^2} \right\rangle_{\xi_P}, \quad \sigma_P + \theta \ll 1, \\ &= \frac{|\alpha_P|^{2n} e^{-\theta^2|\alpha_P|^2/(1+2\sigma_P^2|\alpha_P|^2)}}{n!\sqrt{1 + 2\sigma_P^2|\alpha_P|^2}} \langle Y^{2n}\rangle_Y \end{aligned} \tag{5.69}$$

where $Y$ is a Gaussian random variable with mean $\theta/(1 + 2\sigma_P^2|\alpha_P|^2)$ and variance $\sigma_P^2/(1 + 2\sigma_P^2|\alpha_P|^2)$. Similarly, using (5.65), we obtain

$$P_0F_0 = \frac{|\alpha\beta'|^4 + |\alpha'\beta|^4 + 2|\alpha\beta\alpha'\beta'|^2 e^{-\sigma_P^2/4}}{|\alpha\beta'|^2 + |\alpha'\beta|^2} f_0(\alpha_P, 0) \tag{5.70}$$

$$P_nF_n = \frac{|\alpha\alpha'|^4 + |\beta\beta'|^4}{|\alpha\alpha'|^2 + |\beta\beta'|^2} f_n(\alpha_P, \theta) + (-1)^n e^{-\sigma_P^2/4} \frac{2|\alpha\beta\alpha'\beta'|^2}{|\alpha\alpha'|^2 + |\beta\beta'|^2} f_n(\alpha_P, 0), \quad n \geq 1. \tag{5.71}$$

Now, assuming that the Alice's and Bob's initial states are independent and uniformly distributed over their respective Bloch spheres, the average success probability for the even-parity case is given by

$$\begin{aligned} P_{even} &= \overline{P_0 F_0} \\ &= f_0(\alpha_P, 0)\overline{\left[\frac{|\alpha\beta'|^4+|\alpha'\beta|^4}{|\alpha\beta'|^2+|\alpha'\beta|^2}+\frac{2|\alpha\beta\alpha'\beta'|^2}{|\alpha\beta'|^2+|\alpha'\beta|^2}e^{-\sigma_P^2/4}\right]} \\ &\cong \frac{1}{\sqrt{1+2\sigma_P^2|\alpha_P|^2}}(A+Be^{-\sigma_P^2/4}), \quad \text{when} \quad \sigma_P \ll 1, \end{aligned} \tag{5.72}$$

where

$$A \equiv \overline{\left[\tfrac{|\alpha\beta'|^4+|\alpha'\beta|^4}{|\alpha\beta'|^2+|\alpha'\beta|^2}\right]} \cong 0.432 \tag{5.73}$$

$$B \equiv \overline{\left[\tfrac{2|\alpha\beta\alpha'\beta'|^2}{|\alpha\beta'|^2+|\alpha'\beta|^2}\right]} \cong 0.068, \tag{5.74}$$

and $\overline{[\bullet]}$ denotes Bloch-sphere averaging. Similarly, noting that $\sum_{n=1}^{\infty} f_n(\alpha_P,\theta) = 1 - f_0(\alpha_P,\theta)$ and $\sum_{n=1}^{\infty}(-1)^n f_n(\alpha_P,\theta) = f_0(\sqrt{2}\alpha_P,\theta) - f_0(\alpha_P,\theta)$, the average success probability for the odd-parity case is given by:

$$\begin{aligned} P_{odd} &= \sum_{n=1}^{\infty}\overline{P_n F_n} \\ &= \overline{\left[\frac{|\alpha\alpha'|^4+|\beta\beta'|^4}{|\alpha\alpha'|^2+|\beta\beta'|^2}\right]}\,[1-f_0(\alpha_P,\theta)] \\ &+ e^{-\sigma_P^2/4}\overline{\left[\frac{2|\alpha\beta\alpha'\beta'|^2}{|\alpha\alpha'|^2+|\beta\beta'|^2}\right]}\,\left[f_0(\sqrt{2}\alpha_P,0)-f_0(\alpha_P,0)\right] \\ &\approx A\left[1-\frac{e^{-\theta^2|\alpha_P|^2/(1+2\sigma_P^2|\alpha_P|^2)}}{\sqrt{1+2\sigma_P^2|\alpha_P|^2}}\right] \\ &+ Be^{-\sigma_P^2/4}\left[\frac{1}{\sqrt{1+4\sigma_P^2|\alpha_P|^2}}-\frac{1}{\sqrt{1+2\sigma_P^2|\alpha_P|^2}}\right], \quad \sigma_P+\theta \ll 1. \end{aligned} \tag{5.75}$$

The total success probability of the gate is again given by $P_{success} = P_{even} + P_{odd}$. $P_{success}$ is a measure of how often our gate performs the required task. So, ideally it should be close to one. That occurs when both of its constituents, $P_{even}$ and $P_{odd}$, take their maximum values of 1/2. For $P_{even}$, from (5.72), that ideal condition occurs when $\sigma_P^2|\alpha_P|^2 \ll 1$ and $\sigma_P^2 \ll 1$. This is in contrast to what we obtained in (5.55) using the single-mode model, for which $P_{even}$ is always 1/2. For $P_{odd}$, the second term in (5.75) vanishes for $\sigma_P^2|\alpha_P|^2 \ll 1$ and for $\sigma_P^2|\alpha_P|^2 \gg 1$, and the first term is at its maximum when $\theta^2|\alpha_P|^2 \gg 1$, in which

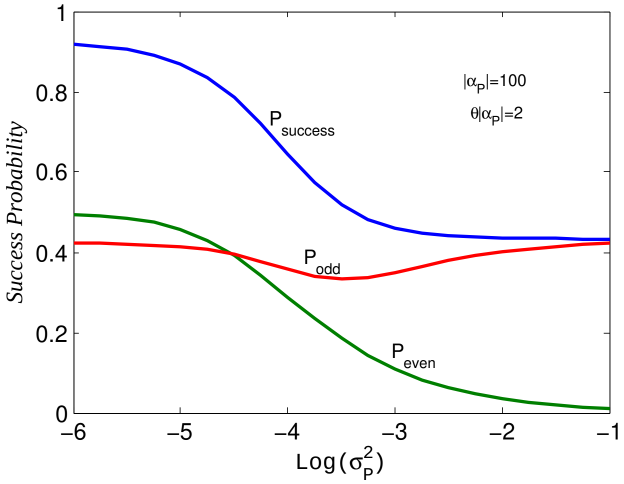

Figure 5-5: Success probability versus phase noise variance for $|\alpha_P| = 100$ and $\theta = 20\,\mathrm{mRad}$.

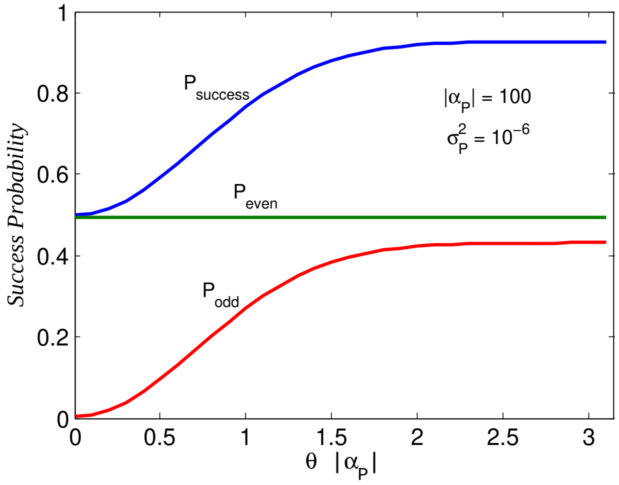

Figure 5-6: Success probability versus $\theta|\alpha_P|$ for $\sigma_P^2 = 10^{-6}$ and $|\alpha_P| = 100$.

case $P_{odd} = A = 0.43$. Again, this is in contrast to what we obtained in (5.56) using the single-mode model, for which $P_{odd}$ approaches 1/2 for $\theta^2|\alpha_P|^2 \gg 1$. The reason for this difference could lie in what we noticed in equations (5.46) and (5.50) regarding the extra phase terms due to the non-commuting nature of phase noise operators. Overall, based on our continuous-time theory for the cross-Kerr effect, it seems that for the optimum performance of the gate we have to satisfy the following three conditions simultaneously:

$$\theta^2|\alpha_P|^2 \gg 1,\ \sigma_P^2|\alpha_P|^2 \ll 1,\ \sigma_P^2 \ll 1. \tag{5.76}$$

In Figs. 5-5–5-7, we have plotted the success probability by varying one of the three

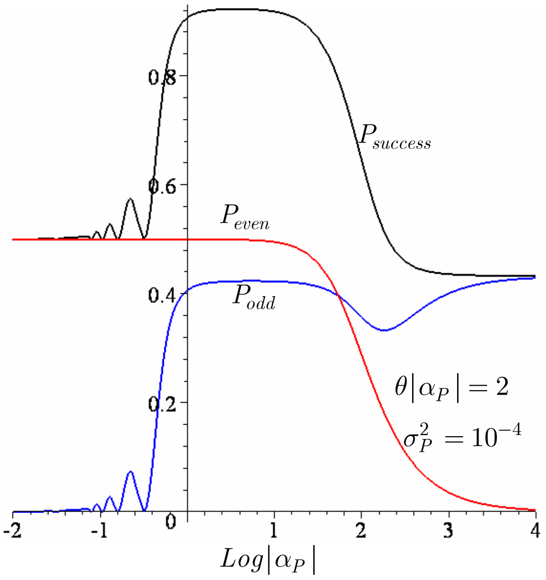

Figure 5-7: Success probability versus the probe parameter $|\alpha_P|$ for $\theta|\alpha_P| = 2$ and $\sigma_P^2 = 10^{-4}$. By fixing $\theta|\alpha_P|$ and changing $|\alpha_P|$, we are implicitly varying the nonlinearity of the material.

variables $\sigma_P^2$, $|\alpha_P|$, and $\theta|\alpha_P|$, with the other two fixed. Here, we have assumed that it is possible to change the phase variance $\sigma_P^2$ without affecting $\theta$, even though both are related to the material response function. Fig 5-5 shows that $P_{even}$ is very sensitive to the phase noise, and it drops significantly if $\sigma_P^2|\alpha_P|^2 > 1$. On the other hand, $P_{odd}$ only drops slightly for moderate values of $\sigma_P^2$, and it achieves its maximum value again for large values of $\sigma_P^2$. Its maximum, however, is bound to the value of $A = 0.43$. In Fig. 5-6, it can be seen that whereas $P_{even}$ is independent of $\theta$, $P_{odd}$ requires $\theta|\alpha_P| > \pi/2$ to achieve a reasonable performance. That justifies the use of $\theta|\alpha_P| = 2$ in the Figs. 5-5, 5-7, and 5-8. Finally, one may be interested in the effect of $|\alpha_P|$, as shown in Fig. 5-7. In the weak nonlinear regime, we need a large value of $|\alpha_P|$ in order to achieve a sufficiently high value of $\theta^2|\alpha_P|^2$. That imposes a large amount of phase noise because the value of $\sigma_P^2|\alpha_P|^2$ also increases. However, if we have a material with a large cross-Kerr coupling constant $\kappa$ and a low phase-noise variance, then we only need a moderate value for $|\alpha_P|$. In the extreme case of $|\alpha_P| \ll 1$, $P_{odd}$ again goes to zero because $f_0(\alpha_P, \theta) \to 1$. In Fig. 5-7, we have calculated $f_0$ numerically because the condition $\sigma_P + \theta \ll 1$ in (5.69) no longer holds when $|\alpha_P| = 2/\theta \ll 1$.

So far, we have assumed that we independently vary $\theta$ and $\sigma_P^2$. This, however, is not the case in our cross-Kerr effect model. Because of (5.44), both $\sigma_P^2$ and $\theta$ are functions of $h(t)$. In order to increase the maximum of $h(t)$ while keeping its area constant, we need to

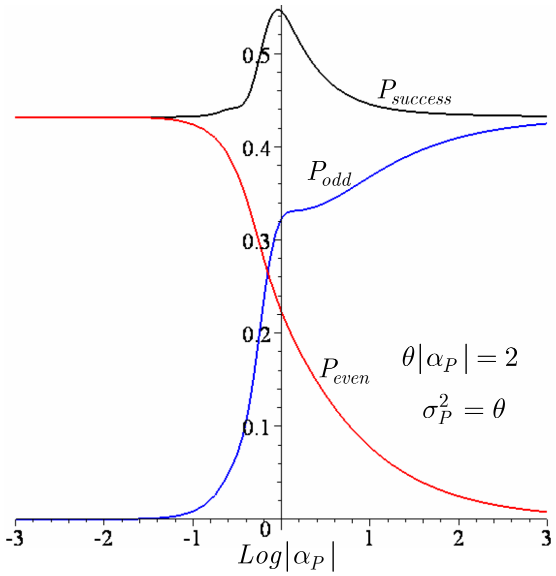

Figure 5-8: Success probability versus the probe parameter $|\alpha_P|$ using the double-pole response function for the medium at $T = 0\,K$ and $\gamma_0 \to 0$.

make it narrower. That however increases the frequency content of $h(t)$, which may increase $\sigma_P^2$. On the other hand, $\sigma_P^2 \propto \kappa$ and $\theta \propto \kappa$. Therefore, in order to satisfy both $\theta^2|\alpha_P|^2 > 1$ and $\sigma_P^2|\alpha_P|^2 \ll 1$ conditions, one needs a high ratio of $\theta^2/\sigma_P^2$, or equivalently, a large value for $\kappa$. This is not a desired behavior for a system that was designed to operate in the weak-nonlinear regime.

To clarify the above points, let's consider a concrete example. Suppose $h(t)$ is the two-pole response function associated with the frequency response

$$H(\omega) = \int dt h(t) e^{i\omega t} = \frac{\Omega_0^2}{\Omega_0^2 - \omega^2 - i\omega\gamma_0}, \tag{5.77}$$

where $\Omega_0$ is the vibrational resonance frequency of the medium and $\gamma_0$ is a damping rate. It has turned out [35] that the best performance is achieved in the underdamped single resonance regime $0 < \gamma_0/2 < \Omega_0$, for which

$$h(t) = \frac{\Omega_0^2 e^{-\gamma_0 t/2} \sin\left(\sqrt{\Omega_0^2 - \gamma_0^2/4}\, t\right)}{\sqrt{\Omega_0^2 - \gamma_0^2/4}}, \quad t \geq 0. \tag{5.78}$$

Moreover, the ideal performance is achieved when $T = 0\,K$ and $\gamma_0 \to 0$, in which case, we have

$$\int_0^\infty d\omega H_i(\omega) = \pi h(t_h)/2, \text{ where } \quad h(t_h) = \Omega_0, \tag{5.79}$$

and therefore,

$$\sigma_P^2 = (2\kappa/\pi)\int_0^\infty d\omega H_i(\omega) = \kappa h(t_h) = \theta. \tag{5.80}$$

Figure 5-8 shows the success probability for the underdamped two-pole response at $T = 0\,\mathrm{K}$ plotted versus $|\alpha_P|$ at $\theta|\alpha_P| = 2$. It can be seen that the optimum performance of the system is achieved at a low value of $|\alpha_P|$, for which $P_{success}$ is only about 0.55. This agrees with what we observed before. For large values of $|\alpha_P|$, we have that $\sigma_P^2|\alpha_P|^2 = \theta|\alpha_P|^2 = 2|\alpha_P|$ also has a large value, which, in turn, degrades the even-parity performance. For low values of $|\alpha_P|$, $P_{odd} \to 0$ as was seen before in Fig. 5-7.

### 5.3.1 Further discussion

The results shown in Fig. 5-8 demonstrate that our causal, non-instantaneous model for the cross-Kerr effect precludes the distributed parity gate's achieving high success-probability operation. One should also bear in mind that the fidelity we have derived is for the ideal case of no loss, no SPM, and no dispersion. Each of these issues can by itself significantly deteriorate the system performance. Moreover, the above performance has been achieved under the slow-response conditions, which makes its practicality and applicability questionable. However, there are still two other issues that should be addressed before coming to a definite conclusion about the parity gate's feasibility. First, within the range of validity of our model, we may still be able to do better if we choose an optimum response function for our medium. The material's response function $h(t)$ must satisfy the following conditions

$$\begin{gathered} h(t) = 0, \quad \text{for} \quad t < 0 \\ \textstyle\int dt h(t) = 1 \\ H_i(\omega) \geq 0 \quad \text{for} \quad \omega > 0, \end{gathered} \tag{5.81}$$

which define a convex set of functions. In this set, we are interested in finding the function $h(t)$ that maximizes the success probability of the gate. An easier problem is to find the function $h(t)$ that maximizes the ratio $\theta/\sigma_P$. Both these problems are analytically, as well as numerically, difficult. Even if we knew such a function, it will be difficult to find a material which has the desired response function. Nevertheless, it would be interesting to find the ultimate possible performance of the parity gate using our continuous-time model for the cross-Kerr effect.

The second issue is the validity of our model when we are dealing with atomic systems, possibly under electromagnetically induced transparency (EIT) conditions [64], illuminated by single photons. There are several proposals that use such systems to provide an effective cross-Kerr nonlinearity for single photons [59, 65, 66]. Our model may or may not be applicable to such scenarios. In our model, we translate what we expect to occur classically in a pure cross-Kerr medium into a quantum field-operator language, and then, we make it self-consistent by introducing phase noise operators with appropriate commutators. This is not necessarily what happens when a photon interacts with a single atom or a small ensemble of atoms. In these atom-interaction scenarios we expect to get some pulse-shape broadening, but how we can relate this effect to our medium response function, is yet to be investigated. Moreover, if the physical reason behind the phase noise and the non-instantaneous response function is molecular vibrations, it is logical to ask how much vibrational noise a single photon may cause. In other words, if we don't expect that atomic vibrations are at all significant at a single-photon level, do we need to worry about phase noise or not? These concerns prevents us from generalizing our assessment of the parity gate to all its possible implementations. The relationship between our model and an atom-based model, such as those we used for analyzing quantum memory units, is as interesting topic to be pursued, and it is one of possible routes for extending the work done in this thesis.

# Chapter 6

# Summary and Future Work

This thesis has been devoted to analyzing the performance of various distributed quantum architectures from a system-level standpoint, using analytical tools from physics and engineering. The systems we are interested in all employ neutral atoms, and some relevant metastable levels therein, to store and process quantum data. This can be accomplished with single atoms trapped in high-$Q$ optical cavities, or with atomic ensembles in free-space or low-finesse cavities. Depending on their energy-level configurations, the atoms can interact with and store the photon-number or the polarization-state information from an incoming light beam. Neutral atoms can also be treated as constituents of a nonlinear medium that enable interactions between a pair of light beams.

## 6.1 Thesis summary

In Chapter 2, we studied the loading problem for a variety of trapped-atom quantum memories. We used a system-reservoir approach to model a quantum-memory system illuminated by a single photon. We studied the cold-cavity and the two-level hot-cavity loading problems in detail, and we showed that other more complicated configurations, such as $\Lambda$-level, $V$-level, and double-$\Lambda$-level atoms, could be reduced to these basic cases. In particular, for the off-resonant Raman transition in a $\Lambda$-level atom, driven by a single photon on one leg and a classical control field on the other leg, we studied and compared two loading mechanisms. The main goal of our investigation was to find out about the dependence of the loading probability on the key system parameters, e.g., atom-light coupling rate as well as the input photon bandwidth. In the first approach, based on known techniques for adiabatic transfer, we realized that the ideal system performance could only be achieved long enough input pulses. If we are operating under the two-photon-resonance condition, then the higher the coupling rate is the higher the loading probability will be. In this adiabatic scheme, the coupling rate can only be increased, however, by using a shorter cavity, which results in a more demanding implementation. We proposed and analyzed a non-adiabatic approach—in which the control field was turned off at the peak of the loading probability—and showed that, for a fixed input bandwidth, its performance was optimized at an atom-light coupling rate that could be lower than what was needed in the adiabatic approach. This optimum coupling rate approaches zero, although very slowly, as we decrease the bandwidth associated with the driving photon. A preliminary report of this work has been presented at the 2006 Quantum Electronics and Laser Science Conference [67], and a journal paper is under preparation.

In Chapter 3, we analyzed the MIT-NU loading problem. The MIT-NU architecture uses a pair of trapped-rubidium-atom quantum memories, which are illuminated by the signal and idler outputs from an ultrabright doubly-resonant dual-OPA source of polarization-entangled photons. By approximating these outputs as a general biphoton state, we derived, analytically, the loading probabilities for adiabatic and non-adiabatic loading. In the latter case, we again observed the existence of an optimum coupling rate as a function of the driving pulse parameters. We showed that loading probabilities above 80% were achieveable at these optimum coupling rates, provided that the bandwidths associated with the input pulse is narrower than that of optical cavities. This work was also partially presented in [67].

We also studied the DLCZ system, proposed by Duan, Lukin, Cirac, and Zoller, which uses atomic ensembles as its quantum memories. We presented the first performance analysis for the DLCZ entanglement-distribution, repeater, and teleportation schemes that carefully treats errors arising from multiple-pair emissions and the use of non-resolving photon detectors. Our results show that the DLCZ protocol for entanglement distribution has a better throughput-versus-distance behavior than that of the MIT-NU architecture. Because of the linear optical module used for performing a partial Bell-state measurement, the DLCZ teleportation (repeater) protocol is a conditional scheme with maximum success probability of 1/4 (1/2). The MIT-NU system is capable of performing a full Bell-state measurement provided that we can successfully trap and manipulate single atoms in optical microcavities.

The DLCZ teleportation/repeater system requires highly efficient photon-number resolving detectors to achieve acceptable fidelity performance. These results have appeared in [68, 69].

Finally, in Chapter 5, we studied an optical solution to quantum computing based on the cross-Kerr nonlinearity in optical fibers. This system, proposed by a group of researchers in HP Laboratories, seeks to realize a universal set of quantum gates in the optical domain. We analyzed the cross-Kerr interaction between a single-photon pulse and a coherent-state pulse—which is at the core of the proposed scheme for two-qubit operations—using a continuous-mode formalism for the Kerr effect. The main features of our model are a finite response time for the medium as well as an accompanying phase noise at the output. We showed that, because of the response function's being non-instantaneous, a quantum operation is only feasible in the slow-response regime, in which the durations of the optical pulses are much shorter than that of the response function. Even in the slow-response regime, the output phase noise—whose mean-squared strength is proportional to the response function's amplitude—precludes achieving a high fidelity of operation. These results will be presented at the 2006 Conference on Quantum Communication, Measurement, and Computing [70].

## 6.2 Future work

There are several directions in which this thesis could be extended. Among them are:

1. The cavity-quantum-electrodynamic analysis given in Chapter 2 is applicable to a variety of other problems in quantum optics and quantum computing. Strong coupling regimes can be mimicked in quantum-dot systems embedded in semiconductor microcavities [71, 72, 73] as well as in Cooper pair boxes in superconductor devices [74]. Furthermore, qubit teleportation is not the only protocol for quantum communication [26, 27]. For instance, in [27], one can transfer a quantum state from one cavity to another by local entanglement, operations, and measurements. In this scheme, there are two atoms in each cavity; one serves as the main memory and the other as an auxiliary/backup qubit. The state transfer is done via a single photon traveling between cavities. This system has been analyzed using quantum Monte Carlo simulation. It would be interesting to study the system using the analytical tools we employed in Chapter 2 to enable a fair comparison with other quantum communication systems.

2. Single atoms can be trapped in potential wells in free space much easier than in a

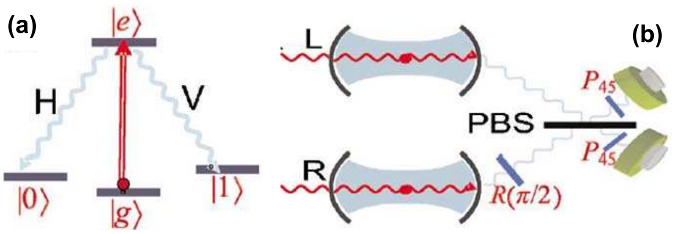

Figure 6-1: A from-the-memory architecture for entanglement distribution using ensembles of atoms with the level configuration as shown in (a). In (b), atomic ensembles L and R are assumed to be polarization entangled if one photon is detected at each photodetector.

cavity. Such trapped atoms can be used in controlled single-photon sources [75]. Using from-the-memory configuration, we can also employ them to distribute polarization entanglement. It would be interesting to study such systems within our mathematical framework.

3. Our treatment of the MIT-NU loading problem is only an approximation to the real scenario in which the output of the dual-OPA source is in a Gaussian state. This implies that, for a more complete analysis, we have to account for higher order terms, i.e., multiple-photon cases. This analysis of full Gaussian-state loading may be intractable, but it should be possible to analyze cases with at most two photons each in the signal and idler beams.

4. One major problem that makes the DLCZ teleportation scheme inefficient is its dependence on the exact number of photons. We can circumvent this problem by switching to polarization states. One way to do that is to use atoms with the atomic configurations shown in Fig. 6-1(a). In Fig. 6-1(a), we drive the transition $|g\rangle \rightarrow |e\rangle$ by an external field; the atom in the upper state can then undergo a Raman transition to the state $|0\rangle$ or $|1\rangle$, which corresponds, respectively, to the emission of a photon in the horizontal or vertical polarization. Now, by pumping two of these atoms coherently, and combining their outputs at a polarizing beam splitter [76], as shown in Fig. 6-1(b), one can show that both single-photon detectors will click whenever the two atomic systems are in the singlet state [76]. Because this scheme requires both detectors to register photocounts, it can be more reliable than the DLCZ system, which works on the basis of a single photodetection event. It is foreseeable that this method has a lower throughput.

Alternatively, with recent advances in light-matter qubit conversion [50, 51, 32]—by which we can transfer the state of a single photon to the collective state of an atomic ensemble and *vice versa*—we can use a memory-to-memory configuration to generate a photon, whose polarization is either $H$ or $V$, entangled with an atomic ensemble, and let this photon load the other party's memory [32]. The entanglement between these two memories can then be verified by a setup similar to Fig. 6-1(b). We can also use the light-matter conversion technique to absorb a pair of polarization-entangled photons. This entangled pair can either be produced by the downconversion process or by two-photon processes in atomic ensembles [77]. In none of the above schemes, however, are we capable of verifying the establishment of the entanglement without destroying it.

5. Another issue in dealing with atomic ensembles is the possibility of emitting or absorbing more than one photon. This precludes us from extending some well-known techniques for treating single atoms to the atomic-ensemble case. There is a new blockade mechanism by which we can prevent the atomic ensemble from absorbing more than one excitation, thus treat the atomic ensemble as a two-level atom. This is based on the light-shift imbalance in a Raman transition [78], and it has been proposed for realizing quantum communication and computation systems with atomic ensembles [79]. It would be interesting to employ the techniques that we learned in Chapters 2 and 4 to analyze these systems.

6. As mentioned earlier, our treatment of the cross-Kerr effect in Chapter 5 is applicable to the nonlinear media, such as optical fiber, whose constituent atoms or molecules are bound to their environments, thus inducing photon-phonon interactions. This may not be the case if we use single trapped atoms [59] or atomic ensembles [66] as the source of nonlinearity. The relationship between our continuous-time formalism in Chapter 5 and the above atomic schemes is an interesting topic for future investigation.

Quantum information science is an emerging discipline whose theoretical progress to date has far outstripped its experimental achievements. Although it has not fundamentally changed our understanding of the physical universe, it has definitely motivated us to look closer at it. This thesis was an attempt to dig deeper into some physical phenomena to help us obtain a more accurate detailed understanding of their impact on neutral-atom based quantum communication and computation. Whether this refined knowledge will result in concrete, useful applications is the main challenge of years to come.

# Appendix A

# Hot-cavity Loading: A Heisenberg-Langevin Analysis

In this appendix, we present alternative derivations to what we obtained in Sections 2.2 and 2.4 for, respectively, two-level and $V$-level atoms illuminated by single photons. Our new approach is based on Heisenberg-Langevin (HL) equations of motion, which we introduced in Section 2.1 for the cold-cavity loading problem. We can easily extend those results to include any intracavity system that interacts with a reservoir of modes through the linear coupling term $\hbar\Gamma \int d\omega (a_\omega^\dagger b + b^\dagger a_\omega)$ in its Hamiltonian[1], where $b$ is the cavity-mode operator that connects the outside world to the internal system. Gardiner and Collett [37] have shown that the Heisenberg equation of motion for any intracavity operator $a$ can be written as follows:

$$\dot{a} = -(i/\hbar)[a, H_{sys}] - [a, b^\dagger](\kappa b - \sqrt{2\kappa} A_{in}) + (\kappa b^\dagger - \sqrt{2\kappa} A_{in}^\dagger)[a, b], \tag{A.1}$$

where all operators are evaluated at time $t$, $H_{sys}$ is the intracavity Hamiltonian, and $A_{in}(t) = (-i/\sqrt{2\pi}) \int d\omega \exp(-i\omega t) a_\omega(0)$. Note that there is a factor $-i$ in front of the integral as compared to what we had in Chapter 2. This is only for the notational convenience and has no effect on our final results. The above equation can be derived along the same lines of derivation that we gave in (2.11) and (2.12).

In the following, we first consider a two-level atom inside a cavity illuminated by a

---

[1] (a) Because of the abundance of operators in this Appendix, we denote any quantum operator $\hat{a}$ by $a$. (b) Unless otherwise noted, we use the same notation that we used in Chapter 2.

single photon. An HL loading analysis for this problem was performed by V. Giovannetti and L. Maccone (GM) [80]. Their work provides the basis for the other problems that we consider in this appendix. Thus we begin, in Section A.1, by rederiving the GM solution, and then follow, in Section A.2, by extending the solution to the case of an atom in the $V$ configuration. In the latter problem, the two atomic transitions are excited by an optical beam in an arbitrary polarization state. Finally, in Section A.3, we consider a pair of two-level atoms illuminated by a pair of photon-number-entangled photons.

## A.1 A two-level atom in a cavity with external single-photon excitation

Consider the two-level atom in Fig. 2-2. In order to analyze the intracavity evolution, it suffices to find the HL equations for $b$, $\sigma_{ee}$, and $\sigma_{eg}$. Using (A.1), these equations are as follows:

$$\dot{b}(t) = -(i\omega_0 + \kappa)b(t) - ig\sigma_{ge}(t) + \sqrt{2\kappa}A_{in}(t), \tag{A.2}$$

$$\dot{\sigma}_{ee}(t) = ig[\sigma_{ge}(t)b^\dagger(t) - \sigma_{eg}(t)b(t)], \tag{A.3}$$

$$\dot{\sigma}_{eg}(t) = i\omega_a\sigma_{eg}(t) + ig[\sigma_{gg}(t) - \sigma_{ee}(t)]b^\dagger(t). \tag{A.4}$$

For our loading problem, we assume the Langevin operator is initially in the state given by (2.1). Then, the loading probability, i.e., the probability that, at time $t$, the photon has been absorbed and the atom is in its excited state, is given by $\langle\sigma_{ee}(t)\rangle$. To evaluate this average, we can repeatedly use (A.2)–(A.4) until we obtain a closed set of linear equations that can be solved by well-known methods such as the Laplace transform. The main issue that helps us get to this point is the fact that there is only one excitation in the whole system. As a result, there are only certain states that are possible for the intracavity system as we saw in Section 2.2. For instance, knowing that the atom is in its excited state implies that the field operator $b$ is in the vacuum state. There is a little bit of subtlety, however, in dealing with this problem, which can be formulated in the following lemma.

**Lemma A.1.** *For any function $f(t,t') = f_a(t)f_p(t)f_{in}(t')$, where $f_a(t)$ is an atomic operator, $f_p(t)$ is a photonic operator (inside the cavity), and $f_{in}(t')$ is a function of the input Langevin operator, all in the Heisenberg picture, we have* *(a)* $\langle f(t,t')\rangle = \left\langle \langle f_a(t) f_p(t)\rangle_c f_{in}(t')\right\rangle$*, and therefore,* $\langle f_a(t) f_p(t)\rangle_c = 0 \Rightarrow \langle f(t,t')\rangle = 0$*. Here,* $\langle\cdot\rangle_c$ *denotes averaging over the intracavity system.*

*(b)* $\langle f_a(t) f_p(t)\rangle_c$ *is a function of* $A_{in}$*. It is zero if* $\langle\psi_1|f_a(0)f_p(0)|\psi_2\rangle = 0$*, where*

$$|\psi_1\rangle, |\psi_2\rangle \in \{|g\rangle|0\rangle_b, |g\rangle|1\rangle_b, |e\rangle|0\rangle_b\}. \tag{A.5}$$

*The above three states represent all possible intracavity scenarios: no photon absorption, absorption by the cavity, and absorption by the atom. For example,* $b(0)\sigma_{ee}(0)$ *takes all these states to* $0$*, and therefore,* $\langle b(t)\sigma_{ee}(t) f_{in}(t')\rangle = 0$*.*

Now, we can start finding a closed set of first-order linear differential equations from which $\langle\sigma_{ee}(t)\rangle$ can be obtained. The first equation comes directly from (A.3), which introduces a new term $W(t) = b(t)\sigma_{eg}(t)$ for which we have (hereafter, we may neglect to write $t$ explicitly in our expressions)

$$\begin{aligned}
\dot{W} &= \dot{b}\sigma_{eg} + b\dot{\sigma}_{eg} \\
&= \left[-(i\omega_0+\kappa)b - ig\sigma_{ge} + \sqrt{2\kappa}A_{in}\right]\sigma_{eg} + \ b\left[i\omega_a\sigma_{eg} + ig(\sigma_{gg}-\sigma_{ee})b^\dagger\right] \\
&= -(i(\omega_0-\omega_a)+\kappa)W - ig\sigma_{gg} + igb\sigma_{gg}b^\dagger - igb\sigma_{ee}b^\dagger + \sqrt{2\kappa}A_{in}\sigma_{eg} \\
&= -(i(\omega_0-\omega_a)+\kappa)W + igb^\dagger\sigma_{gg}b - ig\sigma_{ee} - igb^\dagger\sigma_{ee}b + \sqrt{2\kappa}A_{in}\sigma_{eg},
\end{aligned} \tag{A.6}$$

where we used $[b, b^\dagger] = 1$ in the last step. Defining new terms

$$A_0 = 2\mathrm{Re}\langle W\rangle \ \text{ and } \ A_1 = -2\mathrm{Im}\langle W\rangle = i\langle W\rangle - i\langle W\rangle^*, \tag{A.7}$$

we have

$$\dot{A}_0 = -\kappa A_0 - (\omega_0-\omega_a)A_1 + \mathrm{Re}\{F_1(t,t)\} \tag{A.8}$$

and

$$\dot{A}_1 = -\kappa A_1 + (\omega_0-\omega_a)A_0 + 2g\langle\sigma_{ee}\rangle + 2gA_2 - \mathrm{Im}\{F_1(t,t)\} \tag{A.9}$$

where from Lemma A.1, $\left\langle b^\dagger b\sigma_{ee}\right\rangle = 0$,

$$A_2 = \left\langle b^\dagger(\sigma_{ee}-\sigma_{gg})b\right\rangle = -\left\langle b^\dagger\sigma_{gg}b\right\rangle \tag{A.10}$$

and

$$F_1(t,t') = 2\sqrt{2\kappa}\left\langle \sigma_{eg}(t)A_{in}(t')\right\rangle . \tag{A.11}$$

Repeating the same procedure for the above new terms, we obtain (using $\dot{\sigma}_{gg} + \dot{\sigma}_{ee} = 0$)

$$\dot{A}_2 = -\left\langle \dot{b}^\dagger \sigma_{gg} b\right\rangle - \left\langle b^\dagger \sigma_{gg}\dot{b}\right\rangle + \left\langle b^\dagger \dot{\sigma}_{ee} b\right\rangle \tag{A.12}$$

where using (A.2)

$$\begin{aligned} \dot{b}^\dagger \sigma_{gg} b &= \left[(i\omega_0 - \kappa)b^\dagger + ig\sigma_{eg} + \sqrt{2\kappa}A_{in}^\dagger\right]\sigma_{gg} b \\ \Longrightarrow \quad \left\langle \dot{b}^\dagger \sigma_{gg} b\right\rangle &= -(i\omega_0 - \kappa)A_2 + ig\langle W\rangle + \sqrt{2\kappa}\left\langle A_{in}^\dagger \sigma_{gg} b\right\rangle \end{aligned} \tag{A.13}$$

plus

$$\begin{aligned} b^\dagger \sigma_{gg} \dot{b} &= b^\dagger \sigma_{gg}\left[-(i\omega_0 + \kappa)b - ig\sigma_{ge} + \sqrt{2\kappa}A_{in}\right] \\ \Longrightarrow \quad \left\langle b^\dagger \sigma_{gg} \dot{b}\right\rangle &= (i\omega_0 + \kappa)A_2 - ig\langle W\rangle^* + \sqrt{2\kappa}\left\langle b^\dagger \sigma_{gg} A_{in}\right\rangle \end{aligned} \tag{A.14}$$

and using $\left\langle b^\dagger b b \sigma_{eg}\right\rangle_c = 0$ along with (A.3), we have

$$\left\langle b^\dagger \dot{\sigma}_{ee} b\right\rangle = ig\left\langle b^\dagger\left(\sigma_{ge}b^\dagger - \sigma_{eg}b\right)b\right\rangle = 0. \tag{A.15}$$

Using the above results, we obtain

$$\dot{A}_2 = -2\kappa A_2 - gA_1 + \mathrm{Re}\{F_2(t,t)\} \tag{A.16}$$

where

$$F_2(t,t') = 2\sqrt{2\kappa}\left\langle b^\dagger(t)(\sigma_{ee}(t) - \sigma_{gg}(t))A_{in}(t')\right\rangle = -2\sqrt{2\kappa}\left\langle b^\dagger(t)\sigma_{gg}(t)A_{in}(t')\right\rangle . \tag{A.17}$$

Among all new terms introduced so far, only $F_1$ and $F_2$ explicitly include the input noise operator. In fact, because $A_0$, $A_1$, and $A_2$, are all initially zero, $F_1$ and $F_2$ play the role of driving forces for the other terms. For instance, if the noise operator is initially in the vacuum state, then, $F_1$ and $F_2$ are both zero at all times, and there will be no evolution in

$\sigma_{ee}(t)$ according to (A.8), (A.9), and (A.16). This is also the case for $\sigma_{gg}(t)$, and we have

$$\langle \sigma_{gg}(t) \rangle = \langle \sigma_{gg}(0) \rangle = 1 \quad , \text{ no input photons.} \tag{A.18}$$

Now, we derive the evolution of the driving forces and show that they will close the set of required equations. From (A.11) and (A.4), we have

$$\frac{\partial}{\partial t} F_1(t,t') = i\omega_a F_1(t,t') - igF_2(t,t') \tag{A.19}$$

Also, from (A.17), (A.2), and (A.3), we have

$$\frac{\partial}{\partial t} F_2(t,t') = (i\omega_0 - \kappa) F_2(t,t') - igF_1(t,t') - 4\kappa \left\langle A_{in}^{\dagger}(t) \sigma_{gg}(t) A_{in}(t') \right\rangle \tag{A.20}$$

where, from Lemma A.1, $\left\langle b^{\dagger}(t)(\sigma_{ge}(t) b^{\dagger}(t) - \sigma_{eg}(t) b(t)) A_{in}(t') \right\rangle = 0$. The last term in (A.20) can be simplified further using (2.15). Now, using (A.18) and (2.15), we get

$$\frac{\partial}{\partial t} F_2(t,t') = -igF_1(t,t') + (i\omega_0 - \kappa) F_2(t,t') - 4\kappa \Phi(t') \Phi^*(t). \tag{A.21}$$

Equations (A.8), (A.9), (A.16), (A.19), and (A.21) plus $\langle \dot{\sigma}_{ee} \rangle = -gA_1$, summarized in Table A.1, comprise a set of linear equations that can be solved using Laplace transforms. In particular, the driving terms $F_1$ and $F_2$ can be obtained from (A.19) and (A.21) using the initial conditions $F_1(0,t') = F_2(0,t') = 0$. The results are as follows:

$$F_1(t,t') = -i \frac{4g\kappa \Phi(t')}{\xi'} \int_0^t d\tau \Phi^*(\tau) \left( e^{\alpha_+(\tau - t)} - e^{\alpha_-(\tau - t)} \right) \tag{A.22}$$

and

$$F_2(t,t') = -4\kappa \Phi(t') \int_0^t d\tau \Phi^*(\tau) \left( \beta_+ e^{\alpha_+(\tau - t)} + \beta_- e^{\alpha_-(\tau - t)} \right) \tag{A.23}$$

where

$$\begin{aligned} \alpha_{\pm} &= -i\omega_a + \frac{\kappa - i(\omega_0 - \omega_a) \pm \xi'}{2} \\ \beta_{\pm} &= \frac{1}{2} \pm \frac{\kappa - i(\omega_0 - \omega_a)}{2\xi'} \\ \xi' &= \sqrt{[\kappa - i(\omega_0 - \omega_a)]^2 - 4g^2}. \end{aligned} \tag{A.24}$$

| **Moment Equations** | **Moment Definitions** |
|---|---|
| $\langle\dot{\sigma}_{ee}\rangle = -gA_1$<br>$\dot{A}_0 = -\kappa A_0 - (\omega_0-\omega_a)A_1 + \mathrm{Re}\{F_1(t,t)\}$<br>$\dot{A}_1 = 2g\langle\sigma_{ee}\rangle + (\omega_0-\omega_a)A_0 - \kappa A_1 + 2gA_2 - \mathrm{Im}\{F_1(t,t)\}$<br>$\dot{A}_2 = -gA_1 - 2\kappa A_2 + \mathrm{Re}\{F_2(t,t)\}$<br>$\frac{\partial}{\partial t}F_1(t,t') = i\omega_a F_1(t,t') - igF_2(t,t')$<br>$\frac{\partial}{\partial t}F_2(t,t') = -igF_1(t,t') + (i\omega_0-\kappa)F_2(t,t') - 4\kappa\Phi(t')\Phi^*(t)$ | $A_0 = \left\langle b^\dagger\sigma_{ge} + b\sigma_{eg}\right\rangle$<br>$A_1 = -i\left\langle b^\dagger\sigma_{ge} - b\sigma_{eg}\right\rangle$<br>$A_2 = \left\langle b^\dagger(\sigma_{ee}-\sigma_{gg})b\right\rangle$<br>$F_1(t,t') = 2\sqrt{2\kappa}\,\langle\sigma_{eg}A_{in}(t')\rangle$<br>$F_2(t,t') = -2\sqrt{2\kappa}\,\left\langle b^\dagger\sigma_{gg}A_{in}(t')\right\rangle$ |

Table A.1: The set of moment equations for a two-level atom in a cavity illuminated by a single photon.

Now solving for $\langle\sigma_{ee}\rangle$, in the on-resonance case $\omega_0 = \omega_a$, we find the following result for the time-dependence of the absorption probability:

$$\begin{aligned}\langle\sigma_{ee}(t)\rangle &= -\frac{g}{2\xi'}\int_0^t d\tau\,\mathrm{Im}\{F_1(\tau,\tau)\}e^{-\kappa(t-\tau)}\left(e^{-\xi'(t-\tau)} - e^{\xi'(t-\tau)}\right)\\ &\quad +\frac{1}{2\xi'^2}\int_0^t d\tau\left(2g^2\mathrm{Re}\{F_2(\tau,\tau)\} - g\kappa\mathrm{Im}\{F_1(\tau,\tau)\}\right)e^{-\kappa(t-\tau)}\\ &\qquad\times\left(2 - e^{-\xi'(t-\tau)} - e^{\xi'(t-\tau)}\right). \end{aligned} \tag{A.25}$$

Although it may not be clear at the first glance, the above equation is equivalent to the compact result that we obtained in (2.27).

## A.2 A trapped three-level atom in the $V$ configuration illuminated by an arbitrarily polarized single photon

In this section, we extend our solution for the two-level atom to the case of a three-level $V$-configuration atom, as shown in Fig. A-1. A photon in the cavity mode governed by field operator $b_+$, corresponding to the $\sigma_+$ polarization, can stimulate the transition $|g\rangle \rightarrow |2\rangle$. Likewise, a photon in the cavity mode associated with field operator $b_-$, corresponding to the $\sigma_-$ polarization, can stimulate the transition $|g\rangle \rightarrow |3\rangle$. The problem we are interested in is how such an atom can absorb a photon with an arbitrary polarization. To answer this question, we follow the same steps we took in the previous section starting with the intracavity Hamiltonian

$$\begin{aligned}H_c = \hbar\omega_0\left(b_+^\dagger b_+ + b_-^\dagger b_-\right) + \hbar\omega_a\left(\sigma_{22}+\sigma_{33}\right)\\ +\hbar g\left(b_+^\dagger\sigma_{g2} + b_+\sigma_{2g} + b_-^\dagger\sigma_{g3} + b_-\sigma_{3g}\right)\end{aligned} \tag{A.26}$$

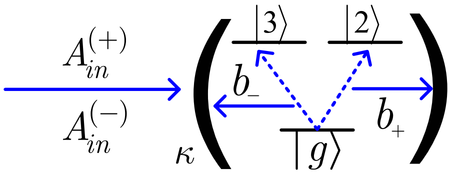

Figure A-1: A single V-configuration atom illuminated by a single photon with an arbitrary polarization.

where the first two terms are, respectively, the field and the atom Hamiltonians, and the last term models their interaction. We assume all intracavity operators are initially at rest, and the input field is in a polarization state:

$$|\psi_0\rangle = |g\rangle \otimes |0\rangle_{b_+} \otimes |0\rangle_{b_-} \otimes \int d\omega\phi(\omega) \left(\alpha \, |1_\omega\rangle_{\sigma_+} + \beta \, |1_\omega\rangle_{\sigma_-}\right), \tag{A.27}$$

where $|1_\omega\rangle_{\sigma_\pm}$ represents a single photon at the frequency $\omega$ with the polarization $\sigma_\pm$.

The parameter we are interested in is the probability of loading the atom with the following normalized state

$$|e\rangle = \alpha|2\rangle + \beta|3\rangle \tag{A.28}$$

or, equivalently, $\langle\sigma_{ee}\rangle$. Using a similar treatment to the previous section, we can write a system of HL equations based on (A.26), from which a set of linear differential equations can be obtained. In this way, it can be shown that the V-level system behaves like three two-level systems, one for each of transitions $g \leftrightarrow 2$, $g \leftrightarrow 3$, and $2 \leftrightarrow 3$. There is a shortcut to this approach by introducing a new basis for the problem consisting of $|e\rangle$, $|f\rangle$, and $|g\rangle$, where

$$|f\rangle = \beta^*|2\rangle - \alpha^*|3\rangle. \tag{A.29}$$

Here, $|f\rangle$ is an unwanted state; it represents an atom loaded with an orthogonal state to the desired state $|e\rangle$. We define the fidelity of loading by the ratio $\langle\sigma_{ee}\rangle/(\langle\sigma_{ee}\rangle + \langle\sigma_{ff}\rangle)$. The Hamiltonian (A.26) takes the following form in the new basis:

$$\begin{aligned} H_c &= \hbar\omega_0 b^\dagger b + \hbar\omega_a\sigma_{ee} + \hbar g\left(b^\dagger\sigma_{ge} + b\sigma_{eg}\right) \\ &\quad + \hbar\omega_0 b_\perp^\dagger b_\perp + \hbar\omega_a\sigma_{ff} + \hbar g\left(b_\perp^\dagger\sigma_{gf} + b_\perp\sigma_{fg}\right) \end{aligned} \tag{A.30}$$

where

$$b = \alpha^* b_+ + \beta^* b_- \quad \text{and} \quad b_\perp = \beta b_+ - \alpha b_- \tag{A.31}$$

represent two independent field operators, i.e., $[b, b_\perp] = [b, b_\perp^\dagger] = 0$ and $[b, b^\dagger] = [b_\perp, b_\perp^\dagger] = 1$. We can see that the Hamiltonian (A.30) is the sum of two independent two-level-atom Hamiltonians. Thus we obtain the same HL equations, as in (A.2) and (A.3), for the current definitions of $b$ and $\sigma_{ee}$, respectively, where for the present problem

$$A_{in} = \alpha^* A_{in}^{(+)} + \beta^* A_{in}^{(-)} \tag{A.32}$$

with

$$A_{in}^{(\pm)}(t) = \frac{-i}{\sqrt{2\pi}} \int d\omega e^{-i\omega t} a_\pm(\omega) \tag{A.33}$$

and $a_\pm(\omega)|1_{\omega'}\rangle_{\sigma\pm} = \delta(\omega - \omega')|\mathbf{0}\rangle_{R\pm}$, where $R_\pm$ denotes the reservoir corresponding to the $\sigma_\pm$ polarization. There are some additional terms to the HL equations for $\sigma_{eg}$ and $\sigma_{gg}$, however, which arise from the ground state's coupling to both $|e\rangle$ and $|f\rangle$. We have

$$\dot{\sigma}_{eg}(t) = i\omega_a \sigma_{eg}(t) + ig[\sigma_{gg}(t) - \sigma_{ee}(t)]b^\dagger(t) - igb_\perp^\dagger(t)\sigma_{ef}(t) \tag{A.34}$$

and

$$\dot{\sigma}_{gg}(t) = -ig[\sigma_{ge}(t)b^\dagger(t) - \sigma_{eg}(t)b(t)] - ig[\sigma_{gf}(t)b_\perp^\dagger(t) - \sigma_{fg}(t)b_\perp(t)]. \tag{A.35}$$

Using the same treatment as in the previous section, we can obtain the same set of equations as in Table A.1 for $\langle\sigma_{ee}\rangle$. The reason that the $\langle\sigma_{ee}\rangle$ equations are unaffected by the additional terms in (A.34) and (A.35) is that the new resulting moments from these additional terms are all zero. For instance, $\langle bb_\perp^\dagger \sigma_{ef}\rangle = 0$ because if the atom is in the state $|e\rangle$ or $|f\rangle$, then there is no photon left in any field operators including $b$. This results in no changes in $W$, and therefore in (A.8) and (A.9). By the same token, $\langle b_\perp^\dagger \sigma_{ef}\rangle = 0$ which results in no changes in (A.19). Similarly, $\langle b^\dagger b b_\perp^\dagger \sigma_{gf}\rangle = 0$ and $\langle b^\dagger b_\perp^\dagger \sigma_{gf}\rangle = \langle b^\dagger b_\perp \sigma_{fg}\rangle = 0$, which leave (A.16) and (A.21) unchanged, respectively. This proves that these two problems have the same dynamical evolution as far as average quantities are concerned. Moreover, writing the HL equation for $b_\perp$, we find that it involves a noise operator $A_{in}^\perp = \beta A_{in}^{(+)} - \alpha A_{in}^{(-)}$, which takes the initial state (A.27) to zero. This leaves no driving forces in (A.21) and results in $\langle\sigma_{ff}\rangle = 0$. It follows that the fidelity of the loading process is unity, i.e., there is no chance

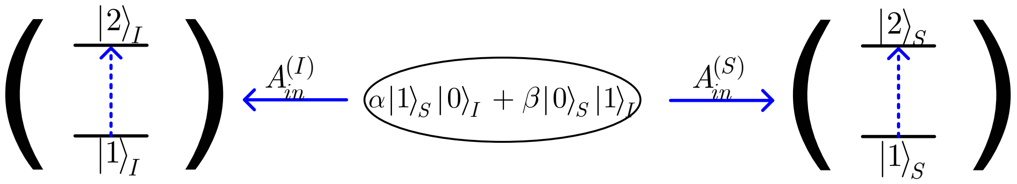

Figure A-2: Two two-level single atoms trapped in two similar cavities illuminated by a pair of photons in an entangled state.

to load the atom with something outside the state space spanned by the desired state $|e\rangle$ and the ground state $|g\rangle$. The results of this section are independent of $\alpha$ and $\beta$, and therefore they hold regardless of the polarization state of the input light.

## A.3 Loading a pair of two-level atoms with a pair of entangled photons

Teleportation protocols begin by preparing their two parties in an entangled state. For scenarios in which two-level atoms are being used as QMUs, this entangled state can be represented by a superposition of ground-excited states. In this section, we study the problem of loading two atoms with such an entangled state by means of a pair of photons entangled in photon number, here either zero or one. Figure A-2 shows a schematic of this architecture. Each atom in Fig. A-2 can be individually modeled by a two-level atom Hamiltonian and the set of HL equations (A.2)–(A.4). The Hamiltonian for the system of two cavities is then simply the sum of these two (we label the atoms $S$ and $I$ corresponding to the signal and idler beams of the photon source):

$$H_c = H_S + H_I, \tag{A.36}$$

where

$$H_k = \hbar\omega_0 b_k^\dagger b_k + \hbar\omega_a \sigma_{22}^{(k)} + \hbar g(b_k^\dagger \sigma_{12}^{(k)} + b_k \sigma_{21}^{(k)}), \tag{A.37}$$

where $\sigma_{ij}^{(k)} = |i\rangle_{kk}\langle j|$, $k \in \{S, I\}$.

The atoms, cavity operators, and input noise operators to each cavity, $A_{in}^{(S)}$ and $A_{in}^{(I)}$, are initially in the following state

$$|\psi_0\rangle = |1\rangle_S \otimes |1\rangle_I \otimes |0\rangle_{b_S} \otimes |0\rangle_{b_I} \otimes \int d\omega\phi(\omega) \Big(\alpha\, |1_\omega\rangle_S\, |\mathbf{0}\rangle_{R_I} + \beta\, |\mathbf{0}\rangle_{R_S}\, |1_\omega\rangle_I\Big), \tag{A.38}$$

where $|1_\omega\rangle_{S/I}$ represents a single photon at the frequency $\omega$ in the signal/idler beam. Here we are interested in finding $\langle\sigma_{ee}(t)\rangle$ where

$$|e\rangle = \alpha|2\rangle_S|1\rangle_I + \beta|1\rangle_S|2\rangle_I \tag{A.39}$$

Similar to the previous section, we start by rewriting the Hamiltonian in a new basis that will simplify the analysis. We need the ground state $|g\rangle = |1\rangle_S|1\rangle_I$, the unwanted state $|f\rangle = \beta^*|2\rangle_S|1\rangle_I - \alpha^*|1\rangle_S|2\rangle_I$, and the inaccessible (because only one photon is available) state $|d\rangle = |2\rangle_S|2\rangle_I$ to complete the basis. In this new basis, the Hamiltonian (A.36) satisfies

$$H_c = H_{eg} + H_{fg} + H_d \tag{A.40}$$

where

$$H_{eg} = \hbar\omega_0 b^\dagger b + \hbar\omega_a\sigma_{ee} + \hbar g b\sigma_{eg} + \hbar g\sigma_{ge}b^\dagger \tag{A.41}$$

represents a two-level system between $|e\rangle$ and $|g\rangle$,

$$H_{fg} = \hbar\omega_0 b_\perp^\dagger b_\perp + \hbar\omega_a\sigma_{ff} + \hbar g b_\perp\sigma_{fg} + \hbar g\sigma_{gf}b_\perp^\dagger \tag{A.42}$$

represents a two-level system between $|f\rangle$ and $|g\rangle$, and

$$H_d = 2\hbar\omega_a\sigma_{dd} + \hbar g(b\sigma_{df'} + \sigma_{f'd}b^\dagger) + \hbar g(b_\perp\sigma_{df''} + \sigma_{f''d}b_\perp^\dagger) \tag{A.43}$$

represents the transitions to the two-excitation state $|d\rangle$. In these equations

$$\begin{aligned} |f'\rangle &= 2\alpha^*\beta^*|e\rangle + (|\beta|^2 - |\alpha|^2)|f\rangle = \beta^*|2\rangle_S|1\rangle_I + \alpha^*|1\rangle_S|2\rangle_I \\ |f''\rangle &= (|\beta|^2 - |\alpha|^2)|e\rangle - 2\alpha\beta|f\rangle = -\alpha|2\rangle_S|1\rangle_I + \beta|1\rangle_S|2\rangle_I \end{aligned} \tag{A.44}$$

and

$$b = \alpha^* b_S + \beta^* b_I \quad \text{and} \quad b_\perp = \beta b_S - \alpha b_I \tag{A.45}$$

are the two independent intracavity field operators. From (A.40), we obtain the following

HL equations for the above system,

$$
\begin{aligned}
\dot{b}(t) &= -(i\omega_0+\kappa)b(t) - ig\sigma_{ge}(t) - ig\sigma_{f'd}(t) + \sqrt{2\kappa}A_{in}(t) \\
\dot{\sigma}_{ee}(t) &= ig[\sigma_{ge}(t)b^\dagger(t) - \sigma_{eg}(t)b(t)] - 2ig[\alpha^*\beta^*\sigma_{ed}(t)b^\dagger(t) - \alpha\beta\sigma_{de}(t)b(t)] \\
&- (|\beta|^2-|\alpha|^2)ig[\sigma_{ed}(t)b_\perp^\dagger(t) - \sigma_{de}(t)b_\perp(t)] \\
\dot{\sigma}_{eg}(t) &= i\omega_a\sigma_{eg}(t) + ig[\sigma_{gg}(t)-\sigma_{ee}(t)]b^\dagger(t) + 2\alpha\beta ig\sigma_{de}(t)b(t) \\
&+ (|\beta|^2-|\alpha|^2)ig\sigma_{de}(t)b_\perp(t) \qquad \text{(A.46)}
\end{aligned}
$$

where

$$A_{in} = \alpha^* A_{in}^{(S)} + \beta^* A_{in}^{(I)} \qquad \text{(A.47)}$$

with

$$A_{in}^{(k)}(t) = \frac{-i}{\sqrt{2\pi}}\int d\omega e^{-i\omega t}a_k(\omega) \qquad \text{(A.48)}$$

and $a_k(\omega)|1_{\omega'}\rangle_k = \delta(\omega-\omega')|\mathbf{0}\rangle_{R_k}$, $k \in \{S, I\}$.

The rest of the game is the same as previous sections. We use the HL equations (A.46) to find a closed set of linear equations from which $\langle\sigma_{ee}(t)\rangle$ can be obtained. We use the same tricks we used in the previous sections to meticulously manipulate all the moments of interest. The main thing that simplifies this calculation is the fact that all transitions to the upper state $|d\rangle$ are forbidden, in the context of the present problem, because there is only one photon altogether in the input beams, and we start with no photons in the cavities and both atoms in their ground states. Therefore, all moments of the form $\langle f_p\sigma_{dx}\rangle$, where $f_p$ is any photonic operator and $|x\rangle$ is any atomic state, vanish. Using this fact, we find that the same set of equations as in Table A.1 is also applicable to the current problem, and $\langle\sigma_{ee}(t)\rangle$ is still given by (A.25).

# Appendix B

# DLCZ Fidelity Analysis

In this appendix, we derive the fidelity of entanglement for the DLCZ architecture. We assume photon-number resolving detectors (PNRDs) are being used in the detection setup, and we find the fidelity $F_{j,\mathrm{d}}$ of being in an arbitrary pure state $|\psi_\mathrm{d}\rangle = d_L|1\rangle_L|0\rangle_R + d_R|0\rangle_L|1\rangle_R$ after the occurrence of event $\hat{M}_j$ as defined in (4.14) and (4.15). From (4.20), and the fact that $\langle\psi_\mathrm{d}|\hat{D}_N(\hat{S}_L,\zeta_a^L)\hat{D}_N(\hat{S}_R,\zeta_a^R)|\psi_\mathrm{d}\rangle = 1 - |d_L^*\zeta_a^L + d_R^*\zeta_a^R|^2$, we obtain

$$\begin{aligned} F_{j,\mathrm{d}} &\equiv \langle\psi_\mathrm{d}|\hat{\rho}_{\mathrm{pm}_j}|\psi_\mathrm{d}\rangle \\ &= \frac{1}{P_j}\int\frac{\mathrm{d}^2\zeta_a^L}{\pi}\int\frac{\mathrm{d}^2\zeta_a^R}{\pi}\left(1 - \left|d_L^*\zeta_a^L + d_R^*\zeta_a^R\right|^2\right) \\ &\quad\times\int\frac{\mathrm{d}^2\zeta_{p1}}{\pi}\int\frac{\mathrm{d}^2\zeta_{p2}}{\pi}\,\chi_A^{\hat{\rho}_\mathrm{out}}(\zeta_a^L,\zeta_a^R,\zeta_{p1},\zeta_{p2})\left(1 - |\zeta_{pj}|^2\right), \quad \text{PNRD, } j = 1,2, \end{aligned} \tag{B.1}$$

where $P_j$ has been obtained in (4.21). The key technique to evaluating the above integral lies in the Gaussian form of $\chi_A^{\hat{\rho}_\mathrm{out}}(\zeta_a^L,\zeta_a^R,\zeta_{p1},\zeta_{p2})$, as described in (4.11). This function can be written in the following form

$$\chi_A^{\hat{\rho}_\mathrm{out}}(\zeta_a^L,\zeta_a^R,\zeta_{p1},\zeta_{p2}) = (2\pi)^4\sqrt{\det\mathbf{K}}\,G(\boldsymbol{\zeta},\mathbf{K}), \tag{B.2}$$

where

$$\boldsymbol{\zeta} = [\zeta_{ar}^L, \zeta_{ai}^L, \zeta_{pr}^-, \zeta_{pi}^-, \zeta_{pr}^+, \zeta_{pi}^+, \zeta_{ar}^R, \zeta_{ai}^R]^T, \tag{B.3}$$

$$G(\boldsymbol{x},\mathbf{C}) = (2\pi)^{-n/2}(\det\mathbf{C})^{-1/2}\exp\left(-\boldsymbol{x}^T\mathbf{C}^{-1}\boldsymbol{x}/2\right), \tag{B.4}$$

and $\boldsymbol{x} = [x_1, \ldots, x_n]^T$ is a real-valued column vector. The function $G(\boldsymbol{x}, \mathbf{C})$ represents the joint probability density function for $n$ zero-mean Gaussian random variables $X_1, \ldots, X_n$, with covariance matrix $\mathbf{C}$, evaluated at point $\boldsymbol{x}$. The covariance matrix elements are $\mathbf{C}_{ij} = E_{\boldsymbol{x}}\{X_i X_j\}$, where $E_{\boldsymbol{x}}\{\cdot\}$ denotes the statistical averaging over $X_1, \ldots, X_n$. With this new notation, the integral in (B.1) can be written as follows

$$F_{j,\mathrm{d}} = \frac{16\sqrt{\det \mathbf{K}}}{\eta_1 \eta_2 P_j} E_{\boldsymbol{\zeta}} \left\{1 - |\zeta_{pj}|^2 - \left|d_L^* \zeta_a^L + d_R^* \zeta_a^R\right|^2 + |\zeta_{pj}|^2 \left|d_L^* \zeta_a^L + d_R^* \zeta_a^R\right|^2\right\}, \tag{B.5}$$

where the factor $\eta_1\eta_2$ is due to the change of variables from $\{\zeta_{p1}, \zeta_{p2}\}$ to $\{\zeta_p^+, \zeta_p^-\}$ using (4.10). The above moments can be written in terms of the elements of the covariance matrix $\mathbf{K}$. The latter can be found by inverting $\mathbf{K}^{-1}$, which can be easily obtained from (4.11). The resulting symmetric matrix has been summarized in Table B.1. It can be shown that $\sqrt{\det \mathbf{K}} = \eta_1\eta_2/(4\alpha_L\alpha_R)$. Now, we can simplify (B.5), by noting that

$$\begin{aligned} E_{\boldsymbol{\zeta}}\left\{|\zeta_{pj}|^2\right\} &= \frac{E_{\boldsymbol{\zeta}}\left\{|\zeta_p^+|^2 + |\zeta_p^-|^2 + 2(-1)^j \Re\{\zeta_p^+ {\zeta_p^-}^*\}\right\}}{2\eta_j} \\ &= \frac{[\mathbf{K}_{55} + \mathbf{K}_{66} + \mathbf{K}_{33} + \mathbf{K}_{44} + 2(-1)^j(\mathbf{K}_{35} + \mathbf{K}_{46})]}{2\eta_j} \\ &= 1. \end{aligned} \tag{B.6}$$

Also, by using the moment-factoring theorem for Gaussian variables, we obtain

$$\begin{aligned} E_{\boldsymbol{\zeta}}\left\{|\zeta_{pj}|^2 \left|d_L^* \zeta_a^L + d_R^* \zeta_a^R\right|^2\right\} &= \left|E_{\boldsymbol{\zeta}}\left\{\zeta_{pj}(d_L^* \zeta_a^L + d_R^* \zeta_a^R)\right\}\right|^2 \\ &\quad + \left|E_{\boldsymbol{\zeta}}\left\{\zeta_{pj}^*(d_L^* \zeta_a^L + d_R^* \zeta_a^R)\right\}\right|^2 \\ &\quad + E_{\boldsymbol{\zeta}}\left\{|\zeta_{pj}|^2\right\} E_{\boldsymbol{\zeta}}\left\{\left|d_L^* \zeta_a^L + d_R^* \zeta_a^R\right|^2\right\}, \end{aligned} \tag{B.7}$$

in which

$$E_{\boldsymbol{\zeta}}\left\{\zeta_{pj}(d_L^* \zeta_a^L + d_R^* \zeta_a^R)\right\} = \sqrt{\frac{\eta_j}{2}} \left((-1)^{j-1} \sqrt{\eta_L p_{c_L}} d_L^* e^{i\theta_L} - \sqrt{\eta_R p_{c_R}} d_R^* e^{i\theta_R}\right) \tag{B.8}$$

and

$$E_{\boldsymbol{\zeta}}\left\{\zeta_{pj}^*(d_L^* \zeta_a^L + d_R^* \zeta_a^R)\right\} = 0. \tag{B.9}$$

Plugging (B.6)–(B.9) into (B.5), we finally obtain

Table B.1: The elements of the covariance matrix **K**.

$$\mathbf{K}_{11} = \mathbf{K}_{22} = (1 - p_{c_L})/2 + \eta_L p_{c_L}(\eta_1 + \eta_2)/4$$
$$\mathbf{K}_{24} = \mathbf{K}_{42} = -\mathbf{K}_{13} = -\mathbf{K}_{31} = (\eta_1 + \eta_2)\sqrt{\eta_L p_{c_L}} \cos\theta_L/4$$
$$\mathbf{K}_{14} = \mathbf{K}_{23} = \mathbf{K}_{32} = \mathbf{K}_{41} = -(\eta_1 + \eta_2)\sqrt{\eta_L p_{c_L}} \sin\theta_L/4$$
$$\mathbf{K}_{15} = \mathbf{K}_{51} = -\mathbf{K}_{26} = -\mathbf{K}_{62} = (\eta_1 - \eta_2)\sqrt{\eta_L p_{c_L}} \cos\theta_L/4$$
$$\mathbf{K}_{16} = \mathbf{K}_{25} = \mathbf{K}_{52} = \mathbf{K}_{61} = (\eta_1 - \eta_2)\sqrt{\eta_L p_{c_L}} \sin\theta_L/4$$
$$\mathbf{K}_{17} = \mathbf{K}_{28} = \mathbf{K}_{71} = \mathbf{K}_{82} = (\eta_2 - \eta_1)\sqrt{\eta_L p_{c_L} \eta_R p_{c_R}} \cos(\theta_L - \theta_R)/4$$
$$\mathbf{K}_{18} = \mathbf{K}_{81} = -\mathbf{K}_{27} = -\mathbf{K}_{72} = (\eta_2 - \eta_1)\sqrt{\eta_L p_{c_L} \eta_R p_{c_R}} \sin(\theta_R - \theta_L)/4$$
$$\mathbf{K}_{33} = \mathbf{K}_{44} = \mathbf{K}_{55} = \mathbf{K}_{66} = (\eta_2 + \eta_1)/4$$
$$\mathbf{K}_{35} = \mathbf{K}_{53} = \mathbf{K}_{46} = \mathbf{K}_{64} = (\eta_2 - \eta_1)/4$$
$$\mathbf{K}_{37} = \mathbf{K}_{73} = -\mathbf{K}_{48} = -\mathbf{K}_{84} = (\eta_1 - \eta_2)\sqrt{\eta_R p_{c_R}} \cos\theta_R/4$$
$$\mathbf{K}_{38} = \mathbf{K}_{47} = \mathbf{K}_{74} = \mathbf{K}_{83} = (\eta_1 - \eta_2)\sqrt{\eta_R p_{c_R}} \sin\theta_R/4$$
$$\mathbf{K}_{68} = \mathbf{K}_{86} = -\mathbf{K}_{57} = -\mathbf{K}_{75} = (\eta_1 + \eta_2)\sqrt{\eta_R p_{c_R}} \cos\theta_R/4$$
$$\mathbf{K}_{58} = \mathbf{K}_{67} = \mathbf{K}_{76} = \mathbf{K}_{85} = -(\eta_1 + \eta_2)\sqrt{\eta_R p_{c_R}} \sin\theta_R/4$$
$$\mathbf{K}_{77} = \mathbf{K}_{88} = (1 - p_{c_R})/2 + \eta_R p_{c_R}(\eta_1 + \eta_2)/4$$
$$\mathbf{K}_{12} = \mathbf{K}_{21} = \mathbf{K}_{34} = \mathbf{K}_{43} = \mathbf{K}_{36} = \mathbf{K}_{63} = \mathbf{K}_{45} = \mathbf{K}_{54} = \mathbf{K}_{56} = \mathbf{K}_{65} = \mathbf{K}_{78} = \mathbf{K}_{87} = 0$$

$$F_{j,\mathrm{d}} = \frac{\eta_j(1 - p_{c_L})(1 - p_{c_R})}{2P_j} \left| \sqrt{\eta_L p_{c_L}} d_L^* e^{i\theta_L} + (-1)^j \sqrt{\eta_R p_{c_R}} d_R^* e^{i\theta_R} \right|^2, \qquad j = 1, 2. \tag{B.10}$$

From (B.10), it can be easily seen that the maximum fidelity is achieved by the state given by (4.34). Also, by assuming $d_L = \pm d_R = 1/\sqrt{2}$, we find the fidelities of entanglement for the singlet and triplet states as given by (4.31). Although we only derived (B.10) for PNRD systems, one can verify that it also holds for NRPD systems.

The heralding probabilities in (4.22) can be derived from (4.21) by noting that

$$\chi_A^{\hat{\rho}_{\mathrm{out}}}(0, 0, \zeta_{p1}, \zeta_{p2}) = (2\pi)^2 \sqrt{\det \mathbf{K}'}\, G(\boldsymbol{\zeta}', \mathbf{K}'), \tag{B.11}$$

where $\boldsymbol{\zeta}' = [\zeta_{pr}^-, \zeta_{pi}^-, \zeta_{pr}^+, \zeta_{pi}^+]^T$, and

$$\mathbf{K}' = \frac{1}{\beta_L \beta_R - \delta^2} \begin{bmatrix} \beta_R & 0 & -\delta & 0 \\ 0 & \beta_R & 0 & -\delta \\ -\delta & 0 & \beta_L & 0 \\ 0 & -\delta & 0 & \beta_L \end{bmatrix} \tag{B.12}$$

with $\sqrt{\det \mathbf{K}'} = 1/(\beta_L \beta_R - \delta^2)$. The rest of derivation is straightforward; it parallels what we have done for the fidelities and will be omitted.

# Bibliography

[1] Y. I. Manin. Computable and uncomputable (in Russian). *Sovetskoye Radio*, 1980.

[2] R. P. Feynman. Simulating physics with computers. *Int. J. Theor. Phys.*, 21:467, 1982.

[3] D. Deutsch. Quantum theory, the Church-Turing principle and the universal quantum computer. *Proc. R. Soc. Lond. A*, 400:97, 1985.

[4] P. W. Shor. Algorithms for quantum computation: discrete logarithm and factoring. Proc. 35th Symp. Foundations of Computer Science, IEEE Press, Los Alamitos, CA, 1994.

[5] L. Grover. *Proc. 28th Annual ACM Symp. Theory of Computer Science*, page 212, 1996.

[6] N. Gisin, G. Ribordy, W. Tittel, and H. Zbinden. Quantum cryptography. *Rev. Mod. Phys.*, 74:145, 2002.

[7] G. Amaslennikov, A. A. Zhukov, M. V. Chekhova, and S. P. Kulik. Practical realization of a quantum cryptography protocol exploiting polarization encoding in qutrits. *J. Opt. B.: Quantum Semiclass. Opt.*, 5:S530, 2003.

[8] M. Riebe, H. Haffner, C. F. Roos, W. Hansel, J. Benhelm, G. P. T. Lancaster, T. W. Korber, C. Becher, F. Schmidt-Kaler, D. F. V. James, and R. Blatt. Deterministic quantum teleportation with atoms. *Nature*, 429:734, 2004.

[9] M. D. Barrett, J. Chiaverini, T. Schaetz, J. Britton, W. M. Itano, J. D. Jost, E. Knill, C. Langer, D. Leibfried, R. Ozeri, and D. J. Wineland. Deterministic quantum teleportation of atomic qubits. *Nature*, 429:737, 2004.

[10] M. A. Nielsen and I. L. Chuang. *Quantum Computation and Quantum Information.* Cambridge University Press, 2000.

[11] D. Dieks. Communication by EPR devices. *Phys. Rev. Lett.*, 92:271, 1982.

[12] W. K. Wootters and W. H. Zurek. A single quantum cannot be cloned. *Nature*, 299:802, 1982.

[13] H. Barnum, C. M. Caves, C. A. Fuchs, R. Jozsa, and B. Schumacher. Noncommuting mixed states cannot be broadcast. *Phys. Rev. Lett.*, 76:2818, 1996.

[14] C. H. Bennett, G. Brassard, C. Crépeau, R. Jozsa, A. Peres, and W. K. Wootters. Teleporting an unknown quantum state via dual classical and Einstein-Podolsky-Rosen channels. *Phys. Rev. Lett.*, 70:1895, 1993.

[15] D. Gottesman and I. L. Chuang. Demonstrating the viablity of universal quantum computation using teleportation and single-qubit operations. *Nature*, 402:390, 1999.

[16] K.-Y. Chen, T. Hogg, and R. Beausoleil. A quantum treatment of public goods economics. *Quantum Inf. Process.*, 1:449, 2002.

[17] P. G. Kwiat, Klaus Mattle, H. Weinfurter, Anton Zeilinger, A. V. Sergienko, and Y. Shih. New high-intensity source of polarization-entangled photon pairs. *Phys. Rev. Lett.*, 75:4337, 1995.

[18] P. G. Kwiat, E. Waks, A. G. White, I. Appelbaum, and P. H. Eberhard. Ultrabright source of polarization-entangled photons. *Phys. Rev. A*, 60:R773, 1999.

[19] F. König, E. J. Mason, F. N. C. Wong, and M. A. Albota. Efficient and spectrally bright source of polarization-entangled photons. *Phys. Rev. A*, 71:033805, 2005.

[20] M. Fiorentino, C. Kuklewicz, and F. N. C. Wong. Source of polarization entanglement in a single periodically poled KTiOPO4 crystal with overlapping emission cones. *Opt. Express*, 13:127, 2005.

[21] N. Lütkenhaus, J. Calsamiglia, and K.-A. Suominen. Bell measurements for teleportation. *Phys. Rev. A*, 59:3295, 1999.

[22] P. G. Kwiat and H. Weinfurter. Embeded Bell-state analysis. *Phys. Rev. A*, 58:R2623, 1998.

[23] C. Schuck, G. Huber, C. Kurtsiefer, and H. Weinfurter. Complete deterministic linear optics Bell state analysis. *Phys. Rev. Lett.*, 96:190501, 2006.

[24] M. O. Scully and M. S. Zubairy. *Quantum Optics.* Cambridge University Press, New York, 1997.

[25] J. J. Sakurai. *Modern Quantum Mechanics.* Addison Wesley Pub. Co., 1994.

[26] J. I. Cirac, P. Zoller, H. J. Kimble, and H. Mabuchi. Quantum state transfer and entanglement distribution among distant nodes in a quantum network. *Phys. Rev. Lett.*, 78:3221, 1997.

[27] S. J. van Enk, J. I. Cirac, and P. Zoller. Ideal quantum communication over noisy channels: a quantum optical implementation. *Phys. Rev. Lett.*, 78:4293, 1997.

[28] M. Fleischhauer, S. F. Yelin, and M. D. Lukin. How to trap photons? Storing single-photon quantum states in collective atomic ensembles. *Opt. Commun.*, 179:395, 2000.

[29] L. M. Duan, M. D. Lukin, J. I. Cirac, and P. Zoller. Long-distance quantum communication with atomic ensembles and linear optics. *Nature*, 414:413, 2001.

[30] J. H. Shapiro. Architectures for long-distance quantum teleportation. *New J. Phys.*, 4:art. 47, 2002.

[31] S. Bose, V. Vedral, and P. L. Knight. Multiparticle generalization of entanglement swapping. *Phys. Rev. A*, 57:822, 1998.

[32] D. N. Matsukevich, T. Chanelière, S. D. Jenkins, S.-Y. Lan, T. A. B. Kennedy, and A. Kuzmich. Entanglement of remote atomic qubits. *Phys. Rev. Lett.*, 96:030405, 2006.

[33] W. J. Munro, K. Nemoto, and T. P. Spiller. Weak nonlinearities: a new route to optical quantum information. *New J. Phys.*, 7:art. 137, 2005.

[34] T. P. Spiller, K. Nemoto, S. L. Braunstein, W. J. Munro, P. van Loock, and G. L. Milburn. Quantum computation by communication. *New J. Phys.*, 8:art. 30, 2006.

[35] J. H. Shapiro. Single-photon Kerr nonlinearities do not help quantum computation. *Phys. Rev. A*, 73:062305, 2006.

[36] A. S. Parkins, P. Marte, P. Zoller, O. Carnal, and H. J. Kimble. Quantum-state mapping between multilevel atoms and cavity light fields. *Phys. Rev. A*, 51:1578, 1995.

[37] C. W. Gardiner and M. J. Collett. Input and output in damped quantum systems: Quantum stochastic differential equations and the master equation. *Phys. Rev. A*, 31:3761, 1985.

[38] K. J. Blow, R. Loudon, and S. J. D. Phoenix. Continuum fields in quantum optics. *Phys. Rev. A*, 42:4102, 1990.

[39] S. M. Dutra. *Cavity quantum electrodynamics: the strange theory of light in a box.* John Wiley, New York, 2005.

[40] C. W. Gardiner and P. Zoller. *Quantum noise: a handbook of Markovian and non-Markovian quantum stochastic methods with applications to quantum optics.* Springer, New York, 3rd edition, 2004.

[41] J. H. Shapiro and N. C. Wong. An ultrabright narrowband source of polarization-entangled photon pairs. *J. Opt. B: Quantum. and Semiclass. Opt.*, 2:L1, 2000.

[42] J. R. Kulklinski, U. Gaubatz, F. T. Hioe, and K. Bergmann. Adiabatic population transfer in a three-level system driven by delayed laser pulses. *Phys. Rev. A*, 40:6741, 1989.

[43] S. Lloyd, J. H. Shapiro, F. N. C. Wong, P. Kumar, S. M. Shahriar, and H. P. Yuen. Infrastructure for the quantum internet. *Computer Commun. Rev.*, 34:9, 2004.

[44] B. J. Yen and J. H. Shapiro. Error models for long-distance qubit teleportation. *IEEE J. Sel. Topics Quantum Electron.*, 9:1483, 2003.

[45] S. Lloyd, M. S. Shahriar, J. H. Shapiro, and P. R. Hemmer. Long distance, unconditional teleportation of atomic states via complete Bell state measurements. *Phys. Rev. Lett.*, 87:167903, 2001.

[46] V. Giovannetti, L. Maccone, J. H. Shapiro, and F. C. Wong. Generating entangled two-photon state with coincident frequencies. *Phys. Rev. Lett.*, 88:183602, 2002.

[47] C. E. Kuklewicz, F. N. C. Wong, and J. H. Shapiro. Time-bin modulated polarization-entangled biphotons from cavity-enhanced down-conversion. quant-ph:0605093, 2006.

[48] L. M. Duan, J. I. Cirac, and P. Zoller. Three-dimensional theory for interaction between atomic ensembles and free-space light. *Phys. Rev. A*, 66:023818, 2002.

[49] J. Mostowski and B. Sobolewska. Transverse effects in stimulated Raman scattering. *Phys. Rev. A*, 30:610, 1984.

[50] D. Felinto, C. W. Chou, H. de Riedmatten, S. V. Polyakov, and H. J. Kimble. Control of decoherence in the generation of photon pairs from atomic ensembles. *Phys. Rev. A*, 72:053809, 2005.

[51] T. Chanelière, D. N. Matsukevich, S. D. Jenkins, S.-Y. Lan, T. A. B. Kennedy, and A. Kuzmich. Storage and retrieval of single photons transmitted between remote quantum memories. *Nature*, 438:833, 2005.

[52] H. P. Yuen and J. H. Shapiro. Optical communication with two-photon coherent states—part iii: quantum measurements realizable with photoemissive detectors. *IEEE Trans. Inform. Theory*, 26:78, 1980.

[53] R. A. Campos, B. E. A. Saleh, and M. C. Teich. Quantum-mechanical lossless beam splitter: SU(2) symmetry and photon statistics. *Phys. Rev. A*, 40:1371, 1989.

[54] C. K. Hong, Z. Y. Ou, and L. Mandel. Measurement of subpicosecond time intervals between two photons by interference. *Phys. Rev. Lett.*, 59:2044, 1987.

[55] E. Knill, R. Laflamme, and G. J. Milburn. A scheme for efficient quantum computation with linear optics. *Nature*, 409:46, 2001.

[56] T. B. Pittman, M. J. Fitch, B. C Jacobs, and J. D. Franson. Experimental controlled-NOT logic gate for single photons in the coincidence basis. *Phys. Rev. A*, 68:032316, 2003.

[57] M. Fiorentino and F. N. C. Wong. Deterministic controlled-NOT gate for single-photon two-qubit quantum logic. *Phys. Rev. Lett.*, 93:070502, 2004.

[58] I. L. Chuang and Y. Yamamoto. Simple quantum computer. *Phys. Rev. A*, 52:3489, 1995.

[59] Q. A. Turchette, C. J. Hood, W. Lange, H. Mabuchi, and H. J. Kimble. Measurement of conditional phase shifts for quantum logic. *Phys. Rev. Lett.*, 75:4710, 1995.

[60] M. F. Yanik, S. Fan, M. Soljacic, and J. D. Joannopoulos. All-optical transistor action with bistable switching in a photonic crystal cross-waveguide geometry. *Opt. Lett.*, 28:2506, 2003.

[61] K. Kuriki, O. Shapira, S. D. Hart, B. Benoit, Y. Kuriki, J. F. Viens, M. Bayindir, J. D. Joannopoulos, and Y. Fink. Hollow multilayer photonic bandgap fibers for NIR applications. *Opt. Express*, 12:1510, 2004.

[62] L. Boivin, F. X. Kärtner, and H. A. Haus. Analytical solution to the quantum field theory of self-phase modulation with a finite response time. *Phys. Rev. Lett.*, 73:240, 1994.

[63] W. H. Louisell. *Radiation and Noise in Quantum Electronics.* McGraw-Hill Company, New York, 1964.

[64] S. E. Harris. Electromagnetically induced transparency. *Phys. Today*, 50:36, 1997.

[65] R. G. Beausoleil, W. J. Munro, D. A. Rudrigues, and T. P. Spiller. Applications of electromagnetically induced transparency to quantum information processing. *J. Modern Opt.*, 10:2441, 2004.

[66] C. Ottaviani, S. Rebić, D. Vitali, and P. Tombesi. Quantum phase-gate operation based on nonlinear optics: Full quantum analysis. *Phys. Rev. A*, 73:010301, 2006.

[67] M. Razavi, V. Giovannetti, L. Maccone, and J. H. Shapiro. Hot-cavity loading: A Heisenberg-Langevin analysis. *in Quantum Electronics and Laser Science Conference*, Technical Digest:QFA7, Long Beach, CA, 2006.

[68] M. Razavi and J. H. Shapiro. Long-distance quantum communication with neutral atom. *in Fluctuation and Noise, SPIE Proc.*, 5842:132, Austin, TX, 2005.

[69] M. Razavi and J. H. Shapiro. Long-distance quantum communication with neutral atom. *Phys. Rev. A*, 73:042303, 2006.

[70] J. H. Shapiro and M. Razavi. Continuous-time cross-phase modulation and quantum computation. *in Proc. Quantum Communication, Measurement, and Computing*, Japan, 2006.

[71] J. P. Reithmaier, G. Sęk, A. Löffler, C. Hofmann, S. Kuhn, S. Reitzenstein, L. V. Keldysh, V. D. Kulakovskii, T. L. Reinecke, and A. Forchel. Strong coupling in a single quantum dot-semiconductor microcavity system. *Nature*, 432:197, 2004.

[72] T. Yoshie, A. Scherer, J. Hendrickson, G. Khitrova, H. M. Gibbs, G. Rupper, C. Ell, O. B. Shchekin, and D. G. Deppe. Vacuum Rabi splitting with a single quantum dot in a photonic crystal nanocavity. *Nature*, 432:200, 2004.

[73] A. Imamoḡlu, D. D. Awschalom, G. Burkard, D. P. DiVincenzo, D. Loss, M. Sherwin, and A. Small. Quantum information processing using quantum dot spins and cavity QED. *Phys. Rev. Lett.*, 83:4204, 1999.

[74] A. Blais, R. Huang, A. Wallraff, S. M. Girvin, and R. J. Schoelkopf. Cavity quantum electrodynamics for superconducting electrical circuits: An architecture for quantum computation. *Phys. Rev. A*, 69:062320, 2004.

[75] B. Darquié, M. P. A. Jones, J. Dingjan, J. Beugnon, S. Bergamini, Y. Sortais, G. Messin, A. Browaeys, and P. Grangier. Controlled single-photon emission from a single trapped two-level atom. *Science*, 309:454, 2005.

[76] L. M. Duan and H. J. Kimble. Efficient engineering of multiatom entanglement through single-photon detections. *Phys. Rev. Lett.*, 90:253601, 2003.

[77] T. Chanelière, D. N. Matsukevich, S. D. Jenkins, T. A. B. Kennedy, M. S. Chapman, and A. Kuzmich. Quantum telecommunication based on atomic cascade transitions. *Phys. Rev. Lett.*, 96:093604, 2006.

[78] M. S. Shahriar, P. Pradhan, G. S. Pati, V. Gopal, and K. Salit. Light-shift imbalance induced blockade of collective excitations beyond the lowest order. quant-ph:0604120, 2006.

[79] M. S. Shahriar, G. S. Pati, and K. Salit. Quantum communication and computing with atomic ensembles using light-shift imbalance induced blockade. quant-ph:0604121, 2006.

[80] V. Giovannetti and L. Maccone. Quantum internet: cavity loading study. *Internal Report, RLE, MIT*, 2004.